Fakultät für Physik und Astronomie
Ruprecht–Karls–Universität Heidelberg

Master's thesis in Physics
submitted by

Svenja Lohmann

born in Würzburg

December 17, 2015

Beam diagnostics and collector for the electron cooler of the cryogenic storage ring CSR

This Master's thesis has been carried out by Svenja Lohmann
at the Max-Planck-Institut für Kernphysik
under the supervision of

Prof. Dr. Andreas Wolf

Abstract

Beam diagnostics and collector for the electron cooler of the cryogenic storage ring CSR – The CSR electron cooler will be employed both for phase space cooling and as a target for electron-ion collision experiments. Aligning the beams is essential for both applications and, therefore, the cooler features two rotating wire scanners for beam position determination. In the course of this work their design has been finalised. A scheme has been developed to calculate the transverse beam location from two measured rotation angles. This can be utilised to determine the centres of the electron and ion beams. While in the former case a signal is directly induced at the wires, identification of the latter depends on an increasing restriction of phase space with advancing rotation. A procedure is proposed to detect the decline in ion intensity with the CSR's current pick-up.
Furthermore, the electron collector of the cooler has been designed and assembled. A Wien filter is included to minimise backstreaming of secondary electrons, which will prolong the lifetime of the GaAs photocathode. Calculations and a simulation were conducted to optimise its design. Additionally, an analyser cup allows for beam profile and energy distribution measurements. From this, among others, the electron density can be computed, which is necessary for rate coefficient calculations.

Zusammenfassung

Strahldiagnose und Kollektor für den Elektronenkühler des kryogenen Speicherring CSR – Der CSR Elektronenkühler wird sowohl für Phasenraumkühlung als auch als Target für Kollisionsexperimente zwischen Elektronen und Ionen verwendet werden. Für beide Anwendungen ist es essentiell, dass die Strahlen übereinander liegen. Der Kühler ist daher mit zwei rotierenden Drahtdetektoren (Wire Scanner) für die Bestimmung der Strahlposition ausgestattet. Im Verlauf dieser Arbeit wurde deren Design fertiggestellt. Ein Schema für die Berechnung der transversalen Strahlposition aus den zwei gemessenen Drehwinkeln wurde entwickelt. Dieses kann dafür genutzt werden, den Mittelpunkt des Elektronen- bzw. Ionenstrahls zu bestimmen. Während im ersten Fall das Signal direkt im Draht induziert wird, hängt die Identifizierung von letzterem von der zunehmenden Begrenzung des Phasenraumes während der Rotation ab. Es wurde ein Verfahren zur Messung der abnehmenden Ionenintensität mit dem Strommonitor des CSR vorgeschlagen.
Des Weiteren wurde der Elektronenkollektor für den Kühler entworfen und aufgebaut. Er enthält einen Wienfilter, welcher Sekundärelektronen daran hindert, zur GaAs Photokathode zurückzufließen, wodurch deren Lebensdauer verlängert wird. Mithilfe von Berechnungen und einer Simulation wurde dessen Design optimiert. Durch den Einbau eines Analysators können Strahlprofile und Energieverteilungen gemessen werden. Hieraus kann die Elektronendichte abgeleitet werden, welche notwendig für die Berechnung von Ratenkoeffizienten ist.

Einführung für Nicht-Physiker

Die häufig gestellte Frage: “Und was machst du so in deiner Masterarbeit?”, erweist sich als schwierig zu beantworten, wenn sie von Nicht-Physikern gestellt wird. Mir ist es immer ein Anliegen gewesen, sie trotzdem zu beantworten. Daher jetzt diese Einführung:

Das übergeordnete Experiment, an dem die beiden Projekte meiner Arbeit angesiedelt sind, ist der CSR am Max-Planck-Institut für Kernphysik. CSR steht für cryogenic storage ring – kryogener Speicherring. Kryogen bedeutet kalt, sehr kalt – in diesem Fall ungefähr $-263\,^{\circ}\mathrm{C}$. Ein Speicherring besteht im Wesentlichen aus einem ringförmig (bzw. in unserem Fall eher quadratisch) angeordneten Vakuumrohr, das heißt aus einer Umgebung, die nur noch sehr wenig Luft enthält. Diese Bedingungen – extreme Kälte, hohes Vakuum – sind die gleichen wie im Weltraum. Nun ist auch das All nicht komplett leer; es gibt Sterne, Planeten, Kometen, Staub... . Wie die Erde auch bestehen diese Objekte aus Atomen und Molekülen. Diese liegen allerdings meistens – und das ist ein Unterschied zur Erde – in einem elektrisch geladenen Zustand vor. Man bezeichnet sie dann als Ionen. Hier kommt jetzt wieder der Speicherring ins Spiel. In einem solchen können elektrisch geladene Teilchen gespeichert werden. Das bedeutet, dass sie fortlaufend auf der durch das Rohr definierten Bahn zirkulieren.

Mit diesen gespeicherten Ionen kann man dann Experimente machen, indem man zum Beispiel andere Teilchen oder Laserlicht in den Ring einschießt und die dann auftretenden Reaktionen untersucht. Für die Durchführung und Auswertung solcher Experimente ist es nützlich, wenn alle Teilchen einen klar definierten Strahl formen. Das heißt man möchte, dass die Ionen möglichst parallel, in einem möglichst dünnen Strahl und möglichst alle mit derselben Geschwindigkeit durch den Ring fliegen. Die Geschwindigkeitsunterschiede zwischen den Teilchen bezeichnet der Physiker als Strahltemperatur. Analog dazu wird die Methode, die genutzt wird, um solch einen Strahl zu erhalten, als Strahlkühlung bezeichnet. In unserem Fall verwenden wir dazu einen zweiten, kälteren Teilchenstrahl, diesmal bestehend aus Elektronen.

Man kann diesen Vorgang analog dazu betrachten, einen heißen Gegenstand mit kaltem Wasser zu kühlen. Es ist leicht einzusehen, dass die Kühlung am effektivsten ist, wenn man den Gegenstand direkt unter einen kalten Wasserstrahl hält. In diesem Fall fließt immer neues, kaltes Wasser nach, so dass der Gegenstand bis auf die Wassertemperatur abgekühlt werden kann. Die Elektronenstrahlkühlung funktioniert im Prinzip genauso. Kalte Elektronen werden kontinuierlich an einer Stelle in den CSR eingeschossen und dem gespeicherten Strahl überlagert. Nach ungefähr einem Meter verlassen sie den Ring wieder. Die Temperatur des Ionenstrahls kann dadurch theoretisch auf die Elektronentemperatur abgesenkt werden.

Genau wie man das verbrauchte Kühlwasser auffangen muss, um nicht seine Wohnung zu fluten, muss man auch die Elektronen stoppen. Das Instrument, welches dafür verwendet wird, heißt Kollektor. Im einfachsten Fall besteht dieser nur aus einem Metallbecher, mit dem die Elektronen eingefangen werden. Mit unserem Kollektor kann man jedoch zusätzlich einige Eigenschaften des Elektronenstrahls messen: zum Beispiel die Strahlgröße und -temperatur und wie viele Elektronen pro Sekunde von dem Becher aufgefangen werden. Eines der Projekte meiner Masterarbeit bestand aus der Entwicklung dieses Kollektors.

Um noch einmal auf das Bild der Wasserkühlung zurückzukommen: Man kann sich leicht vorstellen, dass diese Kühlung viel effizienter ist, wenn der Wasserstrahl den heißen Gegenstand vollständig umschließt. Das gleiche gilt auch für das Kühlen des gespeicherten Ionenstrahls. Um dies zu ermöglichen, muss man Informationen darüber haben, wo im Vakuumrohr die beiden Strahlen liegen. Mein zweites Projekt geht dieser Frage nach. Dazu fährt man zwei auf spezielle Art gebogene Drähte über den Querschnitt des Rohres. Wenn einer der Drähte den Strahl schneidet, kann man ein Signal an dieser Drahtposition messen. Aus den Signalpositionen beider Drähte kann man dann die Lage des Strahls innerhalb des Rohrprofils berechnen.

Elektronen sind negativ geladen. Wenn man nun positiv geladene Ionen im Ring speichert, kann es durch die elektrische Anziehung zu einer Verbindung beider Teilchensorten kommen. Solche Reaktionen, die auch in der Natur auftreten, wollen wir mithilfe des CSR untersuchen. Um die experimentellen Ergebnisse richtig beurteilen zu können, ist es von großer Bedeutung, die Voraussetzungen des Versuchs genau zu kennen. Dies ist ein weiterer Grund, warum es wichtig ist, die Eigenschaften des Elektronenstrahls vermessen zu können, wie es durch den Kollektor ermöglicht wird.

Contents

List of Figures xi

1 Introduction 1

2 CSR and its use in electron collision experiments 5

2.1 Electrostatic versus magnetic storage rings . . . 6

2.2 The cryogenic environment . . . 7

2.3 Design . . . 8

2.3.1 Overview . . . 8

2.3.2 Cryogenic and vacuum technology . . . 10

2.4 Electron-ion collision experiments . . . 10

3 The CSR electron cooler 13

3.1 How to describe stored particle beams . . . 13

3.1.1 Coordinate systems . . . 13

3.1.2 Phase space ellipses and Liouville's theorem . . . 14

3.1.3 The betatron function and the machine ellipse . . . 15

3.2 Phase space cooling . . . 17

3.3 Cold electron production . . . 19

3.3.1 The GaAs photocathode . . . 20

3.3.2 Adiabatic magnetic transverse expansion . . . 21

3.3.3 Lifetime limiting effect of secondary electrons on the photocathode . . . 23

3.4 Design . . . 23
3.5 The electron cooler as target . . . 25

4 Beam positioning with rotating wire scanners 27
4.1 Mechanical design . . . 28
4.2 Mathematical model for beam position determination . . . 32
4.3 Simulation of the scanners with an extended beam . . . 34
4.3.1 The electron beam . . . 35
4.3.2 The ion beam . . . 37
4.4 Discussion . . . 42

5 Development of an electron collector for the CSR electron cooler 47
5.1 Requirements on design . . . 48
5.1.1 Spatial constraints . . . 48
5.1.2 Operation in an UHV environment . . . 48
5.1.3 Minimisation of electron backstreaming . . . 52
5.2 Design . . . 55
5.2.1 Overview . . . 55
5.2.2 The Wien filter . . . 56
5.2.3 The analyser cup . . . 61
5.3 Present status . . . 64

6 Summary and outlook 65

A Mathematica script for beam position determination with scraper wires 67

Bibliography 71

List of Figures

2.1 Layout of the CSR 8

3.1 The horizontal and vertical betafunctions of the CSR 16

3.2 The horizontal and vertical optical functions $\alpha(s)$ of the CSR 17

3.3 Principle of electron cooling 18

3.4 Energy levels in a NEA GaAs photocathode 21

3.5 Layout of the CSR electron cooler 24

4.1 Position of the wire scanners in the interaction region 28

4.2 Model of one wire scanner 29

4.3 Side and front view of the wire scanner 30

4.4 Installation of one wire scanner at the end of the interaction region 31

4.5 Dependence of α_1 on x 34

4.6 Dependence of $\alpha_2 - \alpha_1$ on y 35

4.7 Linear fit for $\alpha_1(x)$ at $y = 0$ 36

4.8 Angle distribution for a centred electron beam with $R_e = 6.7\,\mathrm{mm}$ 37

4.9 Effects of a horizontally shifted beam on the modelled angular distribution 38

4.10 Effects of a vertically shifted beam on the modelled angular distribution 39

4.11 Principle of a scraper measurement 40

4.12 Modelled ion intensity as a function of the scraper rotation for a centred ion beam 42

4.13 Effect of a horizontally shifted beam on the modelled ion intensity 43

4.14 Modelled ion intensity of a beam with smaller initial cross section 44

4.15 Method to determine the ion beam location using four measurement steps 45

5.1 Layout of the collector section of the eCool 47

5.2 The longitudinal magnetic field B_0 in the collector section 49

5.3 Set-up for test of heat conductance 50

5.4 Temperatures at the test collector set-up as a function of applied power 51

5.5 Sketch of the potentials in the collector 53

5.6 Working principle of a Wien filter 53

5.7 Layout of the collector 55

5.8 Beam pipe with steerer rack in the collector region 57

5.9 Mounting rack for steerer and Wien filter coils 58

5.10 Location of the cuts for the display of equipotential line distributions 59

5.11 Equipotential line distribution inside the Wien filter: Version 1 59

5.12 Equipotential line distribution inside the Wien filter: Versions 2 and 3 60

5.13 Model of the analyser and main cup 61

5.14 Photograph of the main cup 62

5.15 Working principle of a retarding field analyser 63

5.16 Photograph of the collector 64

Chapter 1

Introduction

Natural science is commonly defined as the branch of science that aims to describe and understand the universe and the world around us based on empirical evidence. Thus, the very heart of all natural sciences are observations and experiments. Due to the high complexity of nature, scientists have always tried to isolate objects and phenomena, hence, being able to study the influence of single parameters. Any laboratory experiment is an example for such an isolation. By controlling the experimental conditions and varying the same, the response of the studied system can be analysed. Thereby, intrinsic properties, dependencies on external parameters and the interplay with the environment can be revealed. To which extent this is possible often depends on the technical feasibility. This is a self-energising process: greater knowledge about nature leads to technical progress, which again opens up new channels for research.

In physics the nature of the building blocks of matter has always provoked great interest. Several branches descend from this question, among them particle, nuclear, atomic and molecular physics. They have in common that they are concerned with microscopic objects that can only be studied with the help of technology. Many elementary particles and reactions can only be observed at higher energies. The advancing interest in these fields of physics, thus, triggered the development of particle accelerators. In 1932 Cockcroft and Walton succeeded to accelerate protons to an energy of $400\,\mathrm{keV}$ and to detect for the first time a nuclear reaction when shooting them on to a lithium target [10]. Since then both our understanding of matter and technological possibilities have grown. A big step was the proposal to accelerate and store particles on a circular orbit. Such storage rings [44] are synchrotron-like devices, which highly increase the time available for accumulating particles, manipulating the beam and of course experiments. The range of applications is accordingly versatile. While in the 1950s and 60s high energy synchrotrons centred the attention mainly to nuclear and elementary particle physics, later, storage rings operating at lower energies have been used to store atomic and molecular ions. Nowadays, all sorts of particles from leptons to biomolecules are stored in storage rings spanning an energy range from several keV up to $13\,\mathrm{TeV}$ at the Large Hadron Collider (LHC) at CERN [9].

Atoms and to an even greater extent molecules hold an inherent complexity already at thermal energies. Therefore, it is especially important to carefully select and control the circumstances of an experiment.

Storage rings provide a powerful tool for doing so. The respective atomic or molecular ion is produced in an ion source and typically accelerated to the desired energy before being injected into the storage ring. A magnet placed in front allows for the selection of a specific charge-to-mass ratio. Inside the ring the ions are bent and focussed by magnetic or electrostatic elements. Then, the particles circulate around a closed orbit, thus, passing every point in the ring many times. That way high luminosities[1] can be achieved. Given a sufficiently good vacuum, the beam life time (i.e. the time the beam remains in the ring) can be very long (seconds up to several hours, depending on the ion species and the individual storage ring [40]). The ultra-high vacuum (UHV) also minimises collisions with residual gas particles, which increases the signal-to-noise ratio of real events. In the case of ionic atoms and molecules a long storage time allows for the particle to relax into its rotational and vibrational ground state, hence, delivering very controlled conditions for experiments.

Another advantage is the possibility to manipulate the stored beam prior to experiments. A – for many reasons – frequently used form of manipulation is electron cooling. First proposed by Budker and Skrinskiĭ for the cooling of antiprotons [8], it later became a universal tool employed at atomic storage rings. The principle of this method is to transfer energy from the stored ions to much colder electrons via Coulomb interactions. The device which performs the task to produce electrons, merge them with the ion beam and after a certain length demerge and collect them is called electron cooler. Due to the recurrent passage of the ions through the cold electron stream, the ion beam temperature, that means the velocity spread, can be reduced. This has many benefits, among them an increased particle density, a lower divergence and the compensation of heating effects. Thereby, a high intensity and quality of the beam can be obtained and preserved during experimentation.

In atomic and molecular ion research an electron cooler can serve an additional purpose. By merging a beam of stored ions with the electrons, reactions as occurring in natural plasmas can be reproduced. Plasma is the fourth state of matter and appears in a wide variety of types. It actually is the most abundant form of matter in the observed universe. Plasmas can be found, at relatively low energies, in the interstellar medium and planetary atmospheres or at higher temperatures in the bodies and coronae of stars and in cometary comae [52]. Man-made plasmas are for example existent in combustion engines and tokamaks [67]. These environments exhibit a complexity too high to be understood by (remote) observation alone. Therefore, they constitute one case in which the replication of isolated processes by a laboratory experiment is needed. One important process in the evolution of a plasma is electron-ion recombination. By using a storage ring, cross sections of specific reactions can be measured. Each one of these isolated results contributes to the full picture of our growing understanding of such plasma environments.

The new **c**ryogenic **s**torage **r**ing (CSR), located at the Max-Planck-Institut für Kernphysik (MPIK, Max Planck Institute for Nuclear Physics), Heidelberg, Germany, is a fully electrostatic, cryogenic storage ring. It is a tool for the experimental study of dissociation and recombination processes of molecular ions. Therefore, it will be, among other things, equipped with a low-energy electron cooler. In order to be able to perform electron cooling and measure recombination cross sections, diagnostics of the electron beam is

[1] Luminosity is defined as target particles per unit area times beam particles per unit time. The product of the luminosity and the cross section of a reaction gives the event rate at a detector.

necessary. In the scope of this work means for beam position determination with the help of rotating wire scanners have been developed. Furthermore, an electron collector for the cooler has been designed.

The main body of this thesis is divided into four chapters. In the beginning, Chapter 2 gives an overview over the CSR and motivates the use of an electrostatic and cryogenic design. Chapter 3 focusses on electron cooling. Therein, the physical principle as well as the concrete set-up of the CSR electron cooler are explained. Special emphasis is placed on the functioning of the photocathode due to its impact on the design of the collector. In addition, the physics behind electron-ion recombination experiments is briefly described. Chapter 4 is dedicated to the development of the wire scanners. After depicting the mechanical structure, a scheme is developed which allows for the determination of the transverse beam position from signals measured using these scanners. In the following this is adopted to two different techniques for identifying the ion and electron beam location. Chapter 5 follows the proceedings in designing the electron collector. The collector is equipped with a Wien filter and an analyser circuit, which are characterised as well. A summary and an outlook conclude this work.

Chapter 2

CSR and its use in electron collision experiments

At first driven by the wish to study highly charged ions, from the 1980s on several atomic physics storage rings have been built and successfully operated. They are in alphabetical order the **A**arhus **st**orage **ri**ng **D**enmark (ASTRID) at the University of Aarhus, Denmark [37], the **cry**ogenic ion source **ring** (CRYRING) at the Manne Siegbahn Laboratory, Sweden [1], the **e**xperimental **s**torage **r**ing (ESR) at the Gesellschaft für Schwerionenforschung (GSI) in Darmstadt, Germany [18], the **t**est **a**ccumulation **r**ing for the **n**umatron accelerator facility (TARN II) at the Institute for Nuclear Study (INS) in Tokyo, Japan [29] and the **t**est **s**torage **r**ing (TSR) at the MPIK [24]. All of these rings have in common that they use magnets to bend and focus the stored beam. Although they have also made relevant contributions to molecular physics research, their magnetic design limits their applicability in this field. As will be shown below, storing molecular ions of higher masses soon becomes difficult with magnetic beam optics. With a shifting interest towards weakly charged heavy ions, a new generation of electrostatic storage rings has, thus, emerged. The first of such rings to be constructed was the **el**ectrostatic **i**on **s**torage ring **A**arhus (ELISA) at the University of Aarhus [38]. There is has been shown that it is indeed possible to store biomolecules [3] and heavy ions like C_{60}^- in such a device [2].

Another limitation of more conventional storage rings is given by their room temperature environment because the black body radiation excites rotational state transitions in molecules. The self-evident next step is, therefore, to operate a storage ring at cryogenic temperatures. This approach has been taken in the design of the **d**ouble **e**lectro**s**tatic **i**on-**r**ing **e**xp**e**riment (DESIREE) at Stockholm University [58]. It actually consists of two electrostatic storage rings sharing one straight section. This allows for the study of reactions between ions of opposite charge. Another cryogenic, electrostatic storage ring is presently commissioned at RIKEN in Japan. For the **Ri**ken **c**ryogenic **e**lectrostatic ring (RICE) atomic and molecular experiments with tunable lasers and neutral ion beams are planned [15, 41].

CSR falls into this family of storage rings. However, it is the only one of them that features an electron cooler and will, thus, study the dissociative recombination of molecular ions with electrons. This chapter

tries to further motivate the decisions for electrostatic beam optics (Sec. 2.1) and a cryogenic environment (Sec. 2.2) with respect to the planned experimental programme (Sec. 2.4). In addition, the design of the CSR is presented (Sec. 2.3).

2.1 Electrostatic versus magnetic storage rings

Every storage ring consists of a lattice of beam optics, i.e. focussing and bending elements, intercepted by drift regions. The latter are force-free and serve as experimental sections or leave room for beam diagnostics, bunching and/or accelerating devices. The ion optical elements manipulate the particle beam with help of the Lorentz force

$$\vec{F}_L = q \cdot (\vec{E} + \vec{v} \times \vec{B}), \tag{2.1}$$

where q and $\vec{v}$ are the charge and the velocity of the particle. $\vec{E}$ and $\vec{B}$ are the electric and magnetic field strength at the particles's position. The second part of Eq. 2.1 implies that magnetic forces can only change the direction but not the velocity of charged particles. Electric fields on the other hand can accelerate as well as deflect particles. Therefore, storage ring can either feature magnetic or electrostatic beam optics.

The component of the electric field perpendicular to $\vec{v}$, $\vec{E}_\perp$, forces a charged particle on a circular orbit with the radial acceleration $\mathrm{d}\vec{v}_\perp/\mathrm{d}t$,

$$q\vec{E}_\perp = \frac{\mathrm{d}\vec{p}_\perp}{\mathrm{d}t} = \gamma m \frac{\mathrm{d}\vec{v}_\perp}{\mathrm{d}t}. \tag{2.2}$$

m and $\vec{p}$ are the particle's mass and momentum and γ denotes the Lorentz factor. This force acts as a centripetal force and, thus,

$$\left|\frac{\mathrm{d}\vec{v}_\perp}{\mathrm{d}t}\right| = \frac{v^2}{\rho}, \tag{2.3}$$

where ρ is the current bending radius. Combining equations 2.2 and 2.3 gives the *electric rigidity*

$$E_\perp \rho = \frac{pv}{q} = \frac{\gamma m v^2}{q}. \tag{2.4}$$

For magnetic beam optics the same considerations hold. When $\vec{B}$ is always perpendicular to $\vec{v}$, the magnetic rigidity is given by

$$B\rho = \frac{p}{q} = \frac{\gamma m v}{q}. \tag{2.5}$$

The maximum rigidity (be it electric or magnetic) is a characteristic of the individual storage ring and gives the maximum velocity at which a particle of given mass-to-charge ratio can still be stored. Comparing equations 2.4 and 2.5 and setting $\gamma = 1$ shows that for an electrostatic storage ring the maximum velocity is inversely proportional to the square root of the particle's mass:

$$v_{max} \propto \frac{1}{\sqrt{m}}, \tag{2.6}$$

while for a magnetic storage ring its dependence on the mass is given by

$$v_{max} \propto \frac{1}{m}. \tag{2.7}$$

Since the cross section for residual gas induced ion loss rises with decreasing velocity [57], there is effectively an upper limit on the storable ion mass. This limit can be shifted towards higher masses in electrostatic storage rings because ions of the same mass can be stored at higher velocities compared to magnetic storage rings.

Considering only non-relativistic particles, Eq. 2.4 can be rewritten in terms of the particle's kinetic energy E_{kin}

$$E_{\perp}\rho = \frac{2E_{kin}}{q}. \tag{2.8}$$

For molecular ions q usually corresponds to one elementary charge because the production of higher charge states is not possible without breaking the chemical bonds. Therefore, the electric rigidity depends exclusively on the kinetic energy. In practice that means that different ion species, as long as they have the same kinetic energy, can be injected into the ring without changing any settings at the beam optical elements. Hence, an electrostatic storage ring yields a very flexible tool in heavy ion research.

2.2 The cryogenic environment

The CSR's experimental vacuum chamber can be cooled down to below $10\,\mathrm{K}$. This permits to overcome the following limitations of a room temperature environment. First, the achievable vacuum pressure is limited to some $10^{-11}\,\mathrm{mbar}$ due to degassing of mainly H_2 from the stainless steel vacuum chamber walls [31]. For the CSR a vacuum pressure better than $10^{-13}\,\mathrm{mbar}$ at room temperature is envisaged. Such low residual gas densities allow for longer storage times compared to an operation at $300\,\mathrm{K}$.

For the purpose of experiments with molecules, the cryogenic environment provides a second advantage, which is more fundamental from the physics point of view. It is a valid assumption that a molecule relaxes to its vibrational ground state within the storage time achievable even with storage rings operated at room temperature. Rotational state transitions, however, require energies low enough that they can be excited by

300 K black body radiation. A molecule stored in a non-cryogenic storage ring in general thermalises with this background and, hence, is existent in a mix of rotational states. The operation at below 10 K together with the long storage time enables the stored molecular ions to relax to their rotational ground state. This greatly improves the experimental precision since the initial configuration is well known.

Last but not least, the cryogenic UHV inside the CSR's experimental beamline provides a good model environment for the interstellar medium.

2.3 Design

2.3.1 Overview

Fig. 2.1 depicts the layout of the CSR. Shown is a model that already includes the electron cooler. All components are introduced below.

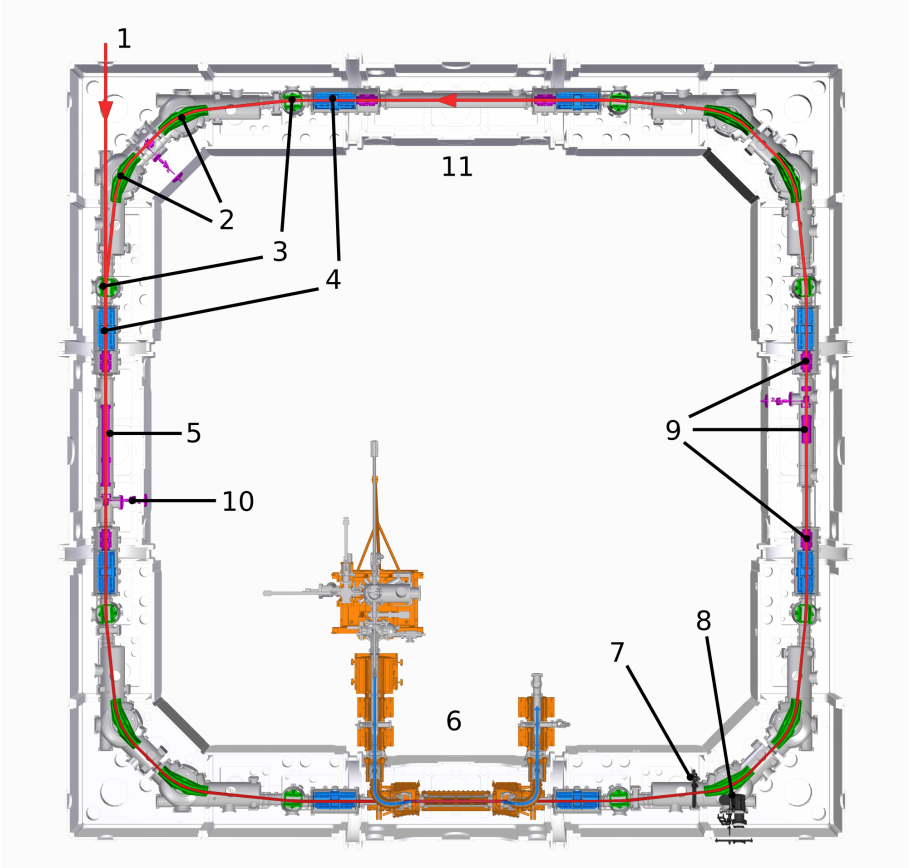

Figure 2.1: Layout of the CSR with: 1 – injection, 2 – 39° deflectors, 3 – 6° deflectors, 4 – focussing quadrupoles, 5 – neutral merging region and rf system, 6 – electron cooler, 7 – COMPACT detector, 8 – NICE detector, 9 – Schottky, current and position pick-ups, 10 – beam viewers, 11 – reaction microscope section. The red arrow indicates the trajectory of the ion beam. Image courtesy of S. Vogel.

The CSR has a circumference of $35\,\mathrm{m}$ and consists of four straight sections connected by four rectangular 90° corners. The latter for their part comprise each of nine individual vacuum chambers, from which eight are arranged symmetrically around the central detector chamber. On both sides this one is followed, first, by a 39° deflector, then by another detector chamber, a 6° deflector and finally by a quadrupole doublet for focussing. This set-up allows for the separation of fragments from dissociative processes happening in the preceding experimental section. The maximum electric rigidity of the beam optics is $600\,\mathrm{kV}$, which according to Eq. 2.8 corresponds to a maximum kinetic energy of $300\,\mathrm{keV}$ per unit charge. The minimum design energy is $20\,\mathrm{keV}$.

Particles stored in the CSR will be of very low velocities. Since they are charged particles, their trajectories can be very easily disturbed by magnetic fields. In order to keep this effect as small as possible, all materials in vicinity of the beamline are required to have a low magnetic permeability of $\mu \leq 1.01$ (1.05 for welding seams) [71]. In addition, this leaves the possibility to install coils to compensate for the earth's magnetic field.

From the four straight sections of the CSR, three are foreseen for experiments while the fourth is reserved for beam diagnostics. The first one behind injection serves for studying the interaction between ions and neutral atoms. The latter are produced by laser stripping of anions prior to injection, and then they are overlapped with the stored beam in a merged-beam geometry. More information on the neutral interaction beamline, which will be available from 2016, can be found in [5, 23]. This section also features a radio-frequency (rf) system, which can be used to bunch the beam.

The second straight section will house the low-energy electron cooler, which is described in more detail in Chapter 3. However, for the first cold beamtime (March - August 2015) this segment served as a laser interaction section. With two different lasers, a tunable optical parametric oscillator (OPO) laser and a continuous He-Ne-laser ($633\,\mathrm{nm}$) first experiments on photodetachment and the dissociation of molecular ions have been performed. The following corner accommodates two detectors. The NICE (**N**eutral **I**maging in **c**ryogenic **e**nvironment) detector serves to distinguish quasi-coincident neutral fragments. Its design consists of a multi-channel plate (MCP) backed by an imaging system composed of a phosphor screen and a fast camera. Additionally, charged reaction products can be observed with the COMPACT (**Co**ld **m**ovable **pa**rticle **c**oun**t**er) detector, which is situated behind the first 6° deflector. It detects single particles with an aluminium converter cathode and a MCP-anode stack and can be moved across the CSR beamline. Information on the two detectors can be found in [4, 65].

The third section is exclusively allotted to beam diagnostics. It features a Schottky pick-up, a current monitor for bunched ion beams and a beam viewer. Of the latter, two more are positioned in the first straight section and the injection corner. Together they form the CSR's destructive, single-turn beam-imaging system. In addition, six position monitors are distributed over all straight sections except for the one where the electron cooler is located. Each of them consists of a vertical and a horizontal capacitive pick-up electrode pair. In the electron cooler section the beam position determination is done with the help of rotating wire scanners (see Chapter 4). For information on the beam diagnosis see also [22].

The fourth section, finally, is planned to house a reaction microscope [73].

2.3.2 Cryogenic and vacuum technology

As mentioned above, the beamline of the CSR can be evacuated to pressures below $10^{-13}\,\mathrm{mbar}$ and cooled down to temperatures below $10\,\mathrm{K}$. In order to protect this experimental vacuum from external heat input, it is shielded by an onion-like structure. The first part of this comprises of two radiation shields made from aluminium. They are followed by 30 layers of super-insulation and a second vacuum, which is of the order of $10^{-6}\,\mathrm{mbar}$. This isolation vacuum is contained by the outer cryostat chambers. The CSR is made up of 16 of these chambers; three for each corner and one for each straight section.

At very low residual gas densities over 90% of particles are hydrogen molecules [49]. It is only possible to reach the envisaged vacuum pressure when cryo-condensating the $\mathrm{H_2}$ inside the experimental vacuum. For this purpose cryogenic pumping units made from copper blocks have been developed, which extend into the inner vacuum with a large surface [71]. The cooling is achieved with a helium refrigerator system, which is operated in a closed cycle. Tubes located inside the inner radiation shield carry liquid helium to the vacuum chamber walls and the cryopumps, hence, cooling them to below $10\,\mathrm{K}$ and $2\,\mathrm{K}$ respectively. Then, the now gaseous helium is redistributed to the two radiation shields, which, in that way, are kept below $40\,\mathrm{K}$ and $80\,\mathrm{K}$ respectively.

The CSR is also designed to be operated at room temperature. In order to still be able to reach a sufficiently high vacuum of the order of $10^{-11}\,\mathrm{mbar}$, the beamline needs to be bakeable up to temperatures of $250\,^{\circ}\mathrm{C}$. Since the super-insulation material cannot withstand such high temperatures, the outer radiation shield is additionally equipped with water cooling to keep the temperatures there below $100\,^{\circ}\mathrm{C}$ during bake-out.

The extreme temperature changes lead to shrinkage and expansion of all components of the CSR. To minimise the influence of the chambers' thermal shrinkage on the functioning of the ring, all beam optical elements are almost completely mechanically decoupled from the outer as well as the inner vacuum chambers. Therefore, all bending and focussing electrodes are directly upheld by external concrete blocks.

2.4 Electron-ion collision experiments

The more or less rectangular shape of the CSR allows for experiments in merged-beam geometry within the straight sections. As mentioned above this fact will be exploited by overlapping a beam of neutral particles with the stored ion beam in the first experimental section. Another interesting reaction to study is the recombination of a cation with an electron. Therefore, the electron cooler is designed to not only cool the stored beam but to also provide the target electrons for such studies.

There are essentially three different recombination processes. Atomic ions usually recombine by capturing a single electron and emitting the surplus energy $h\nu$ via a photon. This process can either be resonant or not. The direct (non-resonant) reaction of a (multiply) charged ion A^{z+} with an electron

$$\mathrm{A}^{z+} + \mathrm{e}^- \rightarrow \mathrm{A}^{(z-1)+} + h\nu \tag{2.9}$$

is called *radiative recombination*. When it proceeds resonantly over a doubly excited state $[\mathrm{A}^{(z-1)+}]^{**}$, it is called *dielectronic recombination*:

$$\mathrm{A}^{z+} + \mathrm{e}^- \leftrightarrow [\mathrm{A}^{(z-1)+}]^{**} \rightarrow \mathrm{A}^{(z-1)+} + h\nu. \tag{2.10}$$

However, with its low energy, the suppression of the 300 K background by a cryogenic design and the extremely low residual gas densities, the CSR offers an outstanding experimental tool for molecular physics. Molecular ions on the other hand recombine via a mechanism called *dissociative recombination* (DR)[1]:

$$\mathrm{AB}^+ + \mathrm{e}^- \rightarrow \mathrm{A} + \mathrm{B} + \text{kinetic energy}, \tag{2.11}$$

where A and B can be atoms or molecules themselves. The first step of this process is the capture of an electron by a singly-charged molecular ion. In a second step a neutral, excited molecular system forms, which then stabilises by breaking of chemical bonds resulting in the right-hand side of Eq. 2.11. However, this is not the full picture. If AB is not a diatomic molecule, it is by no means obvious which of the chemical bonds will be broken. Taking the example of a triatomic molecule ABC, a priori the following reaction channels are possible:

$$\mathrm{ABC}^+ + \mathrm{e}^- \rightarrow \begin{cases} \mathrm{AB} + \mathrm{C} \\ \mathrm{A} + \mathrm{BC} \\ \mathrm{AC} + \mathrm{B} \\ \mathrm{A} + \mathrm{B} + \mathrm{C} \end{cases} \tag{2.12}$$

plus a different quantity of kinetic energy for every alternative. And still this is not a full description of the products. All of them can be generated in their ground state or in an internally excited state, thus, clearing the way for an even further distinction of reaction channels. A constraint on the potential products and their energy state is, thereby, given by the reaction energy.

Three components contribute to the total energy available for any of the reactions given above. The first one is of course the potential energy of the captured electron. Hence, the minimum energy accessible is the ionisation energy of the corresponding neutral molecule in its ground state [67]. Additionally, the kinetic energy of the collision and the rotational and vibrational internal energy of the reactant molecule can contribute. One of the great advantages of storage rings is that the molecules have time to relax to their vibrational ground state. The CSR now offers the possibility to not only perform experiments with ions that are in their complete rovibrational ground state but to do so in a merged-beam geometry. The latter allows for recombination events with very low collision energies and an excellent energy resolution (see Sec. 3.5). Thus, the CSR renders an optimal apparatus to control the initial conditions of a DR experiment.

[1] In the literature both dielectric recombination and dissociative recombination are abbreviated with DR. Within this work, however, it exclusively refers to the latter.

Candidates for first DR studies at CSR are members of the hydrogen ion family, such as HD^+, HeH^+ and H_3^+ [31, 67]. They are not only of high importance for the chemistry of the interstellar medium [67] but have also been subject to extensive theoretical investigation. For all three molecules theoretical DR rate coefficients exist [17, 25, 13], but so far it has only been possible to compare them to experimental data obtained at non-cryogenic temperatures.

Another direction of research would be to take advantage of CSR's electrostatic design and conduct experiments with heavier molecules, one example being biomolecular ions. It has already been shown that these can be stored in an electrostatic storage ring [3, 66], now their interaction with electrons could be studied in order to gain a deeper insight into fundamental biological processes. A second type of interesting heavier species are carbon fluorine ions CF_n^+. CF_4 is a basic component of plasmas used for the etching of silicon, which is an important step in integrated circuit manufacturing [19]. In addition, CF^+ plays an essential role in the chemistry of the interstellar medium [43]. In order to successfully model these plasmas, absolute DR rate coefficients are needed [43]. CSR could extend the knowledge gained from previous measurements at room temperature set-ups [14, 42, 43].

Chapter 3

The CSR electron cooler

From 2016 on the CSR will feature a low-energy electron cooler, the so-called *eCool*. As mentioned above it will be located in the second straight section after injection (cf. Fig. 2.1). Apart from performing phase space cooling on stored ion beams, it will also serve as a target for experiments with positively charged particles. I elaborate on the physics behind both these functions in the following sections 3.2 and 3.5. Additionally, the layout of the cooler is described in detail in Sec. 3.3.

3.1 How to describe stored particle beams

To be able to explain phase space cooling, first some general characteristics of stored particle beams need to be introduced. In general I follow here the nomenclature of Hinterberger [26].

3.1.1 Coordinate systems

All particle trajectories are described as deviations from the design orbit. The latter is represented by the coordinate s, which has a random, but fixed origin along the storage ring's circumference. At any given value of s a coordinate system perpendicular to it can be introduced with the radial and vertical coordinates x and y. Thus, a single particle's spatial position is fully described by the vector (x, y, s). Note that these are curvilinear coordinates.

For the entire definition of a particle in phase space six coordinates are necessary. Instead of using three spatial and three linear momentum coordinates, these can be represented by a vector of the following form:

$$\vec{x}(s) = \begin{pmatrix} x \\ x' \\ y \\ y' \\ l \\ \delta \end{pmatrix} \tag{3.1}$$

with x and y being the spatial deviations from the design orbit as introduced above.

$$x' = \frac{\mathrm{d}x}{\mathrm{d}s}, \quad y' = \frac{\mathrm{d}y}{\mathrm{d}s} \tag{3.2}$$

are the corresponding angular deviations.

$$l = -v_0(t - t_0), \quad \delta = \frac{p - p_0}{p_0}, \tag{3.3}$$

define the longitudinal spatial deviation and the relative momentum deviation from the design particle. v is the particle's velocity, p its momentum and t the time when it passes a certain point s. The index 0 indicates the design particle.

3.1.2 Phase space ellipses and Liouville's theorem

Let us for simplification only consider two phase space coordinates x and x' at a fixed point s for the moment. The trajectory of a single particle in this two-dimensional phase space follows the edge of an ellipse. This ellipse is called single-particle *phase space ellipse*. Thereby, its shape depends on s while its area stays constant. The area divided by π is called single-particle *emittance*.

A particle beam is the overlap of many single-particle trajectories. It is fully described by the six-dimensional density distribution $\rho(x, x', y, y', l, \delta)$. In order to study the transversal beam dynamics, the projections on the radial and vertical coordinates, i.e. $\rho(x, x')$ and $\rho(y, y')$ can be treated independently. At a fixed point s the two-dimensional phase space coordinates of all particles lie within an ellipse. This many-particle phase space ellipse can be represented by a symmetric matrix σ_i with $i = x, y$:

$$\sigma_i = \begin{pmatrix} \sigma_{11} & \sigma_{12} \\ \sigma_{12} & \sigma_{22} \end{pmatrix}. \tag{3.4}$$

Since the formalism in x and y is exactly the same, from now on all formulas will be exemplarily written for the radial coordinate x. Here, the diagonal elements correspond to the maximum spatial and angular deviations of the beam:

$$x_{max} = \sqrt{\sigma_{11}}, \quad x'_{max} = \sqrt{\sigma_{22}}. \tag{3.5}$$

The off-diagonal elements give the strength of the correlation between x and x' inside the beam. In analogy to the single-particle emittance, the area of the phase space ellipse divided by π is called the *beam emittance* ϵ_x[1]. The smaller the emittance the smaller is the spread around the central design particle. Hence, the value of the emittance is one parameter for evaluating the beam quality.

In many cases the particles are not distributed homogeneously in phase space. Instead, a two-dimensional Gaussian density distribution

$$\rho(\vec{x}) = \frac{1}{2\pi\epsilon_x^{1\sigma}} \exp\left(-\frac{1}{2}\vec{x}^{\,T}\sigma_x^{-1}\vec{x}\right), \tag{3.6}$$

with $\vec{x} = \begin{pmatrix} x \\ x' \end{pmatrix}$, can be assumed[2]. One can then define phase space ellipses by lines of equal density. $\vec{x}^{\,T}\sigma_x^{-1}\vec{x} = 1$ for example denotes the ellipse, where the density is decreased by a factor of $\exp(-1/2)$ compared to the centre. This corresponds to one standard deviation 1σ. The emittance of this phase space ellipse is accordingly called the 1σ-emittance $\epsilon_x^{1\sigma}$. It includes $39.3\,\%$ of the total intensity. The 2σ-emittance $\epsilon_x^{2\sigma}$ contains $86.5\,\%$ and the 3σ-emittance $\epsilon_x^{3\sigma}$ $98.9\,\%$.

Statistical mechanics states that, if all active forces can be derived from a Hamiltonian, then the density distribution along any phase space trajectory is constant [59], i.e.

$$\frac{\mathrm{d}\rho}{\mathrm{d}t} = 0. \tag{3.7}$$

This is known as *Liouville's theorem*. An equivalent formulation is that the volume occupied by an ensemble of particles in phase space is always constant. This means that, although a phase space ellipse (and also the six-dimensional phase space ellipsoid) may change its shape, the emittance stays constant.

3.1.3 The betatron function and the machine ellipse

Now, the particle beam generally does not traverse through empty space, but is confined in a storage ring. The field properties of the beam optical elements, spatial constraints by instrumentation and finally the vacuum pipe define the phase space accessible for the particles. It also takes the form of an ellipse, the so-called *machine ellipse* σ_m. Its form is determined by the optical functions

$$\alpha_i(s), \quad \beta_i(s), \quad \gamma_i(s) \qquad i = x,\ y, \tag{3.8}$$

[1] The term *emittance* needs to be handled with care because its definition is somewhat ambiguous. First, it can refer either to a single particle or to the whole beam. Second, the area of the phase space ellipse is often defined as the emittance, which can be written as $E_x = \pi\epsilon_x$. In this work the term, however, always refers to ϵ_x itself.

[2] From now on we will always make this assumption.

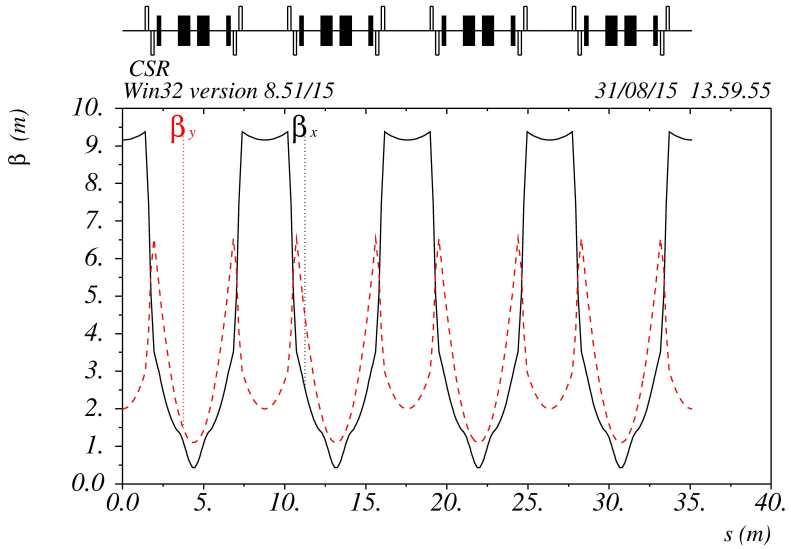

Figure 3.1: The simulated horizontal $\beta_x(s)$ and vertical $\beta_y(s)$ betafunctions of the CSR at the standard working point. On top the optical lattice is shown. The filled rectangles are the deflectors; the open ones are the quadrupoles. (from [20])

which provide one way of describing the optical lattice of the individual storage ring. Ideally the phase space ellipse of the stored beam equals the machine ellipse, which then can be written as

$$\sigma_x = \sigma_m = \epsilon_x^{1\sigma} \begin{pmatrix} \beta_x(s) & -\alpha_x(s) \\ -\alpha_x(s) & \gamma_x(s) \end{pmatrix}. \tag{3.9}$$

The *betatron function* (also simply called betafunction) $\beta_i(s)$ describes the betatron oscillations of the particles. These are horizontal and vertical oscillations around the design orbit [26], which occur in every storage ring. They lead to the fact that a single particle is situated on a different point on the phase space ellipse after every revolution in the ring. The simulated horizontal and vertical betafunctions of the CSR are shown in Fig. 3.1. Note that the cooler is located in one of the sections free from beam optical elements. In this straight section $\beta_x(s)$ is significantly larger than $\beta_y(s)$.

The other optical functions can be derived from the corresponding betafunction (now dropping the index):

$$\alpha(s) = -\frac{1}{2}\beta'(s), \tag{3.10}$$

$$\gamma(s) = \frac{1+\alpha^2(s)}{\beta(s)} = \frac{1+(\beta'/2)^2}{\beta(s)}. \tag{3.11}$$

A simulation of $\alpha_x(s)$ and $\alpha_y(s)$ for the CSR's standard working point is depicted in Fig. 3.2. In the straight sections, i.e. also at the position of the eCool, both functions are very close to zero.

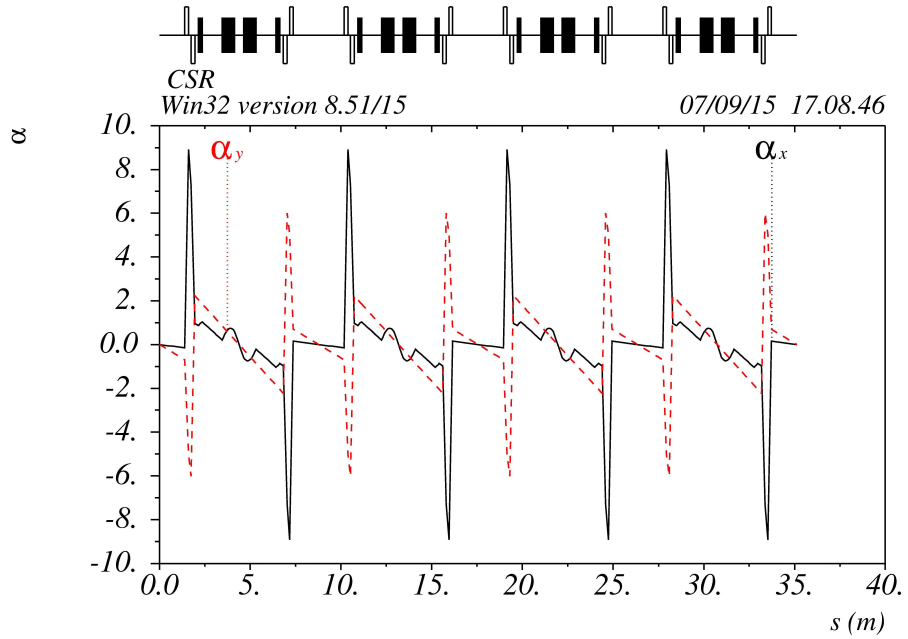

Figure 3.2: The simulated optical functions $\alpha_x(s)$ (horizontal) and $\alpha_y(s)$ (vertical) of the CSR at the standard working point. On top the optical lattice is shown. The filled rectangles are the deflectors; the open ones are the quadrupoles. (from [20])

The emittance of the largest phase space ellipse that can still be stored in the ring is called the *acceptance* A. The horizontal and vertical acceptances of the CSR have been calculated by Fadil et al. [16]:

$$\begin{aligned} A_x &= 120\,\text{mm mrad} \\ A_y &= 180\,\text{mm mrad}. \end{aligned} \tag{3.12}$$

3.2 Phase space cooling

Phase space cooling is a superordinate term for a number of methods that aim for the reduction of the beam cross section, the angular deviations and the momentum spread by extracting energy from the system [69]. Hence, the particle density can be increased allowing for the accumulation of many particles, which is especially interesting for rare particles, for example antiprotons [36]. Other benefits are the possibility to prepare highly collimated beams for precision experiments and the preservation of the beam intensity and quality by compensation of heating effects [35]. The three common techniques to cool beams in storage rings are

1. radiation of *synchrotron light* for electrons and positrons [55],
2. *stochastic cooling* [68] and
3. *electron cooling* for all heavier particles.

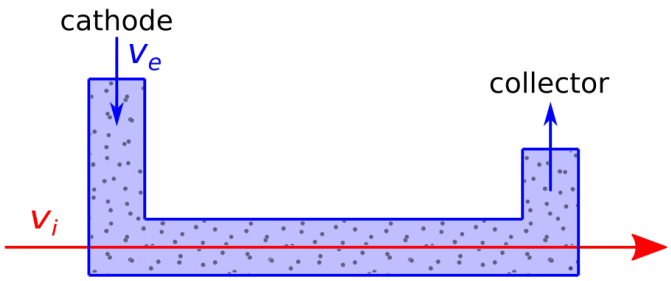

Figure 3.3: Principle of electron cooling. The stored ion beam (red arrow) of mean velocity v_i is merged with a cold electron beam (blue) of equal mean velocity $v_e = v_i$. Via Coulomb interactions a heat exchange between electrons and ions takes place. Since electrons are constantly reproduced at the cathode, this decreases the phase space occupied by the ions.

The first point listed leads to a reduction of energy and, therefore, total momentum. This energy loss is compensated for by rf-acceleration, which, however, only increases the longitudinal momentum. The momentum spread and, hence, the transverse emittances are decreased. Stochastic cooling uses an electronic feedback loop to first detect the position of a test particle and then correct the angular deviation with a kicker. That way betatron oscillations and the momentum spread can be damped. The cooling method employed at CSR though is electron cooling.

Fig. 3.3 schematically shows a set-up for electron cooling. The electrons are produced at a cathode, then overlapped with the stored ion beam and, finally, deflected from the ring again. If the electrons travel at a mean velocity $\vec{v}_e$ and the ions at a mean velocity $\vec{v}_i$, then the relative velocity can be expressed as

$$\begin{aligned} \vec{v}_r &= \vec{v}_e - \vec{v}_i \\ \Longrightarrow v_r &= \sqrt{v_e^2 + v_i^2 - 2v_e v_i \cos\phi}, \end{aligned} \tag{3.13}$$

where ϕ is the angle between the two beams in the interaction region. However, electron cooling is usually happening in a merged-beam geometry. That means that the electron beam is aimed to be merged with the ions in such a way that $\phi = 0$. This given, the electron velocity can be tuned such that the interaction happens at zero relative velocity, i.e.

$$v_e = v_i. \tag{3.14}$$

Via Coulomb interactions the ions and electrons exchange heat. Since the latter are constantly reproduced at the cathode, the longitudinal and transversal velocity deviations of the ion beam decrease. This means that the phase space occupied by the particles becomes smaller.

In the common centre-of-mass frame (cm) of the two beams, it can be assumed that both beams are described by the Maxwell-Boltzmann distribution with mean thermal velocities

$$\langle v_{e,cm} \rangle = \sqrt{\frac{k_B T_e}{m}}, \quad \langle v_{i,cm} \rangle = \sqrt{\frac{k_B T_i}{M}}, \tag{3.15}$$

where k_B is the Boltzmann constant, m and M are the electron and ion mass respectively and T_e and T_i are the corresponding beam temperatures. Thus, the beams can be treated as a plasma that undergoes thermalisation. Since the electron temperature stays fixed, the ion temperature converges exponentially towards it with the time constant [63]

$$\tau_{cool} = \frac{3(4\pi\epsilon_0)^2 mM}{8\sqrt{2\pi} n_e Z^2 e^4 L_C} \left(\frac{k_B T_i}{M} + \frac{k_B T_e}{m} \right)^{3/2}. \tag{3.16}$$

Herein, ϵ_0 is the vacuum permittivity, n_e the electron density, Z the charge state of the ions and L_C the Coulomb logarithm [30] with a numerical value of about 3 to 6. Noteworthy here is that electron cooling is faster for already cold ion beams.

The cooling is counteracted by heating, which increases the velocity spread of the ions. Relevant heating effects in a storage ring are residual gas collisions, intra-beam scattering and interactions with a potential internal target. Hence, τ_{cool} must not be too large. For the conditions in the CSR the influence of T_i on the cooling time can be neglected because the thermal velocities of any stored molecular ions are much smaller than the one of the electrons. For the sake of clarity all numerical parameters are omitted so that the main dependencies of τ_{cool} summarise to

$$\tau_{cool} \propto \frac{M T_e^{3/2}}{n_e Z^2}. \tag{3.17}$$

Molecular ions cannot easily be produced in a charge state larger than one because this usually results in the breaking of chemical bonds. In addition, the mass of the ions desired to be investigated can be quite high ($M \gg 10\,\mathrm{u}$). This greatly increases the cooling time compared to highly charged atomic ions. To counterbalance this effect, the electron temperature needs to be low. On the other hand, as will be shown below, this, together with other impacts, limits the electron density. Therefore, it is especially important that the ion beam completely overlaps with the electron beam.

Ideally, electron cooling leads to equal electron and ion beam temperatures. In equilibrium the transverse angular deviations are given by [50]

$$x_i' = \sqrt{\frac{m}{M}} x_e', \quad y_i' = \sqrt{\frac{m}{M}} y_e', \tag{3.18}$$

where x_e' and y_e' represent the transverse angular spread of the electron beam. Considering the great mass difference between electrons and any ion, thus, highly collimated ion beams can be produced.

3.3 Cold electron production

From the requirement of equal velocities (Eq. 3.14), a relation between the kinetic energy of the ions E_i and the kinetic energy of the electrons, the so-called *cooling energy* E_{cool}, can be withdrawn:

$$E_{cool} = \frac{m}{M} \cdot E_i. \tag{3.19}$$

Recalling the low design energy of the CSR (20 keV to 300 keV per unit charge), this equation reveals one of the challenges for the eCool: The electrons need to be very slow. Typical values for a 300 keV beam are 163 eV for protons, < 20 eV for most molecular ions and around 1 eV for ions with $M = 160$ u, which is the highest mass that can still be phase space cooled with the eCool [62].

The second challenge has already been anticipated in the last section. In order to efficiently cool a stored ion beam, the electron temperature must be very low. Both of these requirements are met by using an electron gun based on emission from gallium arsenide (GaAs) semiconductor photocathodes [45] together with *adiabatic magnetic transverse expansion* [47]. Such a set-up has been employed at the MPIK before; at the TSR electron target [72]. The photocathode has been extensively characterised [30, 46] and successfully utilised in experiments and will, thus, be transferred to the CSR eCool.

3.3.1 The GaAs photocathode

The most common technique to produce electron beams is thermionic emission. Typically a metal filament is heated so that the free electrons of the material gain enough thermal energy to overcome the material's work function, and, thus, are able to leave the cathode. The cathode work function W_c is, hereby, defined as the energy difference between the Fermi level E_F and the lowest unbound vacuum state. However, as described in Richardson's law

$$J = A_G \cdot T_c^2 \exp\left(-\frac{W_c}{k_B T_c}\right), \tag{3.20}$$

the emitted current density J strongly depends on the cathode temperature T_c, with A_G only being a parameter characteristic for the cathode material. For metals this method is, therefore, only efficient for temperatures of around 1200 K to 1500 K [64]. The velocities of the emitted electrons form a Maxwell-Boltzmann distribution (cf. Eq. 3.15), with the temperature T_e given by the cathode temperature. Production of cold electrons with a low velocity spread is, hence, not feasible with thermionic emission.

In photocathodes, on the other hand, electrons gain the energy to overcome the work function by absorbing a photon. These photons are provided by a laser of small power ($\leq$ 1 W [48]). When the cathode is additionally cooled, its temperature and, hence, the electron beam temperature can reach values below 100 K.

The photocathodes that will be used in the eCool are made from GaAs crystals doped with zinc. In order to be able to extract electrons from the cathode material, the vacuum energy level E_{vac} should lie below the lowest state of the conducting band E_{CB}. Scheer and van Laar have shown that a monolayer of caesium and oxygen on a semiconductor's surface leads to a bending of the band structure [56]. This is illustrated in Fig. 3.4. Then, the vacuum level is indeed located below the conducting band so that the electrons can

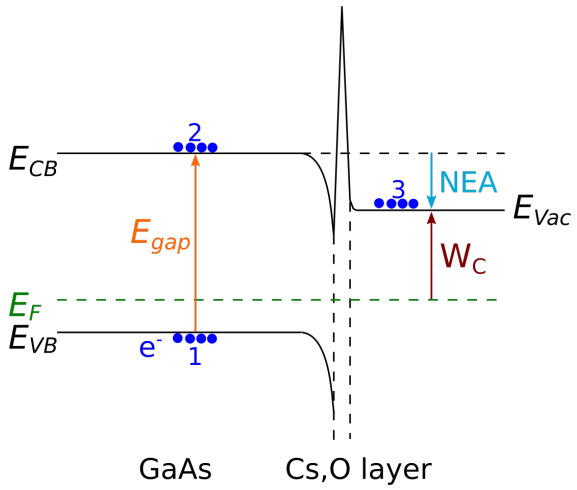

Figure 3.4: Energy levels in a NEA GaAs photocathode. Laser light with an energy $h\nu \geq E_{gap}$ raises the electrons from the valence band E_{VB} to the conducting band E_{CB}. Due to the (Cs,O) coating, the band structure is bent into a NEA state. This way, the electrons can tunnel through the thin surface barrier into the vacuum E_{vac}.

leave the crystal by tunnelling through the thin surface barrier. This state is referred to as ***n**egative **e**lectron **a**ffinity (NEA)*.

The GaAs crystal is mounted on a transparent sapphire socket and operated in transmission mode. In a first step, the laser light with an energy of $h\nu \geq E_{gap}$ raises the electrons from the valence band to the conducting band. From there they escape by tunnelling. In front of the cathode surface the electrons accumulate in a cloud generating space charge. It has been shown that the electron energy spread, when operating the phtotocathode in such a space charge mode, is determined by the GaAs temperature [48]. For room temperature operation this accounts for $k_B T_e = 25\,\mathrm{meV}$. When cooling the cathode with liquid nitrogen to $90\,\mathrm{K}$, this value can be lowered to $8\,\mathrm{meV}$ [48].

The electron beam is extracted and accelerated by a number of electrodes arranged in a *Pierce geometry* [53, 62]. The geometry of these electrodes can be merged into a single parameter called *perveance* P $\left([P] = 1\,\mathrm{Perv} = 1\,\mathrm{AV}^{-3/2}\right)$. The extraction voltage U_{ext} can, thereby, be chosen in such a way that extraction from the electron cloud and emission from the cathode into the same are in equilibrium. This is the so-called space charge mode already mentioned above. The extracted electron current is then given by

$$I = P U_{ext}^{3/2}, \tag{3.21}$$

which, noteworthy, does not depend on the cathode temperature.

3.3.2 Adiabatic magnetic transverse expansion

So far we have neglected that, although the CSR is an electrostatic storage ring, the electrons in the cooler are guided by a longitudinal magnetic field. Due to the Lorentz force (Eq. 2.1), the particles' motion is

divided into a translation parallel to the field lines and a rotation around the same (see Sec. 5.1.3 for a more detailed description). Hence, the beam temperature and related quantities can be separated into a longitudinal and a transverse component (denoted by $||$ and $\perp$ respectively).

Adiabatic transverse expansion (ATE) is a method to efficiently reduce the transverse electron temperature $T_\perp$ in an electron cooler. It was first implemented at the CRYRING facility in Stockholm [11] and successfully employed at the TSR as well [51]. The principle of this technique is to not use a constant guiding field but to decrease the magnetic field strength from an initial value B_i to a smaller one B_f. The ratio of these two quantities is called the *expansion factor* α:

$$\alpha := \frac{B_i}{B_f}, \tag{3.22}$$

which is limited to 20 for the CSR [62] but in principle can be higher. Due to the gradient in the magnetic field strength, the field lines are not parallel anymore, which evokes a longitudinal component of the Lorentz force. Naturally, this leads to a longitudinal acceleration and an increase of the particle's longitudinal energy component $E_{||}$. However, energy needs to be conserved; therefore, this results in the reduction of $E_\perp$. This can be written in the form of *adiabatic invariants* [51]

$$\begin{aligned} \frac{E_\perp}{B} &= \text{const} \\ \implies E_{\perp,f} &= \frac{1}{\alpha} E_{\perp,i}, \end{aligned} \tag{3.23}$$

where the indices i and f denote the initial and final state respectively. Since this relation does not only hold for a single particle but also for a whole ensemble, $E_\perp$ can be replaced with the mean transverse energy $\langle E_\perp \rangle = k_B T_\perp$. The desired decrease of the transverse temperature follows directly:

$$k_B T_{\perp,f} = \frac{1}{\alpha} k_B T_{\perp,i}. \tag{3.24}$$

The mean longitudinal energy and, therefore, the temperature can be measured directly for different combinations of B_i and B_f with the help of a *retarding field analyser*. This instrument is part of the collector and is described in Sec. 5.2.3. The connections outlined above, now, yield a method to also determine the initial transverse energy with such measurements. Using conservation of energy

$$\langle E_{\perp,i} \rangle + \langle E_{||,i} \rangle = \langle E_{\perp,f} \rangle + \langle E_{||,f} \rangle , \tag{3.25}$$

Eq. 3.24 can be converted into

$$\langle E_{\perp,i} \rangle = \frac{\langle E_{||,f} \rangle - \langle E_{||,i} \rangle}{1 - B_f/B_i}. \tag{3.26}$$

The introduced technique has a disadvantage though. Another adiabatic invariant is the magnetic flux through the cross section of the electron beam [51]. ATE, therefore, leads to the eponymous transverse expansion of the beam:

$$R_{e,f} = \sqrt{\alpha} R_{e,i}, \tag{3.27}$$

where R_e denotes the radius of the electron beam. The initial radius $R_{e,i}$ is determined by the geometry of the Pierce electrode, and for our photocathode is has a value of $3\,\mathrm{mm}$. From this equation, however, follows directly the reduction of the electron density

$$n_{e,f} = \frac{1}{\alpha} n_{e,i}. \tag{3.28}$$

Considering the dependence of the cooling time on the density (cf. Eq. 3.17), α thus cannot be chosen arbitrarily high.

3.3.3 Lifetime limiting effect of secondary electrons on the photocathode

It has been shown above that the (Cs,O) layer on the photocathode surface is crucial for effective electron production. Yet, this thin coating can be very quickly destroyed by residual gas constituents like H_2O or CO. First and foremost, excellent vacuum conditions in the cathode section are essential for this reason. By pumping, pressures in the $10^{-11}\,\mathrm{mbar}$ are reached, which in principal is sufficient to reach reasonable cathode lifetimes. However, experiences at the TSR electron target have shown that operation of the set-up can itself lead to local vacuum degradation and fast destruction of the (Cs,O) film [30].

An electron cooler is, in principal, a closed current circuit. This means that all electrons emitted by the cathode should be absorbed by the collector. Due to the magnetic guiding field this is mainly true, but it is inevitable that secondary electrons are produced when the primary beam impinges on the metal of the Faraday cup. Secondaries that carry a large fraction of the primary energy have a finite probability of leaving the collector again. Of course, the magnetic guiding works for them as well as for the primaries; therefore, they travel back to the photocathode. As a result of toroidal drifts in the merging regions (see paragraph below), the particles' direction of motion obtains a small transverse component, which causes the electrons to hit the cathode's extraction and accelerations electrodes [30]. This induces the unwanted release of residual gas from the material.

3.4 Design

Fig. 3.5 shows a model of the electron cooler. It is of U-shape with the cathode and collector sections being placed inside the CSR's circumference. The middle part, where the electron beam is overlapped with the stored ions, is integrated into the same. The electrons are produced with the electron gun as explained in the

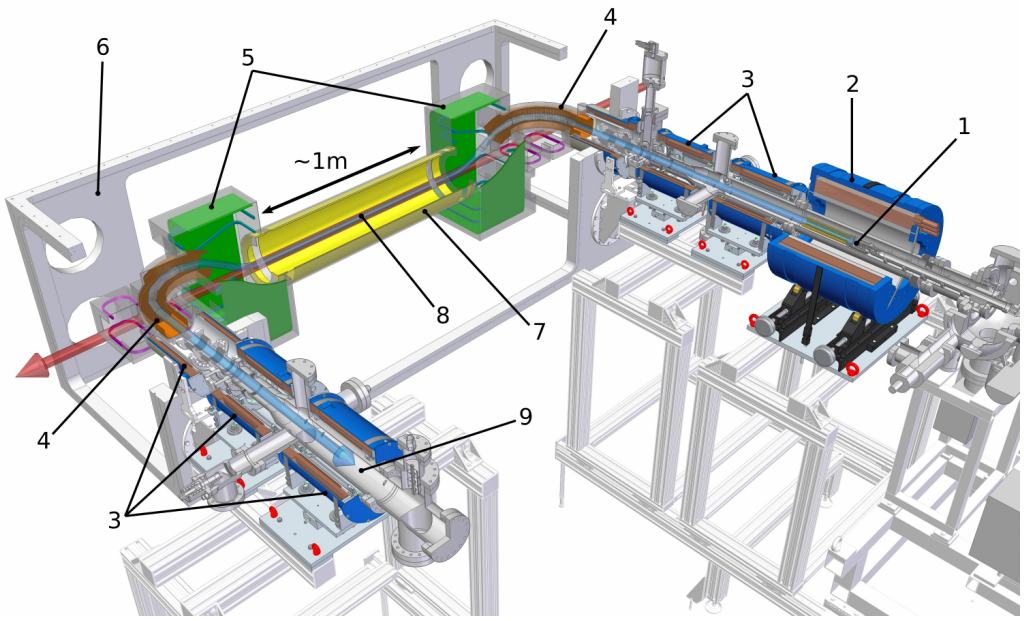

Figure 3.5: Layout of the CSR electron cooler showing: 1 – photoelectron gun, 2 – high field coil (2500 Gs), 3 – low field coils (250 Gs), 4 – toroids, 5 – merging solenoids, 6 – CSR isolation vacuum chamber, 7 – interaction solenoid, 8 – interaction region, 9 – collector region. The red (blue) arrow indicates the ion (electron) trajectory. Image courtesy of S. Vogel.

previous section. The magnetic guiding field is realised by a number of solenoids. The first one as counted from the cathode is a high field solenoid followed by three low field coils to allow for the usage of ATE.

The merging and demerging sections of the cooler are mirror symmetric to each other. They feature the speciality of a new merging scheme, where the electron bending is separated from the actual merging with the ion beam. This has the advantage that the field of the toroid, which is used for the bending process, does not disturb the ion trajectory [62]. The merging is done with the help of the rectangular merging solenoid, a horizontal solenoid and a number of coils producing a vertical magnetic field component. Compensator coils are added as well to account for disturbances of the ion beam. The interaction region itself is enclosed by the cylindrical interaction solenoid. It should be noted that this solenoid is actually split into three parts: one long one in the middle and two short ones at both ends. This leaves two small gaps, which are used for the installation of beam diagnostics in the form of rotating wire scanners (see Chapter 4).

All of the magnets in the merging and interaction section need to be relatively close to the beamline. Since normal-conducting coils would mean an impact of ohmic heat on the cryogenic environment of the CSR's experimental vacuum, it has been decided to use superconducting coils. They are cooled, independently of the CSR, with a cryogenic cooling system based on liquid neon [62, 34]. This, however, produces a new complication. The eCool must always be cooled even when the CSR is operated at room temperature or during bake-out! The experimental vacuum chamber is, therefore, wrapped in a special kind of multilayer isolation, which is bakeable up to 620 K. Onto this follow the superconducting coils and then another wrapping of "normal" multilayer isolation to protect the magnets from room temperature impact.

The third side of the U is made up of the collector section. As on the cathode side, the magnetic guiding field is provided by three low field solenoids. The collector itself is described in detail in Chapter 5.

It is worth mentioning that both the cathode and the collector section are non-cryogenic. Only the magnets, which are built up of copper coils, are water cooled. This means a direct connection between the cryogenic environment of the beamline and the room temperature vacuum of those sections. The merging regions are equipped with additional cryogenic pumping units for this reason. Furthermore, cryopumps and non-evaporable getter (NEG) pumps are installed. This way a vacuum around $10^{-11}\,\mathrm{mbar}$ can be reached in the outer eCool sections.

For further details on planning, designing and testing components of the eCool see [62, 70].

3.5 The electron cooler as target

It has been mentioned before that the eCool will also serve as an electron target for electron-ion recombination experiments. The approach to such studies is to measure the *rate coefficient* of the interaction $\langle \sigma v_r \rangle$ as a function of the collision energy E_{coll}. The latter is – in a non-relativistic case[3] – related to the relative velocity, as given in Eq. 3.13, simply by $E_{coll} = m v_r^2/2$. Since it can still be assumed that the angle between the two beams is zero, these two relations can be combined to [32]

$$E_{coll} = \left(\sqrt{E_e} - \sqrt{E_{cool}} \right)^2 . \tag{3.29}$$

Thus, the electron energy E_e, which is regulated via the acceleration voltage of the cooler, fully controls the collision energy. In practice the electron energy is switched between the cooling and measurement energies on short time scales [64] to prevent the ion beam from heating while performing the experiment.

The electron beam produced in the eCool is much larger than the phase space cooled ion beam. Assuming that the latter is, therefore, completely enclosed by the former, the rate coefficient can be expressed as [33]

$$\langle \sigma v_r \rangle = \frac{R}{n_e N_i L_{eff}/C} . \tag{3.30}$$

R is the rate of reaction products measured with a detector following the interaction region. N_i is the total number of ions stored in the ring, which can be determined with the current pick-up installed in the beam diagnostics section of the CSR. Since only a fraction of these ions actually interacts with the electrons, this number has to be scaled with the ratio of the effective length of the interaction region L_{eff} to the circumference of the ring C. n_e is the density of the electron beam. It can be calculated from the total electron current and the beam profile, which can both be measured at the collector. Eq. 3.30, hence, provides the relation how to determine the rate coefficient experimentally.

[3] This conditions holds always true for the CSR.

Formally, the rate coefficient is expressed as an integral over the interaction cross section σ times the relative velocity distribution [32]. Due to the large mass difference between ions and electrons, the velocity spread of the former can be neglected [33] so that the velocity resolution is completely governed by the thermal energy spread in the electron beam. The resolution of the collision energy is then given by [39]

$$\delta E_{coll} = \sqrt{\left(k_B T_{e\perp} \ln 2\right)^2 + 16 E_{coll} k_B T_{e||} \ln 2}. \tag{3.31}$$

This emphasises the importance of a low transverse temperature, which can be obtained by using a cold photocathode in combination with ATE.

Chapter 4

Beam positioning with rotating wire scanners

It has been explained in the previous chapters that the complete overlap of the electron and the ion beam in the interaction region is essential for both electron cooling and the realisation of recombination experiments. In order to achieve this, the centres of the beams have to be aligned. This is only possible if a system for beam position determination is present. However, due to spatial limitations, no pick-up electrodes (cf. Sec. 2.3) can be installed in the eCool section. Therefore, a different solution had to be found.

A common method to obtain the vertical and horizontal beam location is to measure the current signal, which is induced when a thin, conducting object, such as a wire, transverses the beam. Devices which perform such measurements are called rotating wire scanners. In practice either single-wire scanners [6, 27, 28], which perform two orthogonal scans, or dual-wire scanners [61], which can cover two spatial coordinates with one scan, are used. Since electrons are constantly reproduced at the photocathode, they produce a current high enough for this technique to be employed. The ion beam intensity, however, is not high enough, so the problem has to be approached differently. In this case, the wires are used as so-called scrapers, which restrain the ion beam phase space and, thus, cut away part of the beam. The decrease in ion intensity can then be measured as a function of the progressing rotation.

The CSR eCool is equipped with two dual-wire scanners. They are both used for position determination of the electron as well as the ion beam. Fig. 4.1 illustrates their location at both ends of the interaction region. Also indicated are the trajectories of both beams. It is important to note that they are completely merged at the site of the scanners. Otherwise, it would be more complicated to test for their alignment in the interaction region. A model of one wire scanner is depicted in Fig. 4.2. Their mechanical design is described in Sec. 4.1.

During a measurement the only information available from outside is the position of the scanner determined by its angle of rotation α. Part of this work has been to study how the spatial position of the beam can be withdrawn from this. Sec. 4.2 first gives a fully mathematical description of the pair of wires and then

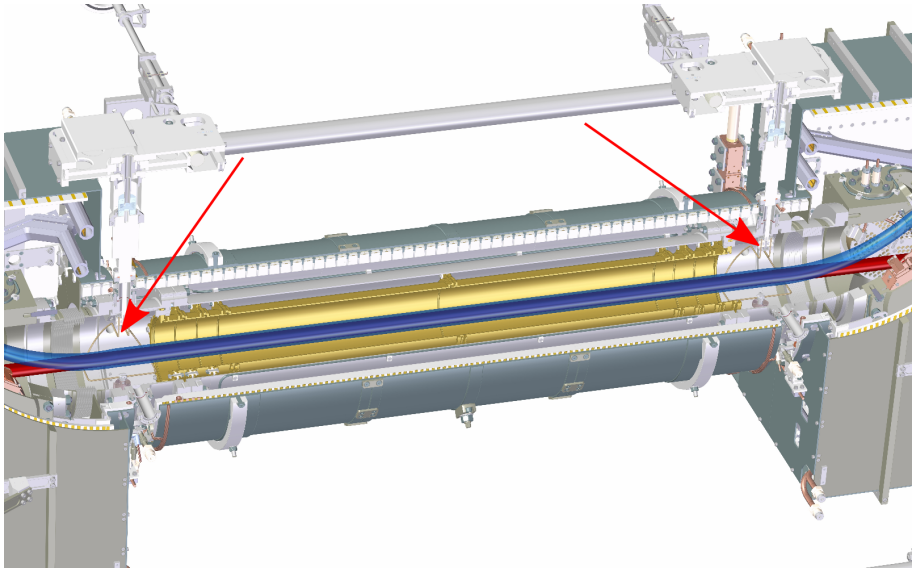

Figure 4.1: Shown is the interaction region of the eCool. The red arrows point to the wire scanners. The ion and electron beam trajectories are illustrated in red and blue respectively. Note that they completely overlap at the scanners' locations. Image courtesy of S. Vogel.

establishes a procedure for calculating the transverse beam position from two measured angles. This is then transferred in Sec. 4.3 to two different techniques to either determine the location of the electron or ion beam.

4.1 Mechanical design

Fig. 4.3 displays a side and a front view of one scanner, also giving the corresponding measures. The wire has a diameter of $2\,\mathrm{mm}$ and is made from Inconel X-750. At the top the two ends of the wire are connected by the carrier. The latter's symmetry axis corresponds to the axis of rotation of the scanner. This is also the y-axis in the scanner's local coordinate system, whose origin lies in the centre of the beamline. The x-axis points towards the outside of the CSR. The initial position of both scanners is chosen such that it lies on the left-hand side of the beamline (as seen from the ions' direction of movement). Due to the curvature of the wires, the scanners do not diminish the aperture of the CSR in this position.

Although one scanner is made from one continuous piece of wire, the only parts of it intersecting the beam are the two curves labelled with "R 51.5" in the left-hand side of Fig. 4.3. Therefore, these two are treated as two independent wires in the following. They are arranged as such that the beam position in the transverse plane can be fully determined with one rotation only. The presence of two scanners allows for the detection of unwanted angular divergences across the length of the interaction region. However, since both wire scanner installations are identical to each other, below I will for simplicity only speak of a singular one.

Fig. 4.4 visualises how the scanner is installed at the end of the interaction region. It is mounted inside a feedthrough vacuum chamber, which is placed in the gap between the long and the short interaction

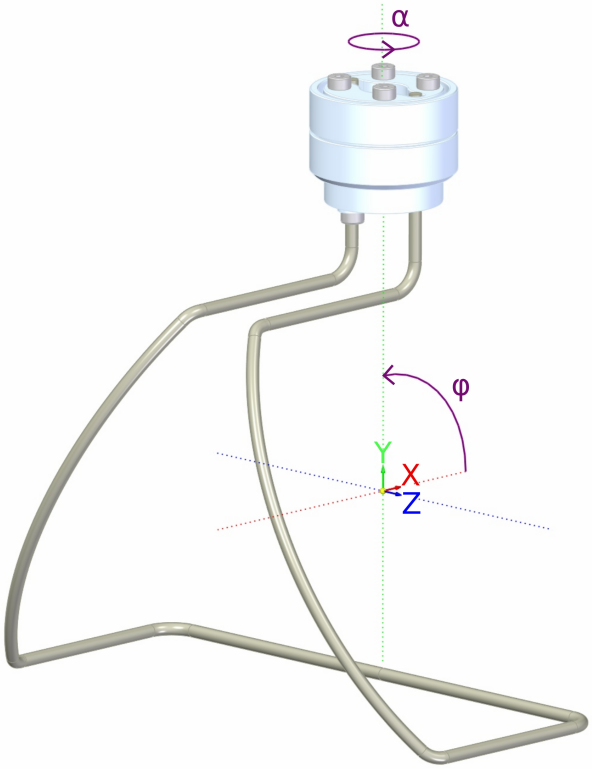

Figure 4.2: Model of one wire scanner. Depicted are the dual-wire design and the carrier. Also shown is the local coordinate system of the wire scanner, which is used for the mathematical description in Sec. 4.2. The y-axis, hereby, corresponds to the rotation axis of the scanner. In its initial position, the x-axis points towards the outside of the CSR.

solenoids. At the bottom the wire is contacted via a balance spring made from titanium. This allows for continuous electrical contact during rotation. However, if the scanner is turned constantly into one direction, the spring will break. Since for beam position determination rotations of $180°$ are sufficient, this does not impose a real problem. Still, the system should be handled with care. An electrical vacuum feedthrough is connected to the spring on the other side so that any charge picked up by the scanner can be transported out of the vacuum. There it can be measured as a current signal.

On top the drive for the rotary motion of the wire scanner is positioned. There are several requirements that have made the development of this drive technically challenging:

1. The rotation angle needs to be adjusted and read out with an accuracy of $1°$. (The demand for this value is motivated in the following section.)
2. Necessity of thermal decoupling between the CSR's experimental vacuum and the outside room temperature environment.
3. Spatial constraints imposed by the neighbouring rectangular merging toroid (see Fig. 4.1).

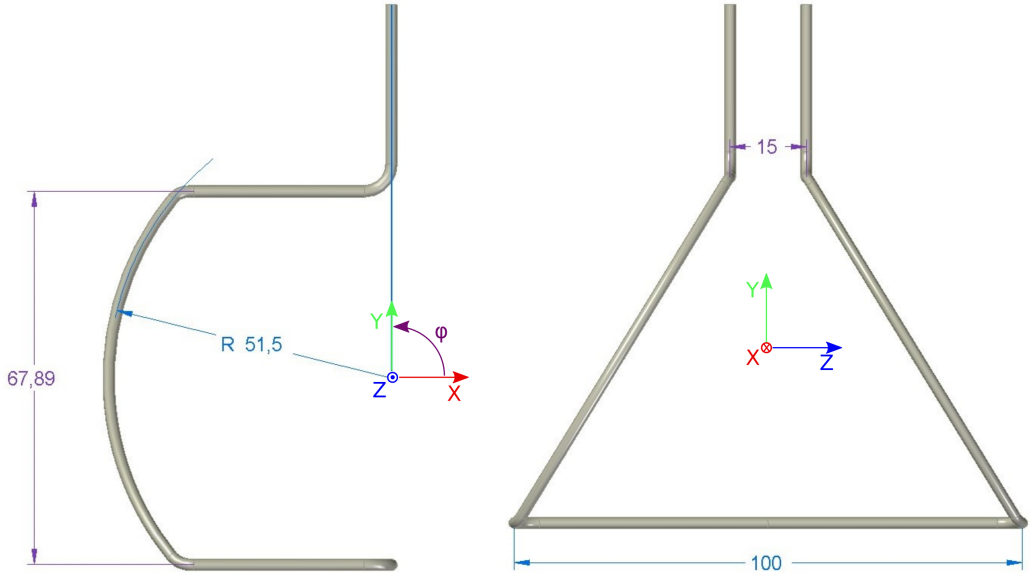

Figure 4.3: Side and front view of the model of the wire scanner. Included are all measures (in mm) that are used for the mathematical description of the scanners. The scanner's local coordinate system is also shown.

The first point is covered by using a worm drive. It consists of a worm gear with 360 teeth and a worm screw with only one tooth. This way a gear transmission ratio of 360 can be achieved. The readout of the angle is, thus, very simple. On the outside a rotation counter counts the number of turns, where each turn corresponds to a rotation of the scanner by 1°. It is foreseen that in the future a stepper motor will set and read out the angle automatically. However, this has not been realised yet. A material combination of aluminium $AlMg_3$ for the gear and polyether ether ketone (PEEK) for the worm screw has been chosen. The latter has been selected because cryogenic tests of the translation mechanics of the COMPACT detector have demonstrated its excellent performance at low temperatures [65].

Previous experience from the design of the CSR detectors has also been exploited to solve the second issue. An intermediate drive very similar to those employed at the COMPACT and the beam viewers is installed between the outer flange and the worm drive. It is mounted on the thermal shield of the cooler (not shown in Fig. 4.4), and allows for transmission of rotary motion from the atmosphere side to the worm screw. The drive shaft is electrically isolated from the mounting. On both sides it ends in a plate holding two carrier pins. The drive is designed in such a way that a full rotation on the outside corresponds to a full rotation on the inside. Partial turns, on the other hand, cannot be as unambiguously translated. That is another reason behind the large transmission ratio of the worm drive. Thermal decoupling is achieved by positioning the drive shaft such that none of the carrier pins makes contact with the respective counterpart. In order to check whether the shaft is really not touching ground potential on either side, a sensor wire is used. It is attached to a titanium spring, which is fixed on the mounting in an electrically isolated manner. This way, almost perfect thermal isolation can be ensured.

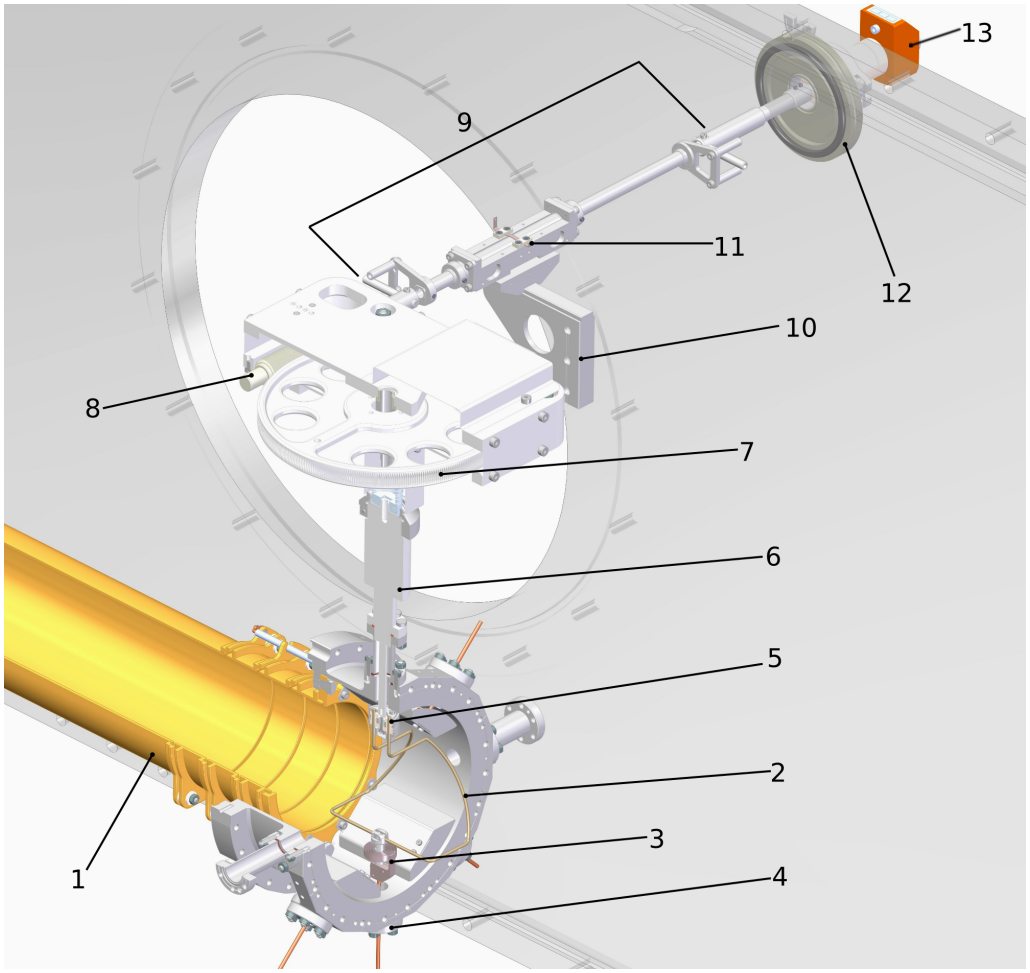

Figure 4.4: Installation of one wire scanner at the end of the interaction region showing: 1 – drift tube, 2 – scanner wire, 3 – balance spring for electrical connection, 4 – electrical vacuum feedthrough, 5 – carrier, 6 – rotary vacuum feedthrough, 7 – worm gear, 8 – worm screw, 9 – intermediate drive for thermal decoupling CSR experimental vacuum/atmosphere, 10 – mounting of intermediate drive on eCool shield, 11 – titanium spring 12 – isolation vacuum flange, 13 – rotation counter. They grey structure in the background is the outer side vacuum flange of the CSR.

The distance between the rotation axis of the scanner and the outer edge of the neighbouring merging toroid is only $36\,\mathrm{mm}$. However, the worm gear needs to have 360 teeth, and thus it is not feasible to manufacture it small enough to fit into this gap. Therefore, it has been decided to place the worm gear above the magnet and to use an accordingly long rotary vacuum feedthrough. The total outer diameter of the now used gear is $181\,\mathrm{mm}$. Its axis of rotation coincides with that of the scanner. Due to the functional principle of the worm gear, the rotation axis of the worm screw is perpendicular to that. This makes it possible to place the connection of the drive shaft to the outside on the outer side shield of the CSR, which is much easier accessible than the top shield.

Due to the intermediate drive, it is not possible to determine the initial position of the wire scanner from outside. On account of this, the worm gear features a screw that establishes an electrical link with one of two contact latches once per $180°$ turn. When assembling the scanner and the drive, it is, thus, highly

Parameter	Value
Radius R	$51.50\,\mathrm{mm}$
a	$59.060\,59\,\mathrm{mm}$
c	$-128.044\,19\,\mathrm{mm}$
φ_{min}	$2.421\,94\,\mathrm{rad}$
φ_{max}	$3.861\,25\,\mathrm{rad}$

Table 4.1: Parameters for the mathematical description of the wire scanners. All values are withdrawn from the model of the scanner as it is shown in Fig. 4.3.

important to define the position of the screw relative to the wire! The gear, the rotary feedthrough and the surrounding mounting elements are grounded. The contact latches are made from titanium, but they are attached to the mounting in an electrically isolating manner. That way contact between the screw and the latch can be detected with a resistance measurement. Since the wire itself is isolated from the rotary feedthrough, this is independent of any measurements performed with the scanner.

4.2 Mathematical model for beam position determination

The aim of this section is to find a scheme how the beam position can be determined from the scanner's angle of rotation. At first we only consider a single point with coordinates (x, y) in a plane transverse to the beam's direction of movement. The spatial extensions of the ion and electron beams are covered in the next section.

In the following each single wire is treated as a non-extended line in three-dimensional space. In the coordinate system as depicted in Fig. 4.2, the front wire (assuming a counter-clockwise rotation) can then be described by the vector

$$\overrightarrow{sc1}(\varphi) = \begin{pmatrix} R\cos(\varphi) \\ R\sin(\varphi) \\ 1/2(a\varphi + c) \end{pmatrix}. \tag{4.1}$$

Respectively, the back wire is described by

$$\overrightarrow{sc2}(\varphi) = \begin{pmatrix} R\cos(\varphi) \\ R\sin(\varphi) \\ -1/2(a\varphi + c) \end{pmatrix}, \tag{4.2}$$

where R, a and c are constants given in Table 4.1. One wire is made up of all the points where $\varphi_{min} \leq \varphi \leq \varphi_{max}$ with φ_{min} and φ_{max} also given in the same table. All values are taken from the model of the wire scanner shown in Fig. 4.3.

A rotation around the y-axis by an angle α can be represented by the corresponding rotation matrix

$$R_y(\alpha) = \begin{pmatrix} \cos(\alpha) & 0 & \sin(\alpha) \\ 0 & 1 & 0 \\ -\sin(\alpha) & 0 & \cos(\alpha) \end{pmatrix}. \tag{4.3}$$

After a rotation by an angle α_1, which is equal to the matrix multiplication of $R_y(\alpha)$ with $\overrightarrow{sc1}(\varphi)$, the x-coordinate of the first wire is given by

$$x_{sc1} = R\cos(\alpha_1)\cos(\varphi) + \frac{1}{2}\sin(\alpha_1)(a\varphi + c). \tag{4.4}$$

Accordingly, the x-coordinate of the back wire after a rotation by an angle α_2 can be written as:

$$x_{sc2} = R\cos(\alpha_2)\cos(\varphi) - \frac{1}{2}\sin(\alpha_2)(a\varphi + c). \tag{4.5}$$

If a beam is present at a position x, an induced current signal will be measured at two angles α_1 and α_2 and

$$x = x_{sc1} = x_{sc2}. \tag{4.6}$$

Then, equations 4.4 and 4.5 form a system of equations with the two unknowns x and φ. The solution is unique due to the restriction of φ. Combined with $y = R\sin(\varphi)$ as stated in equations 4.1 and 4.2, the beam position in a plane perpendicular to the beam direction can, therefore, be deduced from the measured angles $\alpha 1$ and $\alpha 2$.

In order to find a functional relation between a given beam position and the expected experimental result, the mathematical wire scanner model has been simulated with Mathematica [74]. The measured current profile contains two relevant values for beam position determination: the position of the first peak (α_1) and the distance between the two peaks ($\alpha_2 - \alpha_1$). While the latter is purely determined by the vertical position of the beam, the former depends both on x and y. When plotting α_1 over x, this leads to a family of curves for different values of y as shown in Fig. 4.5. Figure 4.6 depicts the dependence of $\alpha_2 - \alpha_1$ on y.

The two wires of one scanner are arranged in such a way that the distance between them constantly decreases as y increases (cf. Fig 4.3 right-hand side). Therefore the decrease in distance between the two angles for a further up positioned beam is as expected. Since the starting position of the wire scanner is at the left-hand side of the beamline, the beam is intersected the earlier the further left it lies. Also, for a fixed value of x, α_1 is greater for a higher lying beam as it is shown in Fig. 4.5. The deviation from this behaviour for very small values of x is due to the not completely linear construction of the scanner. However, for a given combination of α_1 and y, the horizontal coordinate can still be worked out unambiguously.

From figures 4.5 and 4.6 a scheme for determining x and y can be withdrawn. First, the distance between the two measured angles can be used to deduce the vertical position of the beam. Then, the corresponding curve in the x-α_1-plot and the measured value of α_1 can be used to calculate also the horizontal coordinate.

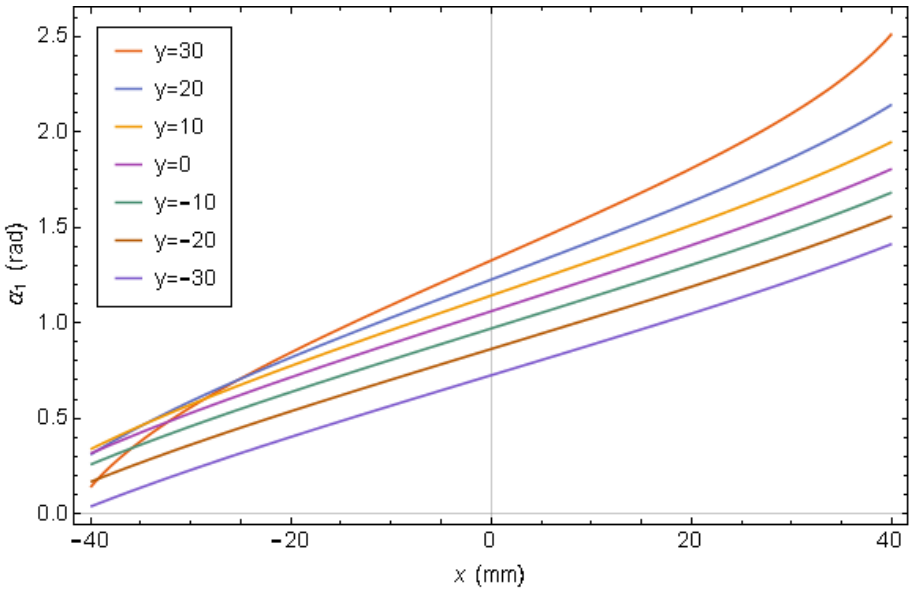

Figure 4.5: Dependence of α_1 on x for different fixed values of y. $(x, y) = (0\,\mathrm{mm}, 0\,\mathrm{mm})$ corresponds to the centre of the beamline. For a beam that is displaced to the left (right) the scanner needs to be rotated less (further) for the first peak to be induced. Also, α_1 is greater for a higher lying beam for most x-values

The Mathematica script shown in Appendix A follows exactly this approach. From two input angles it computes the wanted transverse beam location.

The model can also be used to estimate the spatial resolution achievable with the rotating wire measurement. Since it is not expected for the beam to lie very far away from the beamline centre, the calculated functions for α_1 shown in Fig. 4.5 can be fitted linearly. For determining the resolution only the gradient of the fit is relevant, which around $x = 0$ is almost the same for all curves. Thus, the calculation is done exemplarily at $y = 0$. The function withdrawn from the wire scanner model is shown together with a linear fit in Fig. 4.7.

The linear fit is given by

$$\alpha_1 = 1.061\,64\,\mathrm{rad} + 0.017\,897\,\mathrm{rad\,mm^{-1}}x. \tag{4.7}$$

The requested spatial resolution is $\Delta x = 1\,\mathrm{mm}$. Thus, the required angular resolution $\Delta\alpha$ needs to be 0.018, which corresponds to $\sim 1°$.

4.3 Simulation of the scanners with an extended beam

So far the mathematical description of the wire scanner measurement has been limited to a single point in the x-y-plane leading to two single values for the angles α_1 and α_2. In reality, though, every beam is an object with a macroscopic cross section. When taking this into consideration, the electron beam and the ion beam have to be treated separately due to the different measurement techniques applied.

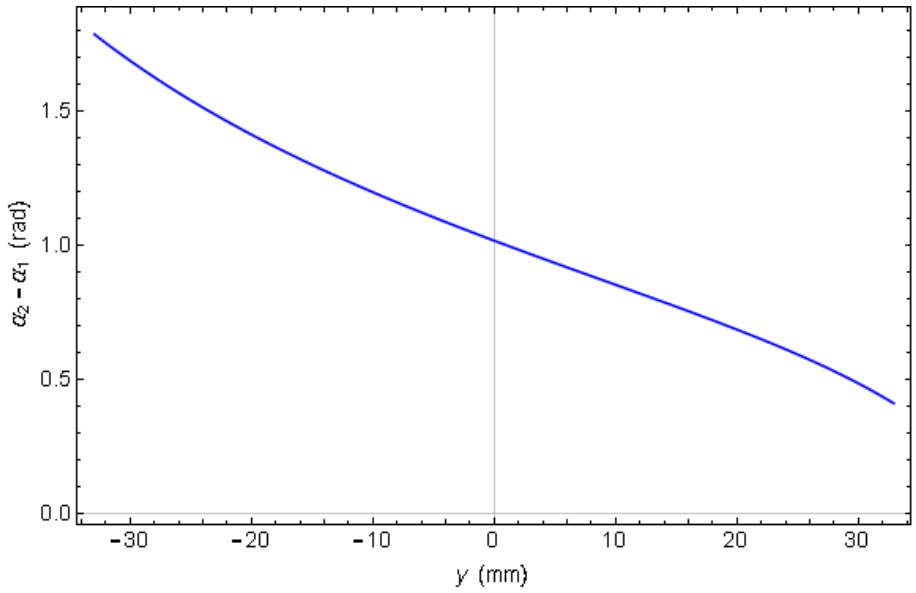

Figure 4.6: Dependence of $\alpha_2 - \alpha_1$ on y for any fixed value of x. The further up the beam lies the smaller gets the distance between the two peaks. This is a consequence of the arrangement of the two wires (cf. Fig. 4.3).

4.3.1 The electron beam

When the electron beam impinges on the wire, it induces a current signal. Since electrons are constantly reproduced at the cathode, this current is high enough to be measurable. As shown in Fig. 4.4 the rotating scanner is contacted the whole time with a balance spring. Via a feedthrough the signal is conducted out of the vacuum pipe, where is can be processed further. Hereby, it is assumed that the strength of the current signal is proportional to the geometrical overlap of the wire with the beam. In the following simulations of such signals are presented.

Inside the interaction region of the eCool the electron beam cross section can be very well approximated by a circular plane of radius R_e. This can be modelled by a number of equally distributed random points with coordinates (x, y), where $x^2 + y^2 \leq {R_e}^2$. For each point the corresponding rotation angles can be calculated with the functions found in Sec. 4.2. The group of all found angles α_1 are the angles, at which a signal is induced at the front wire; all angles α_2 belong accordingly to the back wire. This can be visualised by plotting all of these angles as a histogram. Thus, a qualitative model of the induced current signal can be shown.

The extent of the electron beam inside the interaction region can be calculated with the help of Eq. 3.27. With an expansion factor of $\alpha = 20$ the fully expanded beam has a radius of $R_e = 6.7\,\mathrm{mm}$. Figure 4.8 shows a histogram for a beam of this size around $(x_0, y_0) = (0\,\mathrm{mm}, 0\,\mathrm{mm})$, which corresponds to the centre of the beamline. The bin width has been chosen to be $18\,\mathrm{mrad}$, which equals the achievable experimental resolution.

The purpose of the wire scanners is to provide a tool that allows for the alignment of the electron and ion beam. The most important information that must be withdrawn from such a signal are, thus, the centre

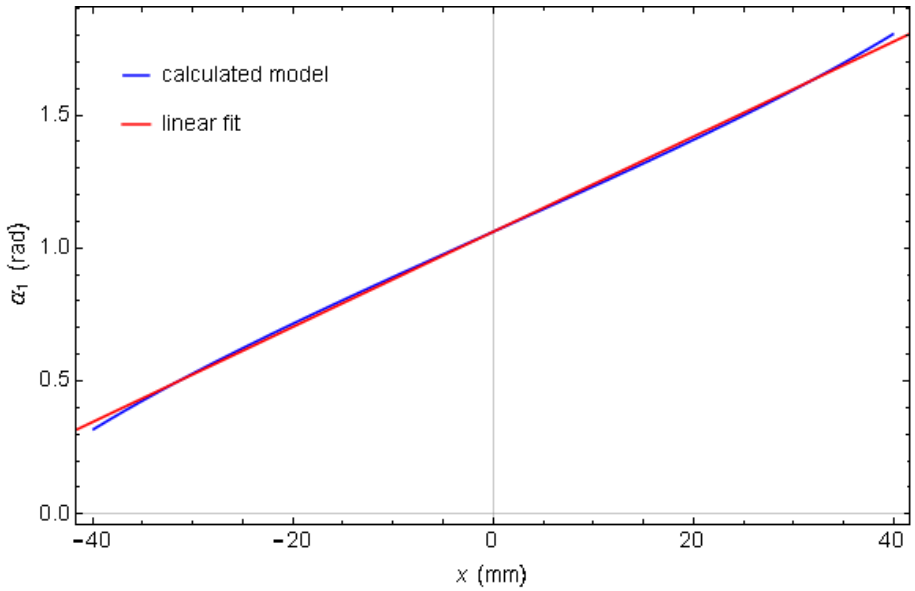

Figure 4.7: Dependence of α_1 on x at $y = 0$. Shown are the function withdrawn from the wire scanner model and a linear fit (see Eq. 4.7). With the aid of the latter the spatial resolution achievable with the scanner measurement can be estimated.

coordinates of the beam. For each of the peaks independently, i.e. for all angles measured with the front wire and for all angles measured with the back wire, the mean can be calculated. Let us call them $\overline{\alpha_1}$ and $\overline{\alpha_2}$. When applying the scheme developed in the last section to $\overline{\alpha_1}$ and $\overline{\alpha_2}$, the beam centre coordinates x_0 and y_0 can be regained. Secondly, the beam diameter can be determined from the width of the peak[1]. The angular width of the blue peak in Fig 4.8 is $0.255\,\mathrm{rad}$. Using Eq. 4.7 this results in a spatial width of $14(1)\,\mathrm{mm}$. The original beam diameter of $13.4\,\mathrm{mm}$ lies within the error. The same result is obtained from the width of the green peak, which is as well $0.255\,\mathrm{rad}$.

In order to investigate the effects of a shifted beam centre on the expected current signal, the above procedure has been conducted for four other beam profiles not lying in the centre of the beamline. Figures 4.9 and 4.10 display angle distributions of beams shifted right, left, up and down by $5\,\mathrm{mm}$ respectively from the same. For better comparison the histogram of the non-shifted beam is drawn into each plot as well. In Table 4.2 the means for α_1 and α_2 and their differences are noted for each of these figures.

As expected from the mathematical model, a solely horizontal shift does not change the distance between the peaks. Only $\overline{\alpha_1}$ becomes smaller (larger) for a left (right) shifted beam. If the beam is shifted vertically, $\overline{\alpha_2} - \overline{\alpha_1}$ changes. It is the smaller the further up the beam lies. All in all, the procedure developed for two single angles can be simply transferred to the means of two measured angular distributions.

[1] This is only true if the beam cross section can be represented by a circle.

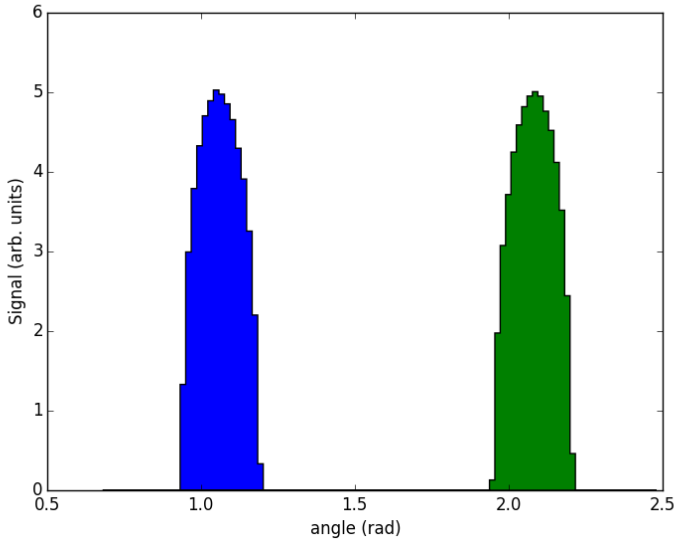

Figure 4.8: Model of the induced current signal obtained from geometrically overlapping the wire scanner vector with the beam cross section. The beam profile consists of $\sim$ 162000 equally distributed points in a circular plane with $R_e = 6.7\,\mathrm{mm}$ and centre coordinates $(x_0, y_0) = (0\,\mathrm{mm}, 0\,\mathrm{mm})$. The blue (green) peak is a histogram of all angles α_1 (α_2) corresponding to points of the beam profile. The bin width is $18\,\mathrm{mrad}$. Since the shape of the signal can only be modelled qualitatively, the area is normalised to 1.

4.3.2 The ion beam

While performing measurements ions are not constantly injected into the ring. That means that, in contrast to the electrons, ions are not reproduced. As mentioned before this leads to the fact that the ion beam current is not high enough for it to be measured in the same way as the electron current. On the other hand, one can take advantage of this, and detect the decrease in ion current when an object, a so-called scraper, is slowly moved across the beamline. Fig. 4.11 illustrates such a scraper measurement for simplicity in one spatial dimension only. Firstly, any ion that hits the scraper directly is lost. Secondly, the scraper restrains the available phase space. Due to the betatron oscillations, one particle is located on a different point of the phase space ellipse after every turn in the storage ring (indicated by the green dots in the figure). From this follows that all particles residing on an ellipse overlapping with the scraper are lost. One consequence from this is that the ion beam vanishes completely as soon as the scraper reaches the closed orbit of the central particle [21]. This can be exploited to determine the centre coordinates of the ion beam.

The rotating wires are thick enough to be also employed as scrapers. In practice a scraper measurement could look like described in the following. First, ions are injected and stored in the ring. The initial position of the scraper is on the left-hand side of the beamline as it is depicted in Fig. 4.1. It is then turned counter-clockwise into the beam. In this case the front wire (described by $\overrightarrow{sc1}(\varphi)$) reaches the ions first and, thus, stops them. Hence, the relevant angle for this measurement is α_1. The number of stored ions needs to be detected as a function of the same. When the wire reaches the closed orbit, the signal drops to zero; no ions are present in the ring at this point. The scraper is then moved to the right-hand side of the beamline before

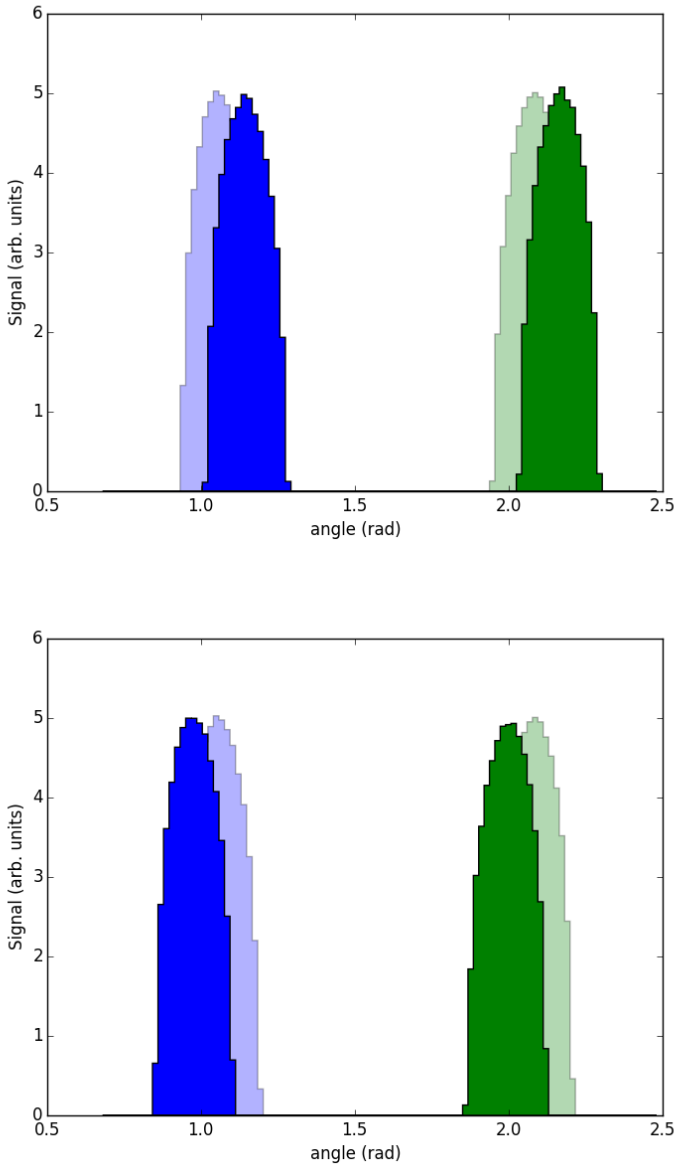

Figure 4.9: Effects of a horizontally shifted beam on the modelled angular distribution. The upper (lower) panel shows a model of the induced current signal for a beam shifted right (left) by $5\,\mathrm{mm}$ relative to the beamline centre. The beam profiles consist each of $\sim$ 16200 equally distributed points in a circular plane with $R_e = 6.7\,\mathrm{mm}$ The blue (green) peak is a histogram of all angles α_1 (α_2) corresponding to points of the beam profile. The pale peaks correspond to a centred beam. The bin width is $18\,\mathrm{mrad}$, and all areas are normalised to 1.

the next injection. In the second measurement phase the scraper is rotated clockwise so that the back wire ($\overrightarrow{sc2}(\varphi)$) cuts away the beam. Now, the number of ions is determined as a function of α_2.

The intensity of the stored ion beam can for example be measured with the current pick-up installed in the CSR's diagnostics section. In this case the beam first has to be bunched by means of the rf-system.

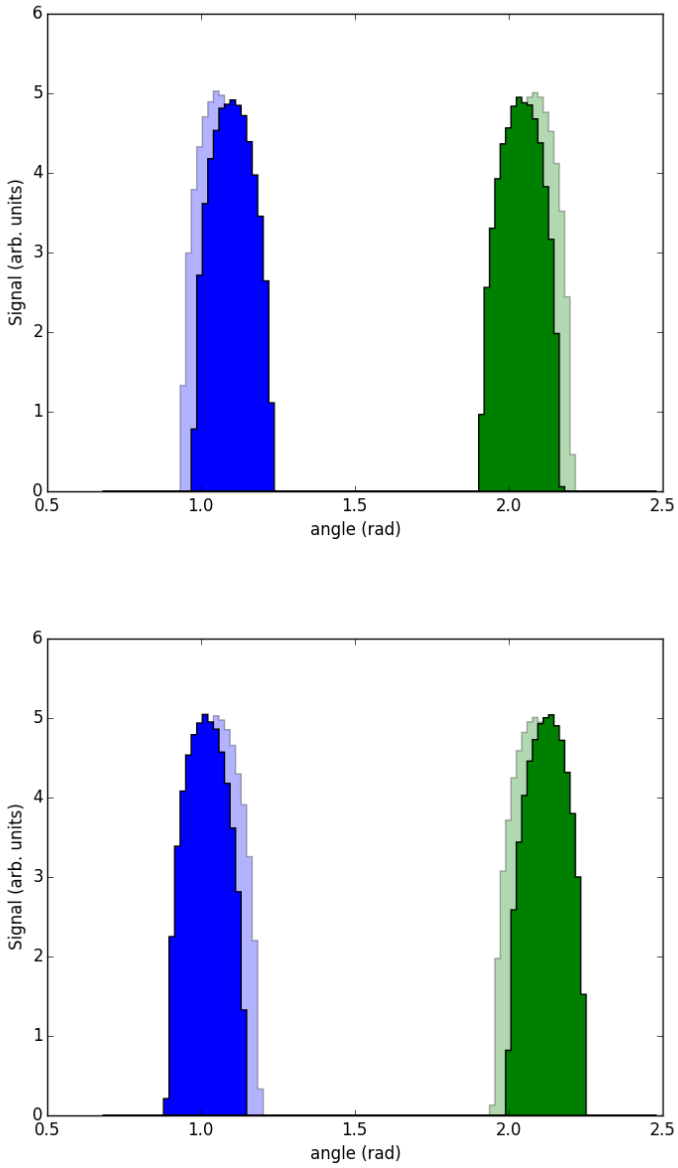

Figure 4.10: Effects of a vertically shifted beam on the modelled angular distribution. The upper (lower) panel shows a model of the induced current signal for a beam shifted upwards (downwards) by $5\,\mathrm{mm}$ relative to the beamline centre. The beam profiles consist each of $\sim$ 162000 equally distributed points in a circular plane with $R_e = 6.7\,\mathrm{mm}$ The blue (green) peak is a histogram of all angles α_1 (α_2) corresponding to points of the beam profile. The pale peaks correspond to a centred beam. The bin width is $18\,\mathrm{mrad}$, and all areas are normalised to 1.

Then, the Fourier spectrum of the ion current is acquired. The ion intensity is, thereby, proportional to the amplitude of the first spectral line, whose position in frequency domain corresponds to the rf. The height of the amplitude can be followed over time. If the rotation angle of the scraper can be assigned to each point in time, then the number of ions as a function of said angle will be obtained. One has to adhere to this

Beam position	$\overline{\alpha_1}$ rad	$\overline{\alpha_2}$ rad	$\overline{\alpha_2} - \overline{\alpha_1}$ rad
centred	1.061	2.080	1.019
right shifted	1.146	2.166	1.019
left shifted	0.976	1.995	1.019
up shifted	1.103	2.039	0.935
down shifted	1.017	2.124	1.107

Table 4.2: Effect of relocation of the electron beam from the central orbit on the angular distribution. Given are the means of α_1, α_2 and their respective differences for the simulations shown in figures 4.8 to 4.10. The error on the angles is $0.018\,\mathrm{rad}$ respectively.

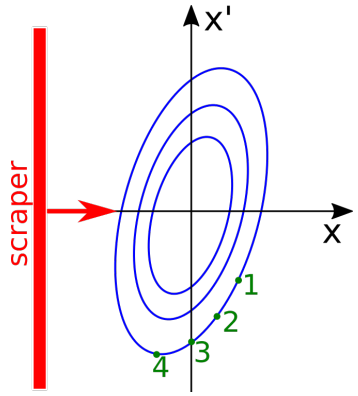

Figure 4.11: Principle of a scraper measurement. Within the storage ring the particles reside on phase space ellipses (coloured in blue). One particle is located on a different point on the phase ellipse after every turn in the storage ring, for example at position 1 after the first turn, at position 2 after the second turn and so on. Due to these betatron oscillations, all ellipses overlapped by the scraper are forbidden. As the scraper is moved further into the beam, more and more particles are lost and the beam intensity decreases. When the scraper reaches the origin, the intensity signal vanishes completely, which can be used to determine the beam centre. Note that in contrast to the figure, our scrapers constrain the four dimensional phase space described by x, x', y and y'.

procedure for both measurement steps. This results in two curves (one for each direction of rotation). Like the electron beam signal they have been modelled qualitatively, which is presented in the following.

At first, the distribution of ions in phase space has to be developed. Since the scraper only has the purpose to measure the transverse cross section, we limit the phase space to four dimensions given by x, x', y and y'. The density distribution is assumed to be Gaussian. We presume that the beam is initially matched to the acceptance of the ring as given in Eq. 3.12. Then, the 4D phase space ellipsoid at the position of the scraper can be represented by

$$\sigma = \frac{1}{9}\begin{pmatrix} \beta_x A_x & -\alpha_x A_x & 0 & 0 \\ -\alpha_x A_x & \gamma_x A_x & 0 & 0 \\ 0 & 0 & \beta_y A_y & -\alpha_y A_y \\ 0 & 0 & -\alpha_y A_y & \gamma_y A_y \end{pmatrix}, \tag{4.8}$$

	Horizontal	Vertical
β	$9.25\,\mathrm{mm\,mrad^{-1}}$	$2.5\,\mathrm{mm\,mrad^{-1}}$
α @ first scanner	0	0.5
α @ second scanner	0	-0.5
γ	$0.108\,11\,\mathrm{mrad\,mm^{-1}}$	$0.5\,\mathrm{mrad\,mm^{-1}}$

Table 4.3: The optical functions at the positions of the wire scanners. β and γ are symmetric around the centre of the drift section and, thus, identical for both scanners. The values for β and α are read off from Fig. 3.1 and 3.2. γ can be calculated from this with the help of Eq. 3.11.

with the values of the optical functions given in Tab. 4.3. The equation is multiplied with $1/9$, because the acceptance is set equal to the 3σ-emittance. Considering that the ion number can only be measured with a precision of around $10\,\%$, this is a valid approximation. Each beam profile is simulated with $100\,000$ random points distributed across the phase space as described above.

The scraper is represented by the group of all points corresponding to an angle α_1 (or α_2 for the second measurement phase) according to the model developed in the course of this work. For each angle setting the maximum ellipse in the $x-y$ plane, that is still not overlapped by the scraper is found. It is, thereby, assumed that the ratio of the axes stays constant. Since the optical functions do not change their values, it is possible to calculate from this the full 4D phase space still available. Only points lying on phase space ellipses still allowed, then, contribute to the ion intensity.

The optical function α is a measure for the inclination of the phase space ellipse. A value of 0, how it is achieved in the centre of the drift region, corresponds to an upright standing ellipse. The sign of α only indicates in which direction the phase space ellipse is tilted. However, due to the betatron oscillations the scraper restrains the absolute values of x, y, x' and y'. Therefore, the measured signal should ideally be identical at both wire scanners. Deviations from this could indicate that the beam is not running parallel to the central orbit.

Fig. 4.12 visualises the modelled signal as a function of the rotation angle. The blue curve corresponds to the signal obtained from turning the scraper counter-clockwise starting at zero (α_1). The green curve actually begins at the right-hand side of the image, and it belongs accordingly to the clockwise rotation of the scraper (α_2). An ion beam centred at $(x_0, y_0) = (0\,\mathrm{mm}, 0\,\mathrm{mm})$ forms the basis of this specific figure. As described above this information should be regained by evaluating the angles, where the signal drops to zero. The combination of $\alpha_1 = 1.062\,\mathrm{rad}$ and $\alpha_2 = 2.080\,\mathrm{rad}$ does indeed lead to the expected point. The CSR only features horizontal deflecting elements but no vertical ones. The appearance of a horizontally shifted ion beam is, therefore, also much more likely. Fig. 4.13 shows the modelled ion intensity for two beams, one shifted right and one left by $5\,\mathrm{mm}$ respectively. Again, the centre of the beam can be determined from the angles, where the respective signal vanishes.

Identifying the ion beam shape from the measured signal is not as easy, however. An indication of the beam size is given by the width of the curve. As an example, the modelled ion intensity for a smaller centred beam is plotted in Fig. 4.14. All values are the same as above except for the initial emittances, which are $\epsilon_{x,i}^{3\sigma} = 0.5 \cdot A_x$ and $\epsilon_{y,i}^{3\sigma} = 0.5 \cdot A_y$. The modelled signals drop to zero at the same angles as in Fig.

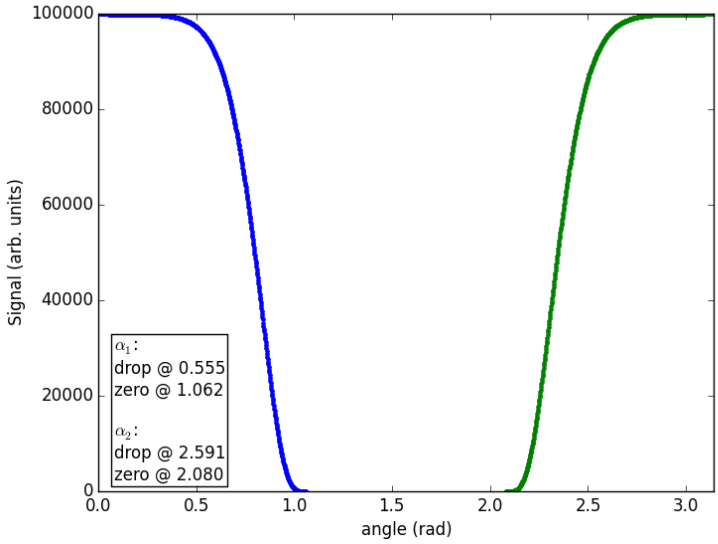

Figure 4.12: Modelled ion intensity as a function of the scraper rotation for an ion beam centred at $(x_0, y_0) = (0\,\mathrm{mm}, 0\,\mathrm{mm})$. The blue (green) curve corresponds to the counter-clockwise (clockwise) rotation of the scanner. Starting points are respectively the left-hand side ($0°$) and the right-hand side ($180°$) of the beamline. The beam centre can be determined from the angles, where the signal drops to zero. The angles indicated by "drop" in the box indicate, where the intensity first falls below $95\,\%$ of the initial one.

4.12, which is only natural because the beam centres are the same. For each signal the angle where the intensity first drops below $95\,\%$ of the initial one is determined (labelled by "drop" in the text boxes). When comparing figures 4.12 and 4.14 one notices that for the smaller beam this angle lies much closer to the angle at which the signal disappears. This way, it can be illustrated that the curve is indeed much narrower.

4.4 Discussion

In the course of this work the design of the wire scanners has been finalised. Thereby, several constraints have been addressed. The main purpose of the scanners is to monitor the alignment of the ion beam with the electron beam inside the interaction region of the electron cooler. Therefore, they are installed at both ends of this section at a position where the two beam are ideally already completely overlapped. The presence of two scanners makes it possible to check for unwanted angular deviations.

The scanner drive is realised in the form of a worm drive with a transmission ratio of 360. A rotation of the scanner by $1°$, thus, corresponds to one full rotation of the outside drive shaft. This makes it fairly simple to regulate and read the current angle. Almost perfect thermal decoupling is achieved by inserting an intermediate drive, which can be positioned such that none of its ends makes thermal contact.

The scanners are of a dual-wire design. In principle, this allows for the determination of the complete transverse position of the beam with one scan only. However, it is necessary that particles are detected at

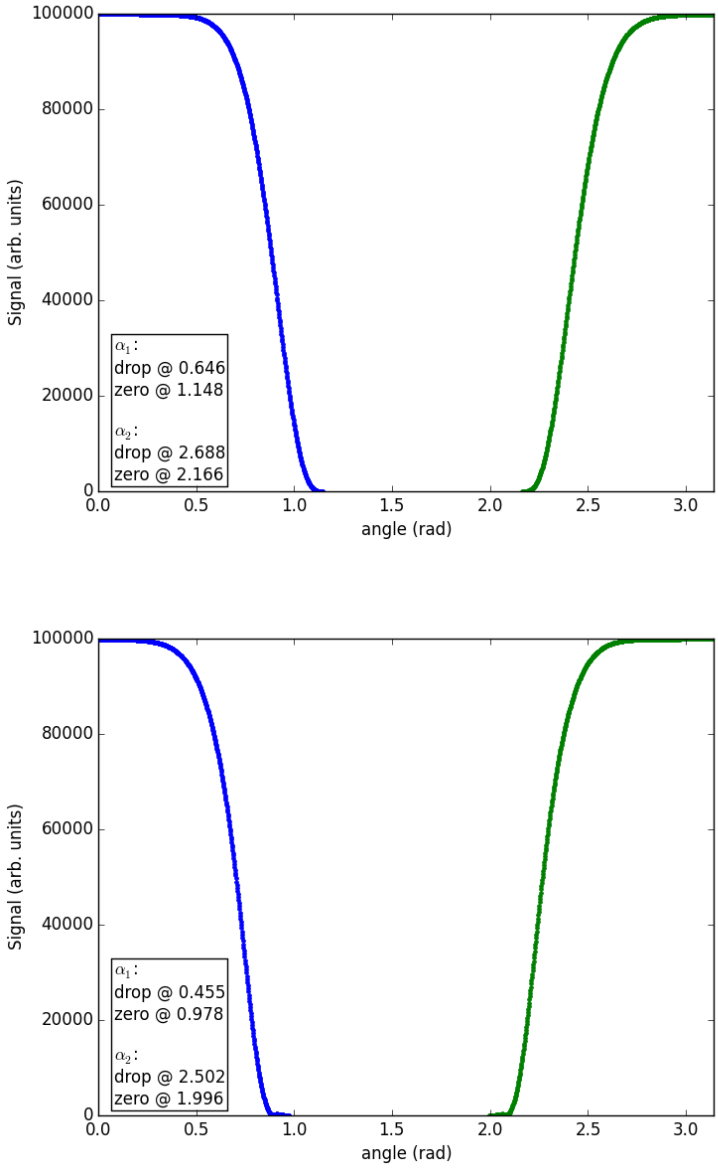

Figure 4.13: Effect of a horizontally shifted beam on the modelled ion intensity. The upper (lower) panel shows the signal for a beam shifted right (left) by $5\,\mathrm{mm}$ with respect to the beamline centre. The blue (green) curve corresponds to the counter-clockwise (clockwise) rotation of the scraper. Starting points are respectively the left-hand side (0°) and the right-hand side (180°) of the beamline. The beam centre can be determined from the angles, where the signal drops to zero. The angles indicated by "drop" in the box indicate, where the intensity first falls below $95\,\%$ of the initial one.

both wires, which corresponds to two signals at two different rotations angles. A scheme has been developed to calculate the spatial transverse coordinates from these two angles. An angular resolution of 1° given, a spatial resolution of $1\,\mathrm{mm}$ can be achieved.

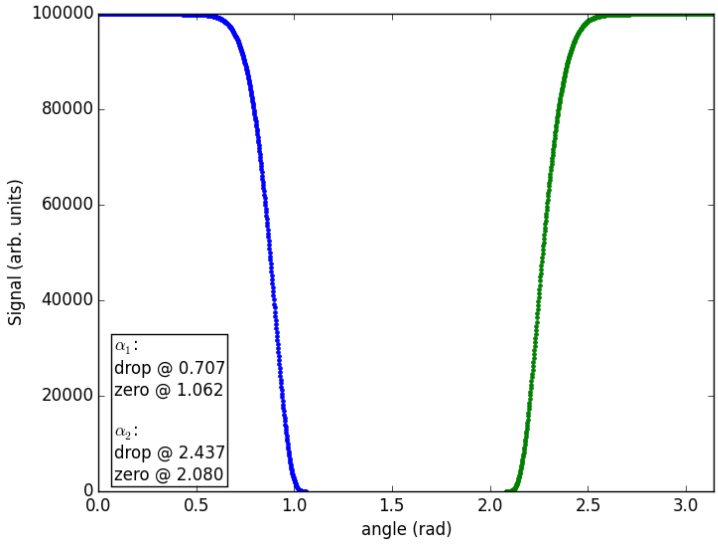

Figure 4.14: Modelled ion intensity as a function of the scraper rotation for a centred beam with smaller initial cross section. All values are the same as for the beam plotted in Fig. 4.12, except for the initial emittances, which are $\epsilon_{x,i} = 0.5 \cdot A_x$ and $\epsilon_{y,i} = 0.5 \cdot A_y$. Note that the signal vanishes at the same scraper position because the beam centres are the same. The "drop angles", where the intensity first falls below $95\,\%$ of the initial one, have changed though, and the width of the curve has decreased.

A simulation of the current signal which is generated when the wire scanner transverses the electron beam has been conducted. The centre of the beam can be very well determined by applying the developed scheme to the means of the obtained angular distributions. From the width of the same the beam diameter can be found. The real wire, however, is not just a line but has a radius of $1\,\mathrm{mm}$. Therefore, the experimental signal might be widened compared to the simulation. Since the size of the radius equals the spatial resolution, I do not expect this to be a significant effect.

Since ions are not constantly reproduced, we assume that the signal generated at the wires will not be measurable. Still, the wire has been chosen thick enough that it can be used as a scraper limiting the available phase space when it is moved into the beam. Ions are lost when they hit the scraper, therefore, two ion injections and two rotations in opposite directions are necessary to make the computation of the beam position possible. It could be shown that the centre of the beam can be calculated from the angles where the respective signals vanish. Thereby, the spatial resolution does not only depend on the angular resolution of the scanners but also on the precision with which the number of stored ions can be measured. A technique to avoid this problem would be to take two measurements per wire and calculate the mean from the two obtained angles. This is sketched in Fig. 4.15. The two exterior curves are gained in the same manner as above. In order to acquire the interior curves, the starting position of the scraper is in both cases at $90°$ so that the beam lies between the wires. Then, the scanner is rotated clockwise (counter-clockwise) to obtain the second α_1 (α_2) value. The horizontal line drawn into the figure indicates the lower detection limit of the ion intensity. The angles where the curves intersect with this line are the ones that would be falsely identified as the "closed-orbit-angles" in an experiment. Taking the mean of the two angles, however, leads

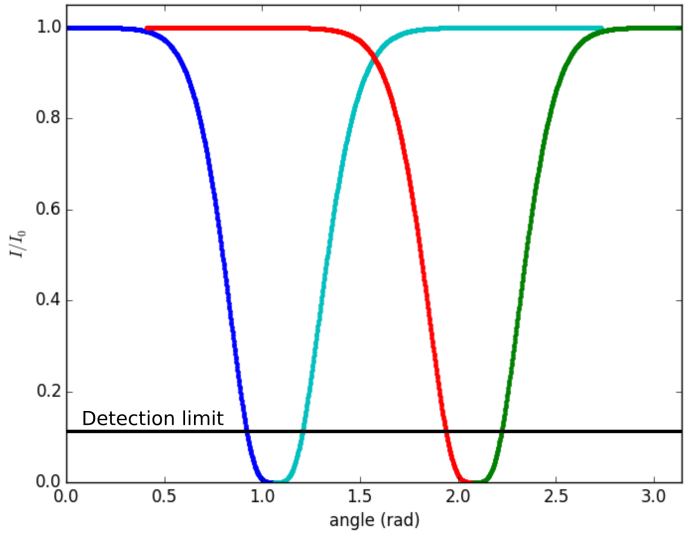

Figure 4.15: Method to determine the ion beam location even if the detection limit forbids to directly detect the angle where the signal vanishes. The two left (right) curves correspond to a signal measured with the wire described by $\overrightarrow{sc1}(\varphi)$ $\left(\overrightarrow{sc2}(\varphi)\right)$. The exterior curves are obtained as depicted in Fig. 4.12. For measuring the interior curves, the scraper initially needs to be placed at a 90° angle and turned clockwise (counter-clockwise) for the turquoise (red) curve. Four ion injections are needed if this technique should be applied. Since the initial ion intensity is not necessarily the same for every injection, the decline of the relative ion intensity I/I_0 has to be analysed. From the two angles, where the left curves intersect the detection limit, the mean can be calculated. Doing the same for the right curves yields the values of α_1 and α_2 that are necessary to compute the ion beam centre. The exact value of the detection limit in the image is chosen arbitrarily.

to the true zero-point of the ion intensity. From the means of α_1 and α_2 the beam centre can then be computed. Since it cannot be assumed that the initial ion intensity is constant with every injection, it is essential to analyse only the decrease of the relative signal I/I_0 when applying this method.

The ion beam density is assumed to be Gaussian, and the transverse beam profile is elliptical. The scraper does not cut parallel to one of the main axes. In addition, the intersecting line varies with the initial beam position. This given, it is not easily possible to deduce the transverse beam size from the measured signal. A qualitative hint, however, is given by the width of the curve.

Chapter 5

Development of an electron collector for the CSR electron cooler

The new CSR electron cooler, which has been described in Chapter 3, consists basically of three sections arranged in a U-shape. At first, an electron beam is produced in the cathode section. The second section, where the interaction between the electrons and the stored ion beam takes place, is integrated into the CSR. The third section will now be the setting of the following chapter.

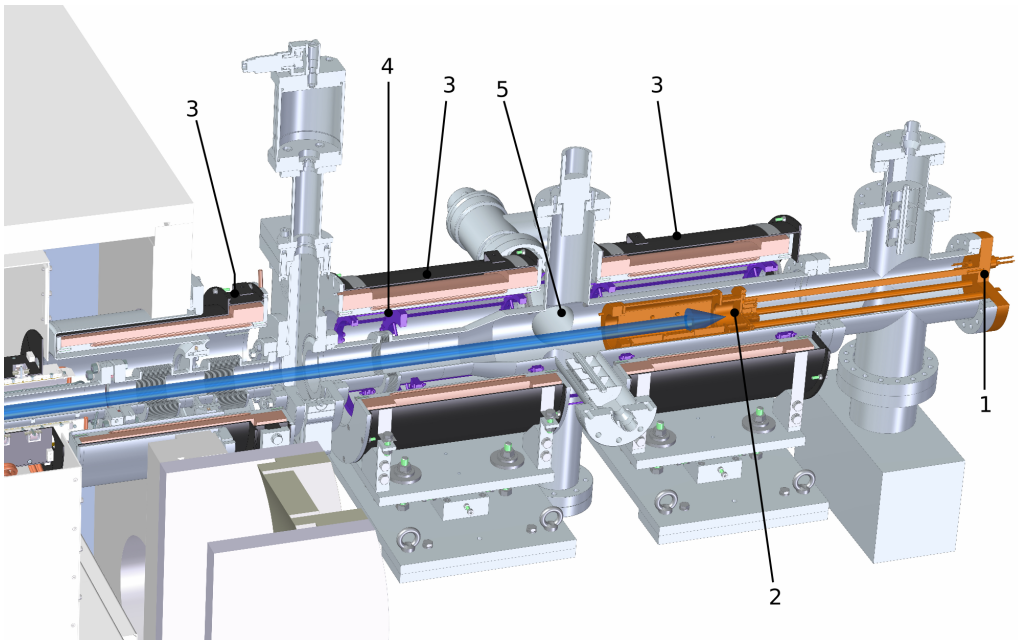

Figure 5.1: Layout of the collector section of the eCool showing: 1 – CF 100 flange, 2 – collector, 3 – solenoids, 4 – rack for steerer and Wien filter coils, 5 – CF 63 cross chamber. The blue arrow depicts the movement of the electron beam. Image courtesy of S. Vogel.

After merging with the stored ions, the electron beam is deflected from the ring and enters the collector section. The model depicted in Fig. 5.1 gives an overview of the latter. Within this segment three things need to happen: 1) the electrons have to be collected to close the current circuit between the cathode and the collector, 2) properties of the electron beam have to be determined and monitored during an experiment and 3) secondary emission from surfaces exposed to the beam needs to be controlled. All of these functions are fulfilled by the collector (2 in Fig. 5.1). It can be divided into three groups with each one addressing one of the issues stated above. The foremost group (as seen by the electrons) consists of an assembly of electrodes for suppression of secondary emission. For gathering the electrons a Faraday cup is used, which from here on will be called the *main cup*. It is followed by a second cup, the so-called *analyser cup*, which can be employed for measurements.

In this chapter the development of the electron collector for the CSR eCool will be described. In addition to the three necessities stated above, more specific requirements on the apparatus are reported in section 5.1. Section 5.2 then depicts in detail the design of the collector.

5.1 Requirements on design

5.1.1 Spatial constraints

When this work was begun, the collector section of the eCool including the vacuum system and all magnets had already been designed, manufactured and built up. Thus, it is essential for the new collector that it is tailored to this set-up. All equipment must fit into the vacuum pipe, which has an inner diameter of $100\,\mathrm{mm}$. In order to keep the CF 63 cross chamber (5 in Fig. 5.1) free for future experimental equipment, the collector should not extend into it.

Fig. 5.2 shows the longitudinal magnetic field B_0 over the length of the collector section in the centre of the beamline. As explained in Sec. 3.3, it is the purpose of this field to guide the electrons from the cathode to the collector. Towards the end of the eCool, however, the longitudinal magnetic field drops to zero (this corresponds to the first $\sim 36\,\mathrm{cm}$ in Fig. 5.2). This large magnetic field gradient leads to magnetic expansion of the electron beam (cf. Sec. 3.3.2), which can distort measurements conducted with the analyser cup. Therefore, the latter should be placed in a region with a relatively constant magnetic field, i.e. behind $z = 36\,\mathrm{cm}$. With these constraints in place, a total length of $26\,\mathrm{cm}$ (between $z = 36\,\mathrm{cm}$ and $z = 62\,\mathrm{cm}$, where the CF 63 cross starts) is available for the actual collector (without mounting parts).

5.1.2 Operation in an UHV environment

The collector section of the eCool needs to be kept at a vacuum level in the low $10^{-11}\,\mathrm{mbar}$ region. In order to achieve this, the vacuum pipe and the collector contained therein need to be baked out to temperatures of up to $250\,^{\circ}\mathrm{C}$. Thus, all materials used for the collector must withstand these temperatures. In addition, the set-up will experience thermal expansion and shrinkage between the operating room temperature and the

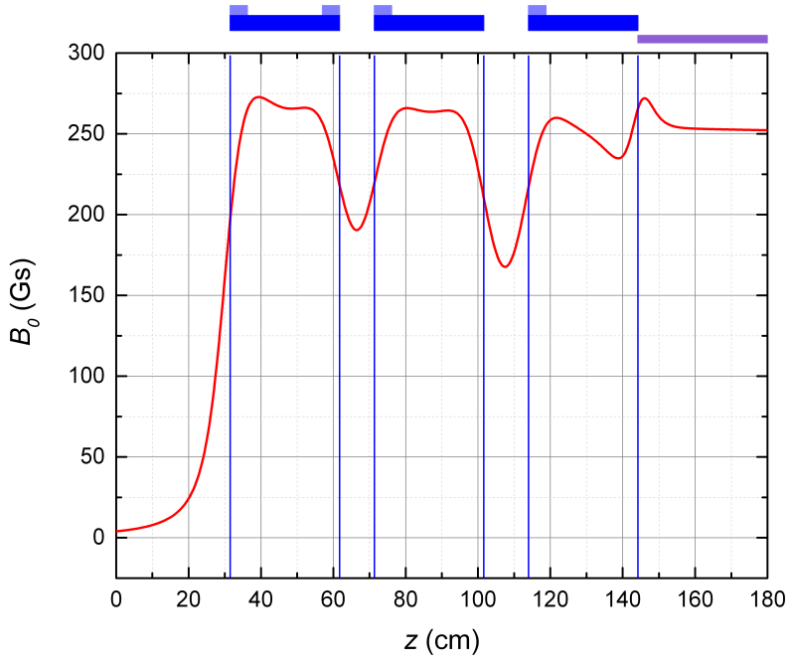

Figure 5.2: Shown is a simulation of the longitudinal magnetic field B_0 over the length of the collector section in the centre of the beamline, i.e. $x = y = 0$. $z = 0$ corresponds to the inner surface of the closing flange. The blue rectangles and the vertical blue lines mark the positions of the solenoids. The light blue rectangles indicate where additional coils have been added. The current flowing through each of the three solenoids is 13.19 A. The purple rectangle depicts the beginning of the merging toroid. Finite-element simulation done by S. Vogel [70].

bake-out temperature. It needs to be ensured that, due to this, the collector electrodes do not change their relative position by a significant extent.

The CSR and its electron cooler are designed for very low energies. Therefore, the cup is only exposed to a relatively low electric power. The maximum electron current produced by the cathode is $1\,\mathrm{mA}$, and the maximum potential difference between the cathode and the collector is $1\,\mathrm{kV}$, resulting in a maximum power of $1\,\mathrm{W}$. This power, with which the electrons impinge on the collector cup, is much smaller than in other electron coolers (compare for example to the TSR electron target where $P_{max} = 595\,\mathrm{W}$ [64]). However, the collector is still located in UHV, which implies that all power which is converted to heat at the cup has to be dissipated by thermal conductance alone. In order to determine if the thermal conductivity of the collector's material is sufficient or if additional water cooling is needed, an experiment on a test collector set-up has been conducted.

5.1.2.1 Test of thermal conductivity: Set-up

A photograph of the installation is shown in Fig. 5.3. Three $250\,\mathrm{mm}$ long aluminium rods with a diameter of $10\,\mathrm{mm}$ connect the CF flange with a supporting ring made from stainless steel (1.4435). The actual cup is simulated by a stainless steel plate, which is screwed to the top of the ring. Both the ring and the plate have a diameter of $31\,\mathrm{mm}$ and a thickness of $3\,\mathrm{mm}$. The cup needs to be electrically isolated from the

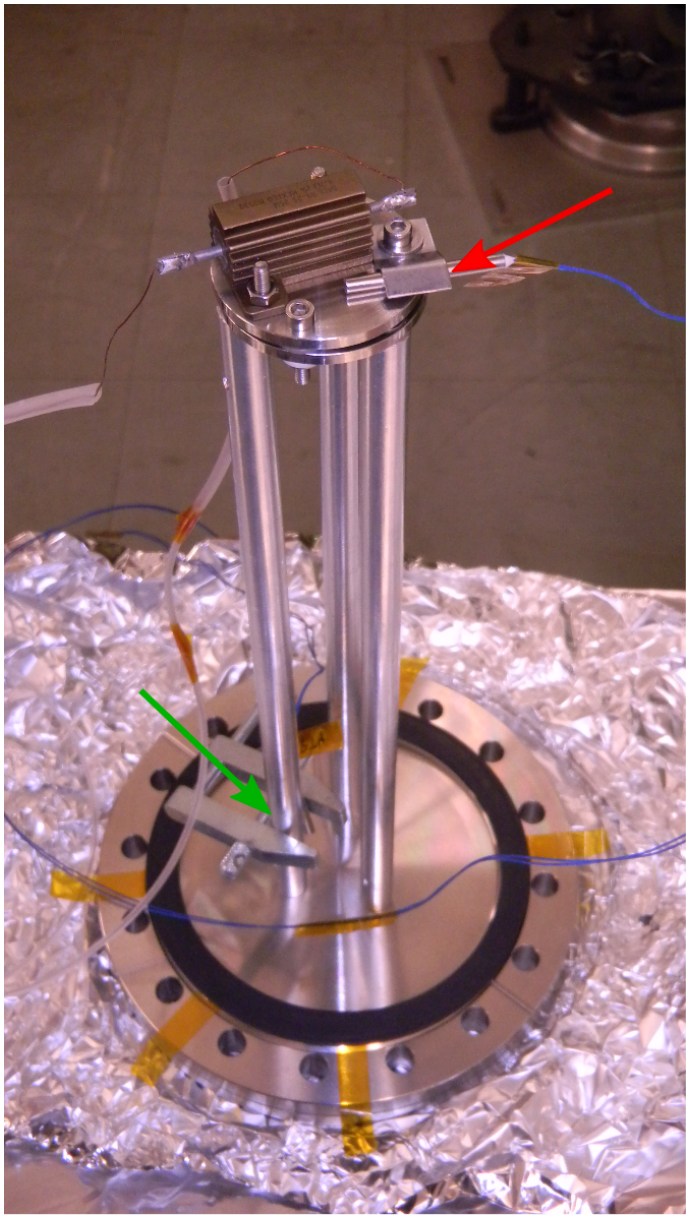

Figure 5.3: Photograph of the set-up for the experimental testing of heat conductance. The red (green) arrow indicates the location of the temperature sensor PT1 (PT4). See text for further explanations of the different parts.

retaining structure, but good thermal conductivity needs to be ensured. Therefore, three sapphire washers of $1\,\mathrm{mm}$ thickness are inserted between plate and ring.

In order to simulate the power transferred by the electrons, a resistor ($R = 5.4\,\Omega$) is mounted on top of the plate. The temperature is monitored as a function of the applied power with the help of two PT1000 sensors. One of the them (labelled PT1) is placed directly next to the resistor; the other one (PT4) is attached to one of the aluminium rods close to the flange (see Fig. 5.3). This way, the temperature difference across the full length of the set-up can be observed.

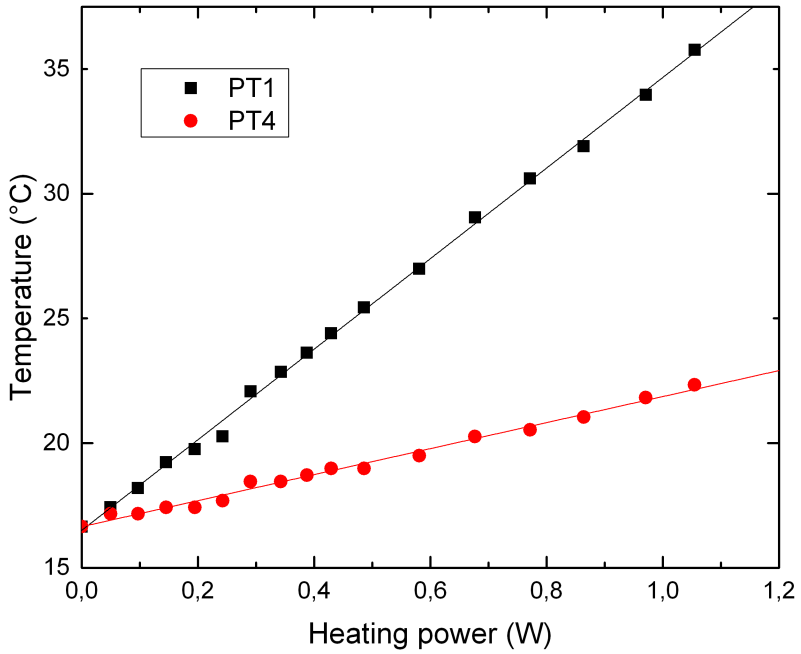

Figure 5.4: Temperatures at the test collector set-up as a function of the power applied to the resistor. The black squares show the temperature measured with PT1 next to the resistor. The red dots are detected with PT4 at the bottom of one of the aluminium rods. The lines are the corresponding linear fits.

In order to simulate the conditions inside the electron cooler, the experiment is performed inside a vacuum chamber. The pressure in the beginning of the measurements was $5.5 \times 10^{-7}\,\mathrm{mbar}$. While this is a much higher residual gas pressure compared to the $10^{-11}\,\mathrm{mbar}$ targeted for the eCool set-up, the quality of the vacuum is more than sufficient to prevent convective heat transport. Hence, it is an adequate environment for the heat balance experiment. The pressure has been monitored during the whole data taking time, but it only slightly increased to $8.3 \times 10^{-7}\,\mathrm{mbar}$. This rise can be explained by the fact that the components have not been degassed by high temperature bake-out before the experiment.

5.1.2.2 Test of thermal conductivity: Results

In Fig. 5.4 the temperatures from both sensors are plotted as a function of the power applied to the resistor. The measured resistances have been converted to the corresponding temperatures with the data from [54].

The maximum temperature difference, which is reached at an applied power of $1.055\,\mathrm{W}$, is $13.4\,^{\circ}\mathrm{C}$. Higher heating powers have not been probed. Both temperature curves can be very well approximated by a linear fit:

$$T_{PT1}(P) = 18.16(18)\,\frac{^{\circ}\mathrm{C}}{\mathrm{W}} \cdot P + 16.50(10)\,^{\circ}\mathrm{C}, \tag{5.1}$$

$$T_{PT4}(P) = 5.22(13)\,\frac{^{\circ}\mathrm{C}}{\mathrm{W}} \cdot P + 16.65(07)\,^{\circ}\mathrm{C}. \tag{5.2}$$

Inside a solid state body the temperature T at a position x depends linearly on the rate of heat flow $\dot{Q}$:

$$T(x) = -\frac{x}{\lambda A} \cdot \dot{Q} + T(0), \tag{5.3}$$

with the thermal conductivity λ and the body's transverse section A. The linear behaviour of the measured temperature difference with the applied heating power, thus, strongly indicates that we have really measured heat conductance inside the material of the set-up. Given that, it can be concluded that the maximum temperature difference is tolerable and that no additional water cooling is needed.

5.1.3 Minimisation of electron backstreaming

When the electrons reach the collector, they hit the metal surface of the main cup and produce secondary electrons. They can also be reflected. These secondary and reflected electrons have a finite probability to leave the collector region and drift back towards the photocathode. When they impinge in vicinity of the latter, they cause local vacuum degradation, which must be avoided at all cost because it quickly destroys the (Cs,O) layer on the photocathode's surface (cf. Sec. 3.3.3).

One way of decreasing the secondaries' chance to escape the collector region is to install a so-called *repeller electrode* in front of the main cup. The repeller is electrically isolated from the main cup and can, therefore, be set to a negative potential with respect to the latter. This is sketched in Fig. 5.5. Secondary or scattered electrons experience this as a potential barrier, which they can only overcome if their kinetic energy is high enough. The maximum allowed potential is determined by the fact that the primary electron beam must not be stopped by the repeller. Reflected electrons, which carry the same or a large fraction of the initial kinetic energy can, hence, not be blocked by such an arrangement.

A different solution has been suggested by Bryzgunov et al. for the electron cooler of the COSY (**co**oler **sy**nchrotron) accelerator in Jülich, Germany [7]. They use a *Wien filter* to suppress back streaming electrons, which have been reflected at the collector. The basic working principle of a Wien filter is demonstrated in Fig. 5.6.

A Wien filter consists of crossed electric $\vec{E}$ and magnetic fields $\vec{B}$, which are again perpendicular to the direction of movement of the incoming electron beam. For an electron of velocity

$$v = \frac{|\vec{E}|}{|\vec{B}|} = \frac{E}{B} \tag{5.4}$$

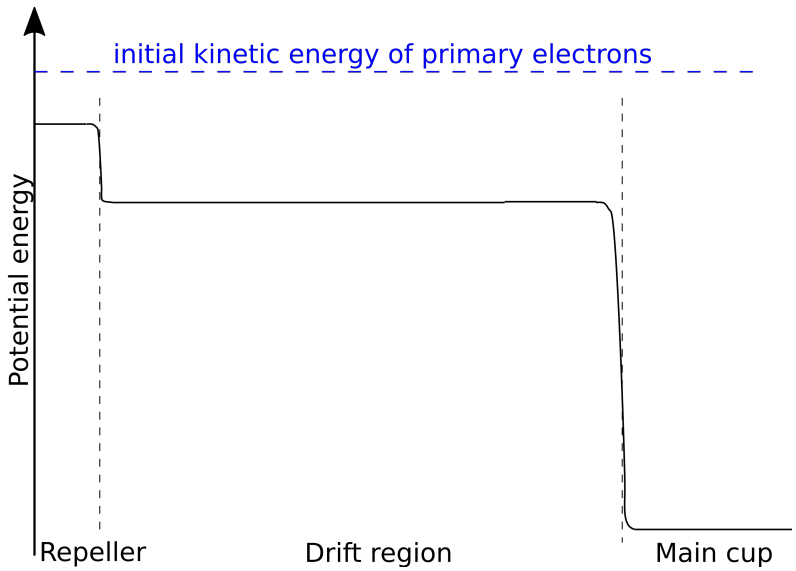

Figure 5.5: Sketch of the potentials in the collector including the repeller and the main cup. Also shown is the initial kinetic energy of the incident electron beam (blue dashed line). The axes are not to scale.

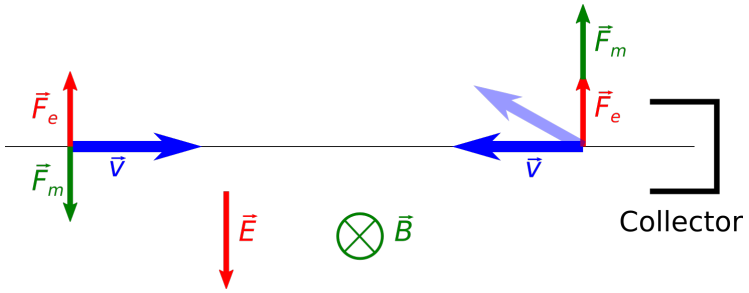

Figure 5.6: Working principle of a Wien filter consisting of crossed electric $\vec{E}$ and magnetic fields $\vec{B}$. The primary electron beam (blue arrow pointing right) of velocity $\vec{v}$ moves undeflected towards the collector because the electric and magnetic forces ($\vec{F_e}$ and $\vec{F_m}$) compensate for each other. A beam of reflected electrons (blue arrow pointing left), on the other hand, is deflected (light blue arrow).

the electric and the magnetic parts of the Lorentz force (Eq. 2.1) compensate for each other so that the particle moves undeflected through the Wien filter. A reflected electron moving in the opposite direction experiences a net force $\vec{F}_\perp$, which deflects it from its original path. It can, thus, be steered towards a *secondary collector* installed at a suitable position. If the absolute value of the electron's velocity is given by Eq. 5.4, then the strength of this net force can be determined by rewriting Eq. 2.1:

$$\begin{aligned} |\vec{F}_\perp| &= |\vec{F}_e| + |\vec{F}_m| \\ &= eE + evB \\ &= 2eE \\ &= 2evB. \end{aligned} \tag{5.5}$$

This is not the full picture, however. Inside the collector section a second, stronger magnetic field is present: the longitudinal magnetic guiding field $\vec{B}_0$, which is perpendicular to both of the Wien filter fields. Let us first consider the electron's movement in this field alone. The movement of the particle can be decomposed into a circular motion around a point called *guiding centre* and the translation $\vec{T}$ of the latter, resulting in a helical trajectory. Then, the particle's position $\vec{x}$ can be written as

$$\begin{aligned} \vec{x} &= \vec{T} + \vec{\rho} \\ &= \vec{T} + \frac{m}{eB_0^2}\vec{v} \times \vec{B}_0, \end{aligned} \tag{5.6}$$

where $\vec{\rho}$ is the rotating Larmor radius induced by the Lorentz force (Eq. 2.1). If now an additional force $\vec{F}$ is present, the equations of motions are:

$$\begin{aligned} \dot{\vec{x}} &= \vec{v} \\ m\dot{\vec{v}} &= e \cdot (\vec{E} + \vec{v} \times \vec{B}) + \vec{F}, \end{aligned} \tag{5.7}$$

and the guiding centre moves with the velocity $\vec{v}_g$ [12]:

$$\begin{aligned} \vec{v}_g = \dot{\vec{T}} &= \dot{\vec{x}} - \dot{\vec{\rho}} \\ &= \vec{v}_{||} + \frac{\vec{F} \times \vec{B}_0}{eB_0^2}, \end{aligned} \tag{5.8}$$

where $\vec{v}_{||}$ is the velocity component parallel to $\vec{B}_0$. Inside the Wien filter the additional force is given by Eq. 5.5. Since it acts perpendicular to $\vec{B}_0$, the transverse drift of the guiding centre is given by

$$v_{g,\perp} = \frac{2vB}{B_0}. \tag{5.9}$$

Let us assume that the Wien filter has a certain length L. An electron of velocity v, then needs the time $t = L/v$ to travel through it. During this time the electron gets deflected by a transverse distance Δy from its original path of flight:

$$\Delta y = v_{g,\perp} \cdot t = 2L\frac{B}{B_0}. \tag{5.10}$$

Note that, due to Eq. 5.8, this deflection is perpendicular both to the applied force and the longitudinal magnetic field.

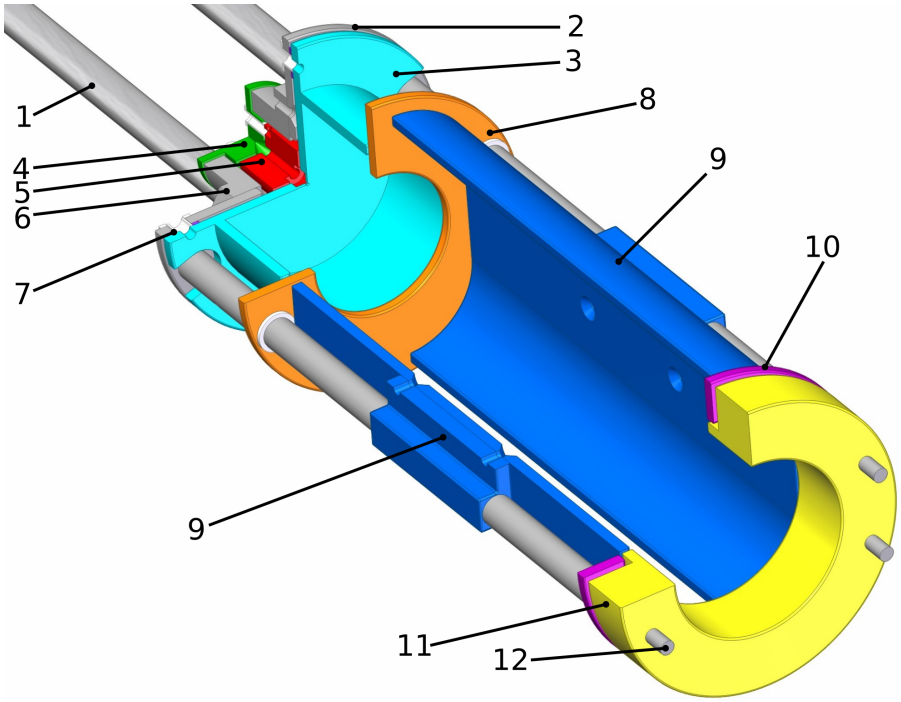

Figure 5.7: Cut through the collector showing: 1 – aluminium rods to flange, 2 – mounting ring, 3 – main cup, 4 – analyser collector, 5 – blocking electrode, 6 – analyser mounting, 7 – sapphire washers, 8 – aperture, 9 – Wien filter electrodes, 10 – secondary collector, 11 – repeller, 12 – thread rods. Not shown are the flange and the coils for the magnetic Wien filter field, which are located outside the vacuum pipe.

5.2 Design

5.2.1 Overview

Fig. 5.7 depicts the final design of the collector. Like in the test set-up described in Sec. 5.1.2.1 everything clings to three massive aluminium rods, which have a diameter of 10 mm. On one side they are directly connected to a stainless steel mounting ring. Not shown here (but in Fig. 5.1) is the outer CF flange, onto which the rods are fastened on the other side. The ring itself holds four stainless steel thread rods, onto which the front electrodes are stacked. Stainless steel tubes lined up on the thread rods are used as spacers between the different elements. By using the same material for the electrodes, spacers and thread rods, uniform thermal expansion and shrinkage can be achieved. This way, the positions of the electrodes relative to each other can be maintained. Electric isolation is ensured with additional ceramics (all white parts in Fig. 5.7). The main cup, however, is mounted directly to the ring with screws isolated not only with ceramics but also with four sapphire washers to ensure sufficient heat conductance. The analyser cup is attached to the back side of the ring.

In order to prevent electrons from backstreaming, the collector is equipped not only with a repeller electrode (11 in Fig. 5.7) but also with a Wien filter. The electric field of the latter is realised by two rounded plate electrodes located between the repeller and the main cup (9 in Fig. 5.7). The magnetic field is built up

Material	Application
stainless steel (1.4435)	electrodes, mounting devices, spacers
aluminium	rods to flange
sapphire (Al_2O_3 monocrystal)	electric isolation, thermal coupling
ceramics (Al_2O_3)	electric isolation
silver	coating for screws

Table 5.1: Materials used for the collector.

by two Helmholtz-like coils (not shown in Fig. 5.7). Due to the non-negligible ohmic heat impact the required current could have on the UHV, it has been decided to place the coils outside the vacuum pipe. The secondary collector (10 in Fig. 5.7) is realised as an additional ring electrode enclosing the back of the repeller. This arrangement given, the primary electron beam is not affected by the potential of the secondary collector. Further details can be found in Sec. 5.2.2.

The analyser cup and associated measurement techniques are presented in more detail in Sec. 5.2.3. In order to facilitate beam profile analyses, the main cup is terminated on the front end by a well-defined aperture (8 in Fig. 5.7). Its opening has a diameter of $40\,\mathrm{mm}$.

As explained above the collector is operated in UHV and, thus, needs to be bakeable. All materials have been chosen accordingly and are summarised in Table 5.1.

5.2.2 The Wien filter

5.2.2.1 The magnetic field

In Sec. 5.1.3 the mathematical framework behind the actions happening in a Wien filter has been presented. When designing the Wien filter for the CSR eCool, the following values have been presumed:

$$B_0 = 250\,\mathrm{Gs}, \quad L = 150\,\mathrm{mm}, \quad \Delta y = 30\,\mathrm{mm}. \tag{5.11}$$

The value of the transverse drift Δy needs to lie in between the inner and the outer radius of the secondary collector electrode so that the deflected secondaries are caught by the same. These radii have sizes of $29.0\,\mathrm{mm}$ and $41.5\,\mathrm{mm}$ respectively. With the help of Eq. 5.10 the transverse magnetic field, that needs to be implemented in the Wien filter, can be calculated:

$$\begin{aligned} B &= \frac{\Delta y \cdot B_0}{2L} \\ &= 25\,\mathrm{Gs}. \end{aligned} \tag{5.12}$$

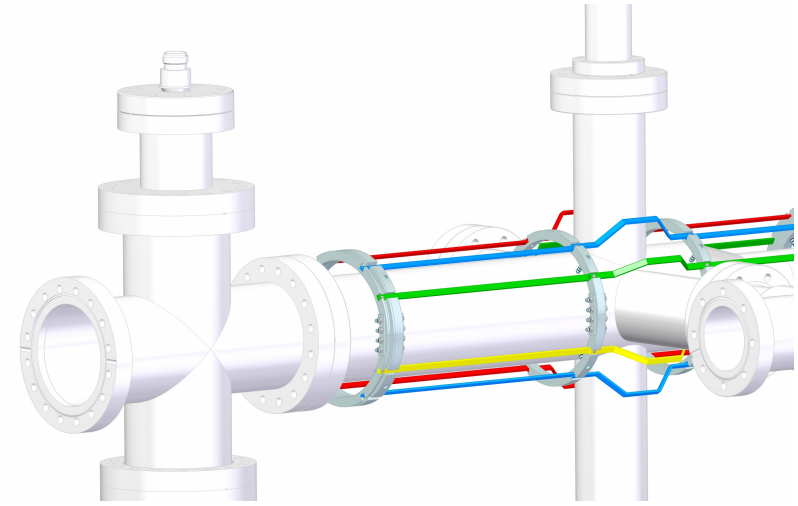

Figure 5.8: Arrangement of the mounting rack for steerer and Wien filter coils around the beam pipe in the collector region. For the magnetic coils of the Wien filter the green and yellow supports are designated. The collector flange will be connected to the open side of the CF 100 cross chamber shown on the left-hand side of the model. Image courtesy of S. Vogel.

This field is provided by two coils, which have to be placed outside of the vacuum pipe to not diminish the UHV. For this purpose the existing rack, on which the magnetic steerer coils[1] are mounted, is used. The arrangement of the same around the vacuum pipe is illustrated in Fig. 5.8. Shown is only the region where the collector is located.

Fig. 5.9 shows the whole rack together with the relevant measures. In contrast to the steerers, however, the Wien filter only needs to span the distance between the last two aluminium rings (denoted by b in Fig. 5.9). For the two Wien filter coils the green and yellow coloured supports are foreseen, which are at an angle of $\pm 30^\circ$ respectively from the centre plane. The magnetic field at the midpoint between two rectangular coils situated at this exact angle can be very well approximated by the well-known formula related to a Helmholtz geometry:

$$B = \frac{8\mu_0 I \cdot N}{\sqrt{125} \cdot c}, \tag{5.13}$$

where μ_0 is the vacuum permeability, I the coil current, N the number of turns for each coil and c the distance between the two coils. In order to reach a field strength of $B = 25\,\mathrm{Gs}$,

$$I \cdot N = 211\,\mathrm{A\,turns} \tag{5.14}$$

are necessary for each coil.

[1] These are two pairs of magnetic coils, which are used to deflect the electron beam both vertically and horizontally. They can be employed for beam profile measurements (see Sec. 5.2.3).

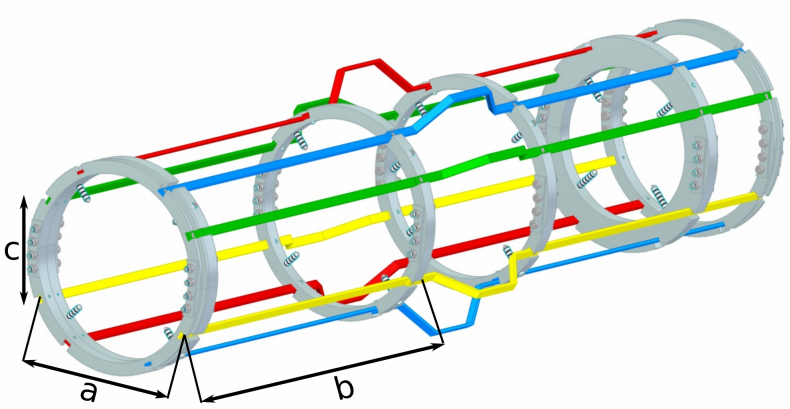

Figure 5.9: Mounting rack for steerer and Wien filter coils. The latter only need to span the distance between the last two aluminium rings (length b). The measures are: $a = 129\,\mathrm{mm}$, $b = 270\,\mathrm{mm}$ and $c = 76\,\mathrm{mm}$. Image courtesy of S. Vogel.

5.2.2.2 The electric field

The electric field which needs to be applied across the Wien filter can be calculated by combining Eqs. 5.4 and 5.12. Neglecting space charge effects, the velocity of the electrons is simply determined by the potential difference U_e along the length of the collector. This does not equal the potential difference between the photocathode and the main cup because the electrons are decelerated before they reach the collector. With a typical value of $U_e = 30\,\mathrm{V}$, the calculation yields

$$\begin{aligned} E &= v \cdot B \\ &= \sqrt{\frac{2U_e e}{m}} \cdot B \\ &= 8121\,\mathrm{V\,m^{-1}}. \end{aligned} \tag{5.15}$$

The most simple way of realising such an electric field is a parallel-plate capacitor with electrodes separated by a distance d and using the vacuum as dielectric. Setting $d = 50\,\mathrm{mm}$ the voltage U_{WF} across those plates is given by

$$\begin{aligned} U_{WF} &= E \cdot d \\ &= 406\,\mathrm{V}. \end{aligned} \tag{5.16}$$

The electric potential distribution inside the collector has been simulated with SIMION [60]. The simulation includes the repeller electrode (set to $-1000\,\mathrm{V}$), the secondary collector ($-950\,\mathrm{V}$), two Wien filter electrodes ($-770\,\mathrm{V}$ left and $-1170\,\mathrm{V}$ right), the aperture ($-870\,\mathrm{V}$), the main cup ($-870\,\mathrm{V}$) and the grounded vacuum pipe. In a first version the Wien filter consisted indeed only of two parallel plates. Fig. 5.11 shows two profiles of this first version transverse to the electron beam's direction of movement with equipotential lines drawn in blue. The left cross section is taken right at the beginning of the Wien filter on the repeller

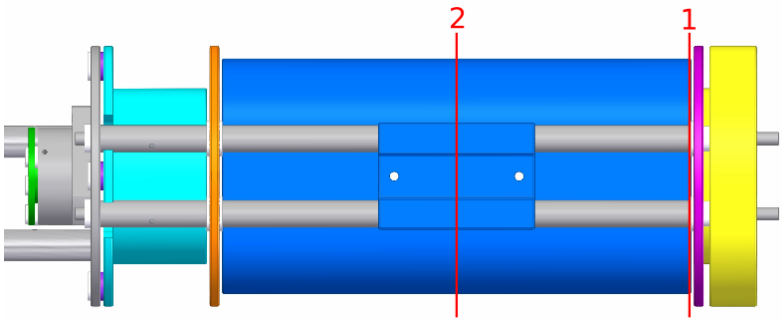

Figure 5.10: Side view of the collector. The red lines indicate the positions of the cuts for the display of the equipotential line distribution inside the Wien filter. Thereby, 1 (2) corresponds to the left-hand (right-hand) side of Fig. 5.11 and Fig. 5.12 respectively.

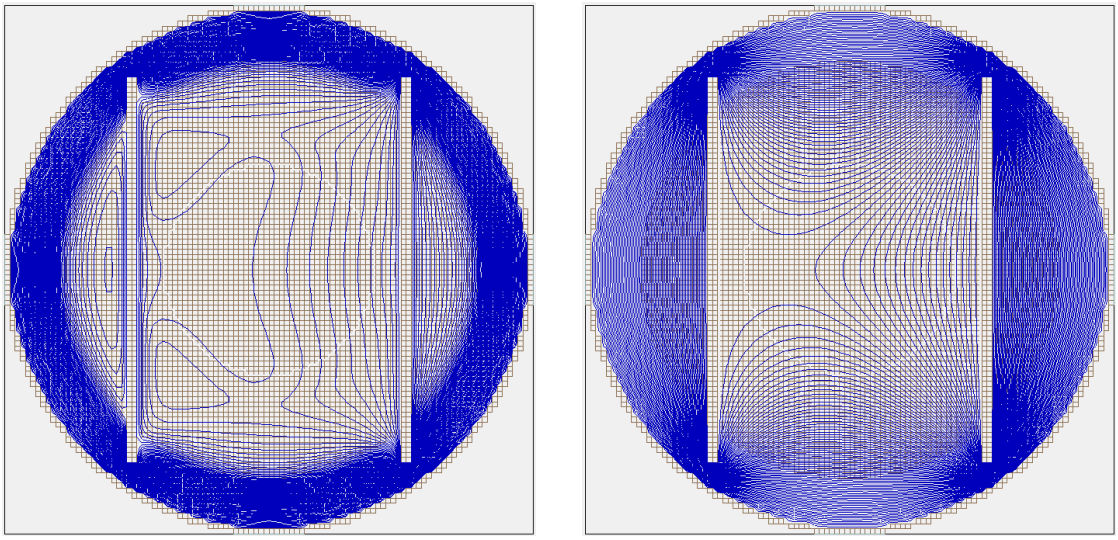

Figure 5.11: Transverse profiles of the first version of the Wien filter taken at the beginning (left) and in the centre (right) of the Wien filter as indicated in Fig. 5.10. The surrounding vacuum pipe is grounded, and the voltages applied to the plate electrodes are $-770\,\mathrm{V}$ (left) and $-1170\,\mathrm{V}$ (right). See text for other electrodes. The blue lines are equipotential lines simulated with SIMION.

side, whereas the right one's location is in the centre of the Wien filter. The locations of these cuts are indicated in Fig. 5.10

In order for the Wien filter to work, a homogeneous electric field, which is perpendicular to both magnetic fields, is needed. The equipotential lines of such a field would be parallel to the electrodes. This is obviously not the case for the design shown in Fig. 5.11. Instead, the electric Wien filter field is distorted by the influence of the grounded vacuum pipe. To solve this problem, the Wien filter has been partially closed at the top and at the bottom so that the distance between the electrodes decreases from $50\,\mathrm{mm}$ in the centre to only $10\,\mathrm{mm}$. Fig. 5.12 (top panel) shows cross sections of this scheme at the same positions as for the open case. One can see that now the equipotential lines in the relevant region, in the centre of the beam pipe, are indeed approximately parallel in both cuts.

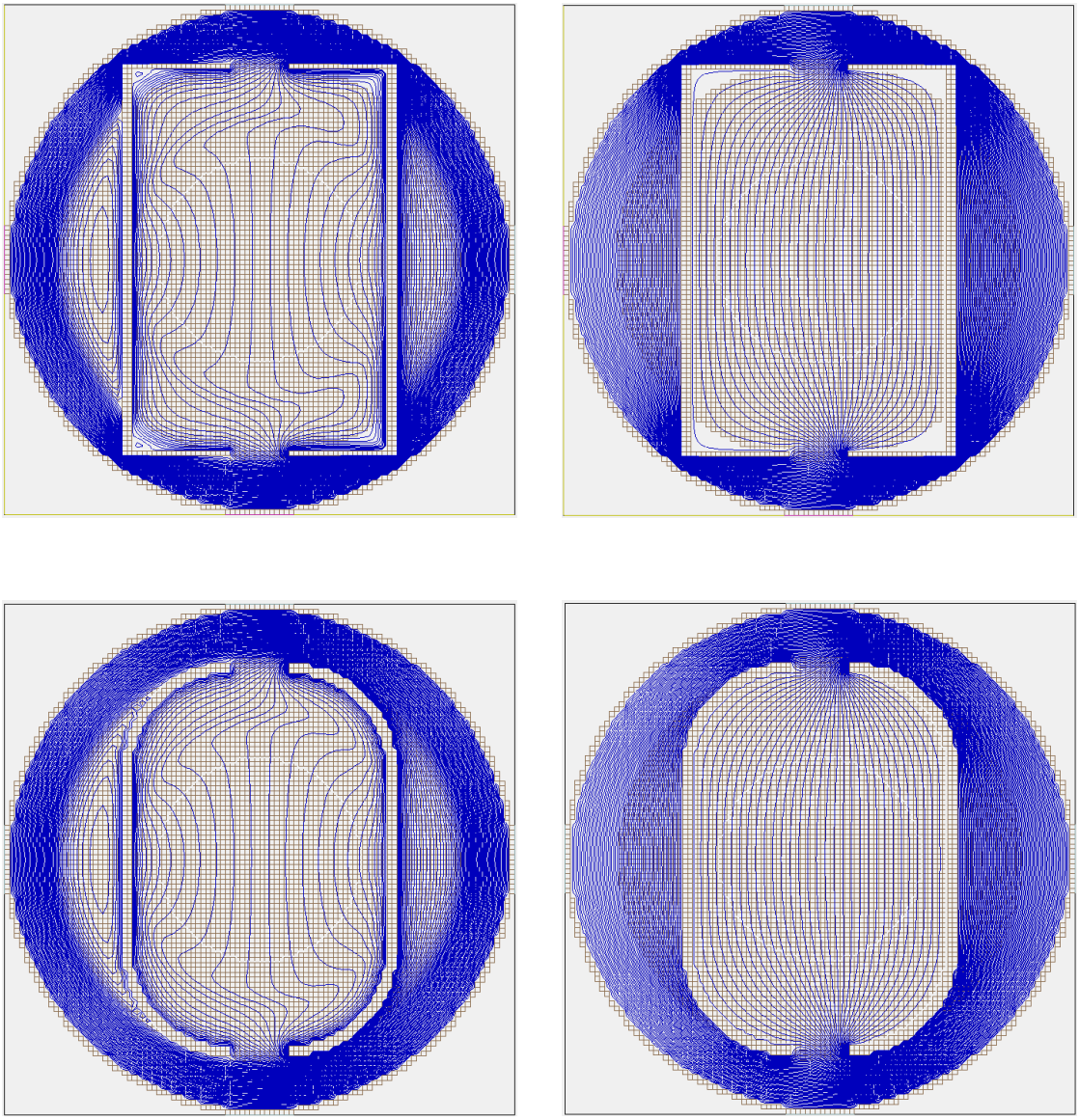

Figure 5.12: Transverse profiles of the partially closed Wien filter. The second version (top) is still of rectangular design while the third and final version (bottom) is rounded for better homogeneity. In both cases the cross sections are located in the beginning (left) and in the centre (right) of the Wien filter as indicated in Fig. 5.10. The surrounding vacuum pipe is grounded, the voltages applied to the plate electrodes are $-770\,\mathrm{V}$ (left) and $-1170\,\mathrm{V}$ (right). See text for other electrodes. The blue lines are equipotential lines simulated with SIMION.

However, it is also visible that the density of field lines around the edges of the electrodes is quite high. In order to prevent sparkovers, the upper and lower parts of the plates are, therefore, designed as $90°$ circle sectors (bottom panel of Fig. 5.12). Furthermore, all edges of the electrodes have been rounded. This electrode shape has the additional advantage that the transition from the Wien filter geometry to the circular geometry of the neighbouring electrodes is not as extreme as in the rectangular case. The field line distribution at the beginning of the Wien filter (left side of Fig. 5.12) is, hence, less irregular.

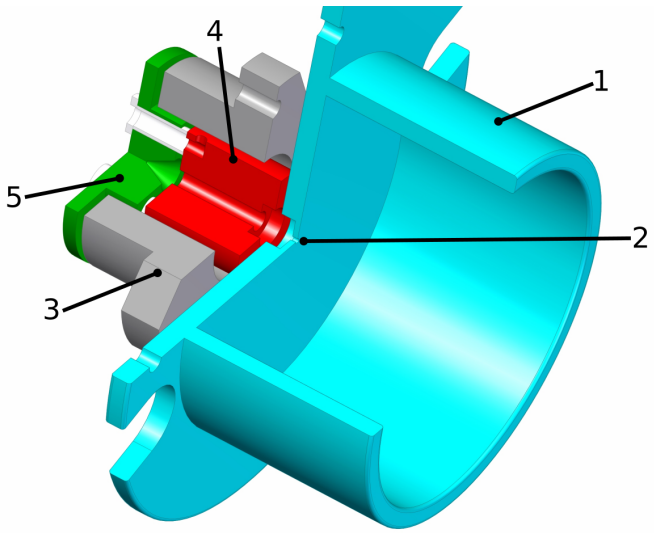

Figure 5.13: Cut through the back part of the collector showing: 1 – main cup, 2 – pinhole, 3 – analyser mounting, 4 – blocking electrode, 5 – analyser collector. All pieces coloured in white are isolating ceramics. Not depicted is the mounting ring, to which the main cup as well as the analyser mounting are attached.

5.2.3 The analyser cup

It has already been mentioned that the major part of the electrons is absorbed by the material of the main cup. By connecting this cup to a floating ammeter, monitoring of the total electron current during an experiment is, therefore, possible. This is already an important quantity. However, as has been shown in Sec. 3.5, for the analysis of data from recombination experiments it is essential to know the electron density. Thus, current and velocity distributions of the electrons in the beam need to be determined. In order to gain this information, the analyser cup is needed. Fig. 5.13 shows the arrangement of the main cup (1 in Fig. 5.13) and the different elements of the analyser cup. Into the centre of the former a small hole with a diameter of $0.8\,\mathrm{mm}$ is drilled. This can easily be spotted in the photograph shown in Fig. 5.14. Via this pinhole a small fraction of the beam can enter the analyser. It first passes through the cylindrical *blocking electrode* (4 in Fig. 5.13) before it is collected by the *analyser collector* (5 in Fig. 5.13). One can assume that the electron density is constant over the beam profile and that the amount of electrons passing through the pinhole is very small compared to the total current. Then, the proportion of the current measured at the analyser collector I_{Ana} to the one detected at the main cup I_{Cup} is determined by the ratio of the pinhole and beam diameters d_{ph} and d_{beam}

$$\frac{I_{Ana}}{I_{Cup}} = \frac{d_{ph}^2}{d_{beam}^2}. \tag{5.17}$$

Considering the small value of I_{Cup} (typically around $100\,\mu\mathrm{A}$), the diameter of the pinhole has been chosen not too tiny in order to guarantee a good signal-to-noise ratio in the current measurements at the analyser collector.

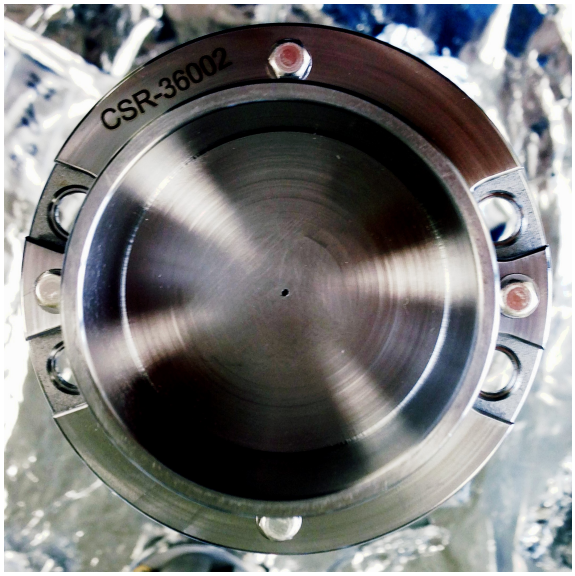

Figure 5.14: Photograph of the main cup. In the centre the pinhole with a diameter of $0.8\,\mathrm{mm}$ can be seen.

5.2.3.1 Beam profile measurements

With the analyser cup two types of experiments can be performed, which are introduced in the following.

First, horizontal and vertical beam profiles can be determined. With help of the magnetic steering coils the beam is driven across the pinhole, and the analyser collector current is measured as a function of the deflection. The blocking electrode is meanwhile grounded. To not distort the deflection, the Wien filter needs to be switched off while performing the measurement. Since there are two pairs of coils perpendicular to each other, a two-dimensional profile can be obtained.

For such measurements it is actually advantageous if the pinhole diameter is as small as possible. Its actual dimension is, thus, a compromise between the two demands stated above. In addition, the requirement of being able to steer the beam in its whole extent over the pinhole sets a lower limit on the aperture diameter. It has to be at least twice as big as the maximum beam diameter. Since the latter adds up to $26.8\,\mathrm{mm}$, the chosen value of $40\,\mathrm{mm}$ is sufficient.

A homogeneous electron density distribution ($n_e = $ const. inside the beam, $n_e = 0$ everywhere else) is of high importance for recombination experiments. However, a wrong voltage setting between the extracting Pierce electrode and the cathode can lead to slightly hollow or constricted beam profiles [64]. Beam profile measurements conducted with the analyser cup provide a tool for testing whether this is the case. This way, the optimal settings for the operation of the photocathode can be found.

Furthermore, the adiabatic transverse expansion of the electron beam can be demonstrated experimentally. For this purpose beam diameters at different magnetic expansion factor can be determined.

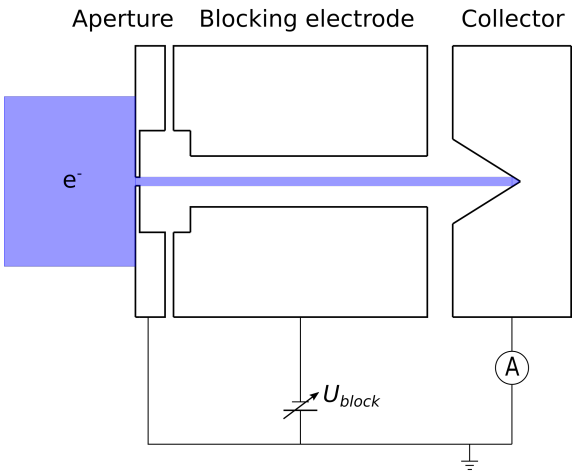

Figure 5.15: Working principle of a retarding field analyser. The main electron current is caught in the main cup. Only a small fraction flows through the entering aperture towards the analyser collector. The voltage applied to the blocking electrode U_{block} can be adjusted, and the arriving current is measured as a function of the same. This way the energy of the electrons can be determined.

5.2.3.2 Energy distribution measurements

The analyser cup can also be employed as a retarding field analyser. Such a device is used to measure the longitudinal energy distribution in the beam. As explained in Sec. 3.3.2, at an electron cooler featuring adiabatic transverse expansion it is also possible to indirectly determine the transverse beam temperature from that. Fig. 5.15 demonstrates the principle behind such a measurement. A voltage U_{block} is applied to the blocking electrode and increased. Thus, the blocking electrode acts as a potential wall. When the collector current is measured as a function of U_{block}, the longitudinal kinetic energy distribution of the electrons can be found by differentiation of the signal. This is of course not the same for all particles, but instead it can be described by a Maxwell-Boltzmann distribution. Alternatively, a cumulative distribution function can be fitted to the obtained curve and the energy spread can be obtained from that. With the help of Eq. 3.15 the longitudinal temperature can then be calculated.

Measurements of this kind have been conducted, among others, by F. Sprenger at the TSR electron target. [64]. Thereby, it has been seen that a large opening of the blocking electrode as compared to its length leads to partial shielding of the electrons in the centre of the beam [64]. Therefore, they do not experience the full blocking voltage, which complicates the energy distribution measurements. Based on this experience, for the design at hand a blocking electrode length of $15\,\mathrm{mm}$ and an opening diameter of $3\,\mathrm{mm}$ have been selected.

From the total beam diameter, the current distribution inside the beam and the velocity distribution of the electrons the electron density can be computed. The implementation of an analyser cup, thus, enables the calculation of rate coefficients of electron-ion recombination reactions.

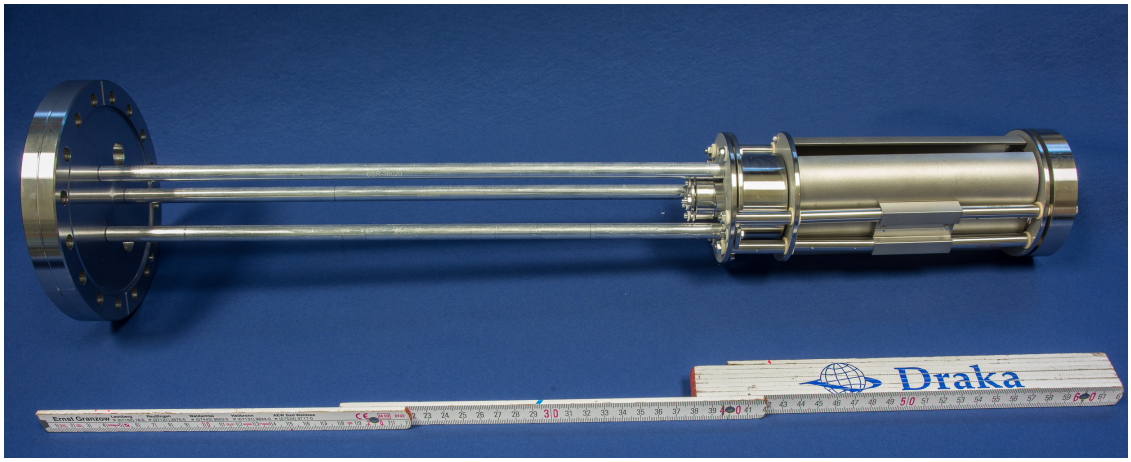

Figure 5.16: Photograph of the complete electron collector. A foot rule is included in the picture to demonstrate its scale. Not shown are the magnetic field coils, which will be installed outside the vacuum pipe.

5.3 Present status

In the course of this work the design of the electron collector has been completed. All parts have been manufactured and assembled as it is shown in Fig. 5.16.

The design is tailored to the fact that the vacuum system of the collector section is already constructed. Everything clings to one CF flange, which can be seen on the very left of the photograph. The three long aluminium rods bear a mounting ring, to which all electrodes are attached. Thus, the whole assembly can be installed by simply connecting the flange to the end of the vacuum pipe. Not yet included in the photograph are the electric connections. Via two four-pin high voltage feedthroughs (DN16CF-4Pin-Cu-6kV-Ceramtec 9871-08-CF) attached to the flange they can be contacted from outside.

The only parts isolated from this assembly are the magnetic field coils for the Wien filter. They will be installed outside the vacuum pipe so that the ohmic heat from the current flowing through does not downgrade the vacuum. It has been demonstrated above that the magnetic and electric Wien filter fields need to be perpendicular both to the direction of movement of the electron beam and to each other. While the former is intrinsically secured by the design, the latter has to be assured during installation. When the magnetic coils are wound around the designated racks (see Fig. 5.8), the magnetic field lines are vertical. This implies that the collector has to be build into the vacuum pipe in such a way that the electric field lines are horizontal, i.e. the Wien filter electrodes need to lie to the left and to the right of the beam trajectory.

The eCool is planned to be installed in the CSR in spring 2016. In the course of this action the collector will be build in as well. As has been explained above, it can be employed to characterise the photocathode and the magnetic guiding field of the electron cooler. Such measurements are actually independent of the status of the CSR. They can be performed without the need to cool down the ring and even without a stored ion beam. Therefore, the first applications of the collector will be to characterise the eCool and to find the optimal settings for cooling and recombination experiments.

Chapter 6

Summary and outlook

In 2016 a low-energy electron cooler will be installed in the cryogenic storage ring CSR. The two different projects that have been subject of the present work make important contributions to the eCool's functionality both as a cooler and as a target for recombination experiments.

One requirement for a properly functioning electron cooler is the complete overlap of the electron beam with the stored ion beam. It has been shown that only then cooling at zero relative velocity is possible. To ensure this, the eCool interaction region is equipped with two rotating wire scanners. Their angle of rotation can be set and read from outside the CSR cryostat with a precision of 1° while keeping almost perfect thermal isolation. In a next step a stepper motor should be installed to perform this task automatically.

The scanners are of a dual-wire design. Thus, the electron beam induces a signal twice per 180° rotation. Due to the extent of the beam, both signals have a finite width, which roughly corresponds to the beam diameter. For each signal a mean angle can be calculated. Within the scope of this work a scheme has been developed to determine the transverse beam position from these two angles. With this scheme the beam centre can be unambiguously identified within a spatial resolution of $1\,\mathrm{mm}$.

The wire scanners are also to be used to find the transverse location of the ion beam. However, since the induced current signal would be too weak to be measurable, they are employed as scrapers. As they are turned across the beamline, they cut away an increasing part of the beam. A procedure has been proposed how the loss in intensity as a function of the rotation angle can be observed with the CSR's current pick-up. When the scraper reaches the closed orbit, the signal vanishes. By injecting ions twice and scraping away the beam from opposite directions, two angles are acquired, to which the developed scheme can be applied. According to the simulation it is possible to determine the ion beam centre with the same precision as the one of the electron beam. However, the sensitivity of the current pick-up has also to be taken into account. Experimental confirmation of the suggested procedure is, therefore, needed in upcoming CSR beamtimes with the electron cooler installed.

A necessary step towards the completion of the electron cooler has been the development of the electron collector. The electron current is absorbed by a Faraday cup. Due to the small incoming power (maximum

$1\,\mathrm{W}$), we have abstained from implementing additional water cooling. The thermal conductance has been measured at a test set-up, and the maximum temperature difference across the set-up length has been found to be $13.4\,^{\circ}\mathrm{C}$, which is tolerable for a UHV set-up. In addition, the collector features an analyser cup, thus, allowing for further characterisation of the electron beam. With the help of magnetic steering coils and a pinhole transition between the two cups, two-dimensional beam profiles can be obtained. From this information together with the total current the electron density can be computed. Knowing its value is essential for precise determination of the merged-beams rate coefficient of a reaction. Also, the analyser cup can be used as a retarding field analyser to measure the longitudinal beam temperature. Since the electron cooler works with adiabatic transverse expansion, from this the transverse temperature can be calculated when measurements at different expansion factors are conducted.

A novelty, as compared to the electron collectors used at the TSR, is the implementation of a Wien filter. This device is included to prevent secondary and reflected electrons from travelling back to the photocathode or towards the cryogenic vacuum chamber walls of the CSR. The former would be damaged, and if the electrons arrive at the latter, localised vacuum degradation in the interaction section is the consequence. The necessary magnetic and electric field strengths have been calculated. The magnetic field will be realised in the form of a pair of Helmholtz-like coils with $211\,\mathrm{A\,turns}$ applied to each coil. They will be placed outside the vacuum pipe and still need to be installed. The electric field configuration of the entirety of the collector electrodes has been simulated. The shape of the Wien filter electrodes has been adjusted such that the field lines are as homogeneous as possible. The electric field and, thus, the voltage across the electrodes needs to be adapted to the electron energy. For a typical value of $30\,\mathrm{eV}$ $406\,\mathrm{V}$ need to be applied.

Presently, the electron cooler is being assembled. It is planned to be integrated into the CSR in spring 2016. At first, the collector and the wire scanners can be employed to further characterise the electron beam produced by the photocathode. Additionally, the functionality of the adiabatic transverse expansion can be tested. This way, suitable settings for electron cooling and recombination experiments can be found. The performed phase space cooling will generate ion beams of higher intensity and quality than now available. All experiments performed with the CSR will benefit from the longer life times and increased energy resolution.

However, for the time being, the CSR is the only cryogenic, electrostatic storage ring featuring an electron cooler. This provides the opportunity for a unique experimental programme. One example introduced in this work is the dissociative recombination of molecular ions in their rotational and vibrational ground state. Thus, conditions of the cold plasma as it is present in the interstellar medium can, for the first time, be mimicked by a laboratory experiment.

Appendix A

Mathematica script for beam position determination with scraper wires

(* Programme for the calculation of the transverse beam coordinates (x,y) from two angles measured with the rotating wire scanners of the CSR eCool. *)

(* All lengths are in mm, all angles in rad *)

(* Input: measured angles *)

(* $\alpha 1$ (from Scraper1) should be smaller than $\alpha 2$ (from Scraper 2) *)

α1=1.061

α2=2.080

(* Used parameters from scraper model *)

radius=51.5

aconst=59.06059

cconst=-128.04419

ϕmin=2.42194

ϕmax=3.86125

(* Rotation matrix for rotation around the y axis *)

rot[α_]:=RotationMatrix[α, {0, 1, 0}]

(* Description of Scraper 1 and Scraper 2 in Cartesian coordinates. r, a and c are given by the model and are specified in the parameters given above. ϕ is a variable ranging between ϕmin and ϕmax. *)

scraper1[ϕ_, r_, a_, c_]:={r * Cos[ϕ], r * Sin[ϕ], 0.5 * (a * ϕ + c)}

scraper2[ϕ_, r_, a_, c_]:={r * Cos[ϕ], r * Sin[ϕ], −0.5 * (a * ϕ + c)}

(* Plot of the non-rotated system *)

ParametricPlot3D[{scraper1[ϕ, radius, aconst, cconst], scraper2[ϕ, radius, aconst, cconst]}, {ϕ, 2.42199, 3.86119},
PlotRange → All, AxesLabel → {x, y, z}, ViewPoint → Above]

(* Rotations of scraper 1 and 2 by multiplication with the rotation matrix *)

rotscraper1 = rot[α1].scraper1[ϕ, radius, aconst, cconst]

rotscraper2 = rot[α2].scraper2[ϕ, radius, aconst, cconst]

(* x coordinates of rotscraper1 and rotscraper2 give system of equations with two unknowns: ϕ and x (x coord of beam position) *)

sol = Solve[{x == rotscraper1[[1]], x == rotscraper2[[1]]}, {x, ϕ}, Reals]

(* The y coordinate can be calculated from ϕ and the definition of the scraper *)

ypos = radius * Sin[ϕ/.sol[[1, 2]]]

beamposition = {x/.sol[[1, 1]], ypos}

(*Testing of the above scheme by calculating backwards*)

xbeam =0

ybeam = 0

ϕtest = ϕtemp/.Solve[{ybeam == scraper1[ϕtemp, radius, aconst, cconst][[2]], ϕmin ≤ ϕtemp ≤ ϕmax}, ϕtemp, Reals]

(* Calculate $\alpha 1$ *)

soltest1 = Solve[{xbeam==(rot[α1test].scraper1[ϕtest, radius, aconst, cconst])[[1]], 0<=α1test ≤ Pi}, α1test, Reals]

(* Calculate $\alpha 2$ *)

soltest2 = Solve[{xbeam==(rot[α2test].scraper2[ϕtest, radius, aconst, cconst])[[1]], 0<=α2test ≤ Pi}, α2test, Reals]

Bibliography

[1] K. Abrahamsson, G. Andler, L. Bagge, E. Beebe, P. Carlé, H. Danared, S. Egnell, K. Ehrnstén, M. Engström, C. Herrlander, et al. CRYRING: A synchrotron, cooler and storage ring. *Nuclear Instruments and Methods in Physics Research Section B: Beam Interactions with Materials and Atoms*, 79(1):269–272, 1993.

[2] J. U. Andersen, P. Hvelplund, S. B. Nielsen, U. Pedersen, and S. Tomita. Statistical electron emission after laser excitation of C_{60}^- ions from an electrospray source. *Physical Review A*, 65(5):053202, 2002.

[3] J. U. Andersen, P. Hvelplund, S. B. Nielsen, S. Tomita, H. Wahlgreen, S. P. Møller, U. V. Pedersen, J. S. Forster, and T. J. Jørgensen. The combination of an electrospray ion source and an electrostatic storage ring for lifetime and spectroscopy experiments on biomolecules. *Review of Scientific instruments*, 73(3):1284–1287, 2002.

[4] A. Becker. *Imaging of Neutral Fragmentation Products from Fast Molecular Ion Beams: Paving the Way for Reaction Studies in Cryogenic Environment*. PhD thesis, Universität Heidelberg, in preparation.

[5] F. Berg. *Die Ionenoptik der Injektionsstrahlführungslinien des kryogenen Speicherrings CSR*. Diploma thesis, Universität Heidelberg, 2011.

[6] C. Bond and S. Gordon. A wide aperture high gain beam profile scanner. *Nuclear Instruments and Methods*, 98(3):513–523, 1972.

[7] M. Bryzgunov, A. Ivanov, V. Panasyuk, V. Parkhomchuk, and V. Reva. Efficiency improvement of an electron collector intended for electron cooling systems using a Wien filter. *Technical Physics*, 58(6):911–918, 2013.

[8] G. I. Budker and A. N. Skrinskiĭ. Electron cooling and new possibilities in elementary particle physics. *Physics-Uspekhi*, 21(4):277, 1978.

[9] CERN. http://home.cern/about/updates/.

[10] J. Cockcroft and E. Walton. Experiments with high velocity positive ions. ii. The disintegration of elements by high velocity protons. In *Proceedings of the Royal Society of London A: Mathematical, Physical and Engineering Sciences*, volume 137, pages 229 – 242. The Royal Society, 1932.

[11] H. Danared, G. Andler, L. Bagge, C. Herrlander, J. Hilke, J. Jeansson, A. Källberg, A. Nilsson, A. Paál, K.-G. Rensfelt, et al. Electron cooling with an ultracold electron beam. *Physical review letters*, 72(24):3775, 1994.

[12] H. J. de Blank. Guiding center motion. *Fusion Science and Technology*, 49(2T):59–66, 2006.

[13] S. F. dos Santos, V. Kokoouline, and C. H. Greene. Dissociative recombination of H_3^+ in the ground and excited vibrational states. *The Journal of Chemical Physics*, 127(12):124309, 2007.

[14] A. Ehlerding, A. Viggiano, F. Hellberg, R. D. Thomas, V. Zhaunerchyk, W. D. Geppert, H. Montaigne, M. Kaminska, F. Österdahl, M. Af Ugglas, et al. The dissociative recombination of fluorocarbon ions III: CF_2^+ and CF_3^+. *Journal of Physics B: Atomic, Molecular and Optical Physics*, 39(4):805, 2006.

[15] Y. Enomoto, Y. Nakano, T. Masunaga, and T. Azuma. Development and commissioning of RIken Cryogenic Electrostatic ring (RICE). In *Journal of Physics: Conference Series*, volume 635, page 022028. IOP Publishing, 2015.

[16] H. Fadil, M. Grieser, R. Von Hahn, and A. Wolf. Finite elements calculations of the lattice and ring acceptance of the Heidelberg CSR. In *EPAC2006-Tenth European Particle Accelerator Conference*, 2006.

[17] A. Florescu-Mitchell and J. Mitchell. Dissociative recombination. *Physics Reports*, 430(5):277–374, 2006.

[18] B. Franzke. The heavy ion storage and cooler ring project ESR at GSI. *Nuclear Instruments and Methods in Physics Research Section B: Beam Interactions with Materials and Atoms*, 24:18–25, 1987.

[19] V. Georgieva, A. Bogaerts, and R. Gijbels. Numerical study of $Ar/CF_4/N_2$ discharges in single-and dual-frequency capacitively coupled plasma reactors. *Journal of applied physics*, 94(6):3748–3756, 2003.

[20] M. Grieser. private communication. 2015.

[21] M. Grieser, R. Bastert, K. Blaum, H. Buhr, D. Fischer, F. Laux, R. Repnow, T. Sieber, R. von Hahn, A. Wolf, et al. The diagnostics system at the Cryogenic Storage Ring CSR. *Proceedings of IPAC*, 2010.

[22] M. Grieser, A. Becker, K. Blaum, S. George, R. von Hahn, C. Krantz, S. Vogel, and A. Wolf. The status of the diagnostic system at the cryogenic storage ring CSR. In *Proceedings of the 5th International Particle Accelerator Conference*, pages 3521–3523, 2014.

[23] F. Grussie. PhD thesis, Universität Heidelberg, in preparation.

[24] D. Habs, W. Baumann, J. Berger, P. Blatt, A. Faulstich, P. Krause, G. Kilgus, R. Neumann, W. Petrich, R. Stokstad, et al. First experiments with the Heidelberg test storage ring TSR. *Nuclear Instruments and Methods in Physics Research Section B: Beam Interactions with Materials and Atoms*, 43(3):390–410, 1989.

[25] D. J. Haxton and C. H. Greene. Ab initio frame-transformation calculations of direct and indirect dissociative recombination rates of $HeH^+ + e^-$. *Physical Review A*, 79(2):022701, 2009.

[26] F. Hinterberger. *Physik der Teilchenbeschleuniger und Ionenoptik*. Springer-Verlag, Berlin Heidelberg, 2nd edition, 2008.

[27] G. Hortig. A beam scanner for two dimensional scanning with one rotating wire. *Nuclear Instruments and Methods*, 30(2):355–356, 1964.

[28] J. Jagger, J. Page, and P. Riley. A simple ion beam scanner. *Nuclear Instruments and Methods*, 49(1):121–124, 1967.

[29] T. Katayama, K. Chida, T. Hattori, et al. Present status of cooler synchrotron TARN II. In *Proceedings of the 7th symposium on accelerator science and technology*, 1990.

[30] C. Krantz. *Intense Electron Beams from GaAs Photocathodes as a Tool for Molecular and Atomic Physics*. PhD thesis, Universität Heidelberg, 2009.

[31] C. Krantz, F. Berg, K. Blaum, F. Fellenberger, M. Froese, M. Grieser, R. von Hahn, M. Lange, F. Laux, S. Menk, et al. The cryogenic storage ring and its application to molecular ion recombination physics. In *Journal of Physics: Conference Series*, volume 300, page 012010. IOP Publishing, 2011.

[32] M. Larsson. Dissociative recombination with ion storage rings. *Annual review of physical chemistry*, 48(1):151 – 179, 1997.

[33] M. Larsson. Dissociative recombination and excitation in ion storage rings. In *The Physics of Electronic and Atomic Collisions: XXI International Conference*, volume 500 of *AIP Conference Proceedings*, pages 44 – 64. AIP Publishing, 2000.

[34] J. Lion. *Das mit Flüssigneon gekühlte supraleitende Magnetsystem des Elektronenkühlers am kryogenen Ionen-Speicherring CSR*. Bachelor's thesis, Universität Heidelberg, 2015.

[35] D. Möhl. Phase space cooling in storage rings. *Physica Scripta*, 1988(T22):21, 1988.

[36] D. Möhl and K. Kilian. Phase-space cooling of ion beams. In *Detectors in Heavy-Ion Reactions*, pages 220 – 243. Springer-Verlag, Berlin Heidelberg, 1983.

[37] S. Møller. ASTRID - A storage ring for ions and electrons. In *Particle Accelerator Conference: Accelerator Science and Technology: Conference Record of the 1991 IEEE*, volume 5, pages 2811 – 2813. IEEE, 1991.

[38] S. P. Møller. ELISA, an electrostatic storage ring for atomic physics. *Nuclear Instruments and Methods in Physics Research Section A: Accelerators, Spectrometers, Detectors and Associated Equipment*, 394(3):281–286, 1997.

[39] A. Müller. Plasma rate coefficients for highly charged ion-electron collisions: New experimental access via ion storage rings. *International journal of mass spectrometry*, 192(1):9–22, 1999.

[40] A. Müller and A. Wolf. *Accelerator-based atomic physics techniques and applications*, chapter 5, pages 147 – 182. AIP Press, Woodbury, New York, 1st edition, 1997.

[41] Y. Nakano, W. Morimoto, T. Majima, J. Matsumoto, H. Tanuma, H. Shiromaru, and T. Azuma. A cryogenic electrostatic storage ring project at RIKEN. In *Journal of Physics: Conference Series*, volume 388, page 142027. IOP Publishing, 2012.

[42] O. Novotnỳ, J. Mitchell, J. LeGarrec, A. Florescu-Mitchell, C. Rebrion-Rowe, A. Svendsen, M. El Ghazaly, L. H. Andersen, A. Ehlerding, A. Viggiano, et al. The dissociative recombination of fluorocarbon ions: II. CF^+. *Journal of Physics B: Atomic, Molecular and Optical Physics*, 38(10):1471, 2005.

[43] O. Novotnỳ, O. Motapon, M. Berg, D. Bing, H. Buhr, H. Fadil, M. Grieser, J. Hoffmann, A. Jaroshevich, B. Jordon-Thaden, et al. Dissociative recombination of CF^+: Experiment and theory. In *Journal of Physics: Conference Series*, volume 192, page 012021. IOP Publishing, 2009.

[44] G. K. O'Neill. Storage-ring synchrotron: device for high-energy physics research. *Physical Review*, 102(5):1418, 1956.

[45] D. Orlov, M. Hoppe, U. Weigel, D. Schwalm, A. Terekhov, and A. Wolf. Energy distributions of electrons emitted from GaAs (Cs, O). *Applied Physics Letters*, 78:2721, 2001.

[46] D. Orlov, C. Krantz, A. Shornikov, M. Lestinsky, J. Hoffmann, A. Jaroshevich, S. Kosolobov, A. Terekhov, and A. Wolf. Ultra cold photoelectron beams for ion storage rings. In *Spin Physics: 18th International Spin Physics Symposium*, volume 1149, pages 1007–1016. AIP Publishing, 2009.

[47] D. Orlov, F. Sprenger, M. Lestinsky, U. Weigel, A. Terekhov, D. Schwalm, and A. Wolf. Photocathodes as electron sources for high resolution merged beam experiments. In *Journal of Physics: Conference Series*, volume 4, page 290. IOP Publishing, 2005.

[48] D. Orlov, U. Weigel, D. Schwalm, A. Terekhov, and A. Wolf. Ultra-cold electron source with a GaAs-photocathode. *Nuclear Instruments and Methods in Physics Research Section A: Accelerators, Spectrometers, Detectors and Associated Equipment*, 532(1):418–421, 2004.

[49] D. A. Orlov, M. Lange, M. Froese, R. von Hahn, M. Grieser, V. Mallinger, M. Rappaport, T. Sieber, T. Weber, and A. Wolf. Cryogenic and vacuum technological aspects of the low-energy electrostatic Cryogenic Storage Ring. In *Advances in Cryogenic Engineering: Transactions of the Cryogenic Engineering Conference-CEC, Vol. 53*, volume 985, pages 1233 – 1239. AIP Publishing, 2008.

[50] V. V. Parkhomchuk and A. N. Skrinskiĭ. Electron cooling: 35 years of development. *Physics-Uspekhi*, 43(5):433 – 452, 2000.

[51] S. Pastuszka, U. Schramm, M. Grieser, C. Broude, R. Grimm, D. Habs, J. Kenntner, H.-J. Miesner, T. Schüßler, D. Schwalm, et al. Electron cooling and recombination experiments with an adiabatically expanded electron beam. *Nuclear Instruments and Methods in Physics Research Section A: Accelerators, Spectrometers, Detectors and Associated Equipment*, 369(1):11–22, 1996.

[52] S. Petrie and D. K. Bohme. Ions in space. *Mass spectrometry reviews*, 26(2):258 – 280, 2007.

[53] J. Pierce. Rectilinear flow in electron beams. *Appl. Phys. Lett*, 11:548, 1940.

[54] Rinck Electronic GmbH. *Temperatursensor PT1000, Temperatur/Widerstandstabelle, Bereich* -50 - $200\,^{\circ}\mathrm{C}$. obtained from `http://www.rinck-electronic.de/`, 2010.

[55] M. Sands. *The physics of electron storage rings: An introduction*. Stanford Linear Accelerator Center Stanford, CA 94305, 1970.

[56] J. Scheer and J. van Laar. GaAs-Cs: A new type of photoemitter. *Solid State Communications*, 3(8):189 –193, 1965.

[57] A. Schlachter, J. Stearns, W. Graham, K. Berkner, R. Pyle, and J. Tanis. Electron capture for fast highly charged ions in gas targets: An empirical scaling rule. *Physical Review A*, 27(6):3372, 1983.

[58] H. T. Schmidt, H. A. Johansson, R. D. Thomas, W. D. Geppert, N. Haag, P. Reinhed, S. Rosén, M. Larsson, H. Danared, K.-G. Rensfelt, et al. DESIREE as a new tool for interstellar ion chemistry. *International Journal of Astrobiology*, 7(3-4):205–208, 2008.

[59] F. Schwabl. *Statistische Mechanik*. Springer-Verlag, Berlin Heidelberg, 3rd edition, 2006.

[60] Scientific Instrument Services, Inc. (SIS). *SIMION 8.1*. 2012.

[61] D. Seely, H. Bruhns, D. Savin, T. J. Kvale, E. Galutschek, H. Aliabadi, and C. C. Havener. Rotating dual-wire beam profile monitor optimized for use in merged-beams experiments. *Nuclear Instruments and Methods in Physics Research Section A: Accelerators, Spectrometers, Detectors and Associated Equipment*, 585(1):69–75, 2008.

[62] A. Shornikov. *An electron cooler for ultra-low energy cryogenic operation*. PhD thesis, Universität Heidelberg, 2012.

[63] L. Spitzer, Jr. *Physics of Fully Ionized Gases*. Wiley & Sons, New York London, 2nd edition, 1962.

[64] F. Sprenger. *Production of cold electron beams for collision experiments with stored ions*. PhD thesis, Universität Heidelberg, 2004.

[65] K. Spruck. *Dielectronic recombination experiments with tungsten ions at the test storage ring and development of a single-particle detector at the cryogenic storage ring*. PhD thesis, Universität Giessen, 2015.

[66] T. Tanabe and K. Noda. Storage of bio-molecular ions in the electrostatic storage ring. *Nuclear Instruments and Methods in Physics Research Section A: Accelerators, Spectrometers, Detectors and Associated Equipment*, 496(1):233–237, 2003.

[67] R. D. Thomas. When electrons meet molecular ions and what happens next: Dissociative recombination from interstellar molecular clouds to internal combustion engines. *Mass spectrometry reviews*, 27(5):485–530, 2008.

[68] S. van der Meer. Stochastic damping of betatron oscillations. internal report CERN ISR-PO/72-31, 1972.

[69] S. van der Meer. Phase space cooling. *Phys. Bl.*, 1983.

[70] S. Vogel. *Developments at an electrostatic cryogenic storage ring for electron-cooled* keV *energy ion beams*. PhD thesis, Universität Heidelberg, in preparation.

[71] R. von Hahn, F. Berg, K. Blaum, J. C. Lopez-Urrutia, F. Fellenberger, M. Froese, M. Grieser, C. Krantz, K.-U. Kühnel, M. Lange, et al. The electrostatic cryogenic storage ring CSR – mechanical concept and realization. *Nuclear Instruments and Methods in Physics Research Section B: Beam Interactions with Materials and Atoms*, 269(24):2871–2874, 2011.

[72] U. Weigel. *Cold intense electron beams from Gallium Arsenide photocathodes*. PhD thesis, Universität Heidelberg, 2003.

[73] A. Wolf, R. Von Hahn, M. Grieser, D. Orlov, H. Fadil, C. Welsch, V. Andrianarijaona, A. Diehl, C. Schroter, and J. C. Lopez-Urrutia. The Heidelberg CSR: Stored ion beams in a cryogenic environment. In *AIP Conference Proceedings*, volume 821, page 473. IOP Publishing, 2006.

[74] Wolfram Research, Inc. *Mathematica 10.2*. Champaign, Illinois, 2015.

Acknowledgements

So, that's it! You have read through this whole thesis, which probably means that I have made it through my whole Master's degree in physics. Time to thank a few people:

I would like to thank Andreas Wolf for giving me the opportunity to work on the two presented projects and make my small contribution to the big CSR project. The timing of my thesis made it possible for me to not only focus on the work written down here but to also witness the first cryogenic beamtime at the CSR. I am grateful for having been part of the team and for the time I was allowed to just hang around the control room. I think I learned a lot from this.

Claude Krantz and Stephen Vogel supervised me during my work. Thank you both a lot for all the help and support and the nice working atmosphere.

In addition, I would like to thank Manfred Grieser for his useful input regarding the scraper measurements.

There are many more people that deserve a "Thank you" at this point: The people from the MPIK construction office and the workshops, the whole CSR crew and of course the rest of the Wolf group (special thanks to Kaija and Elisabeth for the coffee table company). Also, thanks to Heidi for proofreading this thesis.

To all my friends, who always had time for me (and a beer or two), when a problem seemed unsolvable or also just because: I couldn't have done it without you!

As always, special thanks goes to my family. For everything.

Erklärung

Ich versichere, dass ich diese Arbeit selbstständig verfasst habe und keine anderen als die angegebenen Quellen und Hilfsmittel benutzt habe.

Heidelberg, den 17.12.2015 .....